Spectroscopic Measurement Techniques for Aerospace Flows

Paul M. Danehy* and Brett F. Bathel*
NASA Langley Research Center, Hampton, Virginia, 23681-2199, USA

Craig T. Johansen†
University of Calgary, Calgary, AB, T2N 1N4, Canada

Andrew D. Cutler‡ and Samantha Hurley§
The George Washington University, Newport News, VA 23602, USA

1. Introduction

The conditions that characterize aerospace flows are so varied, that a single diagnostic technique is not sufficient for its measurement. Fluid dynamists use knowledge of similarity to help categorize and focus on different flow conditions. For example, the *Reynolds number* represents the ratio of inertial to viscous forces in a flow. When the velocity scales, length scales, and gas density are large and the magnitude of the molecular viscosity is low, the Reynolds number becomes large. This corresponds to large scale vehicles (e.g Airbus A380), fast moving objects (e.g. artillery projectiles), vehicles in dense fluids (e.g. submarine in water), or flows with low dynamic viscosity (e.g. skydiver in air). In each of these cases, the inertial forces dominate viscous forces, and unsteady turbulent fluctuations in the flow variables are observed. In contrast, flows with small length scales (e.g. dispersion of micro-particles in a solid rocket nozzle), slow moving objects (e.g. micro aerial vehicles), flows with low density gases (e.g. atmospheric re-entry), or fluids with a large magnitude of viscosity (e.g. engine coolant flow), all have low Reynolds numbers. In these cases, viscous forces become very important and often the flows can be steady and laminar. The *Mach number*, which is the ratio of the velocity to the speed of sound in the medium, also helps to differentiate types of flows. At very low Mach numbers, acoustic waves travel much faster than the object, and the flow can be assumed to be incompressible (e.g. Cessna 172 aircraft). As the object speed approaches the speed of sound, the gas density can become variable (e.g. flow over wing of Learjet 85). When the object speed is higher than the speed of sound (Ma > 1), the presences of shock waves and other gas dynamic features can become important to the vehicle performance (e.g. SR-71 Blackbird). In the hypersonic flow regime (Ma > 5), large changes in temperature begin to affect flow properties, causing real-gas effects to occur (e.g. X-43 Scramjet). At even higher Mach numbers, chemistry and nonequilibrium effects come into play (e.g. Startdust re-entry capsule), further complicating the measurement. These limits can be predicted by calculating the ratio of chemical and thermal relaxation time to the flow time scales. Other non-dimensional numbers can be used to further differentiate types of aerospace flows.

In the development of a new aerospace vehicle, flow data obtained from ground-testing facilities is critical. Ground tests are often performed to verify operation at realistic flight

* Research Scientist, Advanced Sensing and Optical Measurement Branch, MS 493.
† Assistant Professor, Mechanical and Manufacturing Engineering
‡ Professor, Mechanical and Aerospace Engineering Department, 1 Old Oyster Point Road, Suite 200.
§ Graduate Research Assistant, Mechanical and Aerospace Engineering Department

conditions and/or to validate computation predictions of the flows. Optical measurement techniques are often used in ground tests since they can provide non-intrusive, quantitative data to validate the computational models and also improve understanding of the flows. Force and moment measurements, while extremely useful, only provide integrated quantities (i.e. total wall pressure and total wall shear stress). Physical probe measurements, which provide quantitative information pertaining to the state of the flowfield (examples include Pitot pressure probes, hot wires, etc.), can potentially influence the very flowfield property under study. This is especially a concern at conditions for Ma > 1, where the presence of a probe is particularly intrusive (i.e. can generate flow disturbances such as shock waves). Flow visualization techniques, including schlieren and shadowgraph, provide useful information about flow structures, but are qualitative.[1,2] Spectroscopic measurement techniques can provide large amounts of quantitative, off-body data, which can help explain results obtained from conventional measurement techniques (e.g., lift, drag, or heating).

A large body of research is devoted to the study of incompressible (Ma < 0.3), single phase flows with negligible heat transfer and without any heat sources (e.g. chemistry). These types of flows can be accurately predicted through the solution of the incompressible momentum and mass conservation laws.[3] Of course, the presence of turbulence makes the solution of the momentum equation difficult, often requiring additional equations (i.e. turbulence models) and/or large computational resources.[4] In gaseous flows, the force due to gravity is often neglected, leaving a partial differential equation relating the velocity and pressure fields. As a result, non-intrusive, off-body measurements of velocity and pressure are usually the main sought-after quantities in low-speed, incompressible flows. Recently, van Oudheusden provided a review of velocimetry-based pressure measurements based on exploitation of this pressure-velocity relationship.[5] Pressure is typically calculated from either a direct spatial integration of the pressure gradient in the momentum equation, or through a Poisson formulation. Since 3D velocimetry measurements that are both temporally and spatially resolved are difficult to perform, direct pressure measurements from conventional techniques (e.g. pressure probes) are still valued in these types of flows. Note that if the gas density is known, the pressure can also be determined from temperature data by using the appropriate equation of state.

When particles are seeded into the flow to facilitate a velocity (and/or pressure) measurement technique, there are several requirements that need to be satisfied from a fluid-dynamic standpoint. The particles must be dispersed uniformly, must faithfully follow the flow, and must not adversely affect the velocity field.[6] Using established seeding techniques, small diameter particles (i.e. low Stokes number), and low particle mass loadings can satisfy these requirements. In higher Mach number flows, these tasks are more difficult. When particles are seeded from the wall, it is often not possible to achieve penetration into a high-speed core flow without producing large flow disturbances downstream.[7] Particle seeding uniformity presents a special challenge in short duration or “impulse” facilities (detailed below) because the run durations are usually on the order of milliseconds and the test gas is initially at rest. Furthermore, as the gas velocity increases, the requirements of the imaging system also increase (e.g. temporal resolution, exposure time, etc.) Flow discontinuities, such

as shock waves, present additional challenges with regards to the ability of the particles to faithfully follow the flow. Tedeshi *et al*. (1999) performed an experimental study to quantify the particle lag of micron-sized particles through an oblique shock wave.[8]

In addition to the challenges associated with particle seeding in higher Mach number flows, compressibility effects also inhibit the computation of the pressure field from velocity measurements alone, as can be done in low-speed flows. The conservation of energy, equation of state, chemical reactions, and the transport of multiple species also need to be considered. As a result, non-intrusive measurements of temperature and density are also desired. Even in low Mach number flows when heat transfer or heat release (e.g. combustion) occurs, measurements of temperature are also needed. In extreme cases, where the flow experiences rapid changes in temperature, thermal and chemical nonequilibrium can occur. This can result in the need to measure different types of temperatures such as rotational, vibrational, and translational components. In many of the cases described above, spectroscopic techniques are required.

A variety of different molecular-based optical measurement techniques exist and are commonly used to study aerospace flows. A few of these methods – planar laser induced fluorescence (PLIF), Rayleigh and Raman scattering, and coherent anti-Stokes Raman spectroscopy (CARS) – will be detailed in this manuscript. Several textbooks and review papers provide detailed literature and technical reviews of these methods. Many of these books and papers will be referred to below but a primary important textbook is that of Eckbreth [9] which will be referred to extensively in this manuscript. In the following paragraphs, we provide a brief but broader review of molecular based spectroscopic techniques to provide context for the more detailed sections.

Optical emission spectroscopy (OES) is a method that disperses naturally emitted light to provide quantitative flow field information.[10] However, OES can only be used to study luminous environments. Also, it is difficult to determine spatially-specific information using OES since the collection optics average all the light along its optical path. These limitations can be overcome by using a light source such as a lamp or a laser. If a light source is incident upon a gaseous medium the incident photons can either be absorbed, scattered, or can transmit through the medium. These different possible light paths present opportunities for different methods to probe and measure the gas. Absorption spectroscopy [11] uses the transmitted light to diagnose the sample: the method compares the transmitted intensity with a sample present to a reference thereby determining the sample's absorption integrated along the optical path. Rayleigh scattering, Raman scattering and laser induced fluorescence (LIF) (detailed below in this manuscript) collect scattered light at an angle to the incoming light. This localizes the measurement point at the intersection between the incoming light and the optical path of the detection optics. Measurements can be made at a single spatial location or, using a camera, measurements can be made along a line or in an image plane. Whereas Rayleigh scattering is an elastic scattering process, Raman scattering is inelastic, with a small amount of energy either gained from or lost to the surrounding medium. LIF is a two-step process wherein a photon from the incident beam is absorbed and then is subsequently emitted. These scattering processes emit light approximately isotropically in three

dimensions (into 4π steradians) so that the intensity of the light drops off as one over the distance from the measurement point squared (*inverse square law*). Consequently, using conventional lenses, only a small fraction (typically ~1%) of the scattered light can be collected.[9] The abovementioned scattering techniques do not require the coherence property of a laser and are known as *incoherent* measurement techniques.

Coherent measurement approaches involve the use of multiple laser beams, which are directed into and interact with the flowfield. These techniques make use of the coherence of laser light to perform nonlinear wave-mixing, which generates coherent signal beams. The resulting laser-like beam does not follow the inverse square law. Instead, it can propagate long distances without loss. It can also be spatially filtered to reject flow luminosity (which does follow the inverse square law) without losing signal intensity. For coherent measurement techniques, the measurement volume is determined by the location of the crossing of the laser beams. Unfortunately, these coherent techniques are much more complicated to set up and harder to keep aligned than incoherent techniques. Also, these methods are nonlinear and are therefore generally more difficult to analyze and interpret than incoherent techniques. However, coherent techniques, such as coherent anti-Stokes Raman spectroscopy (CARS), provide high signal-to-noise ratio data in applications with limited optical access and/or flow luminosity.

The wide variety of aerospace facilities present many challenges to the implementation of optical measurement techniques. Facilities range from those which operate at lower Mach number but large physical scale and/or high pressure (to obtain high Reynolds number) to those capable of producing high-enthalpy flow. Such flow facilities can often have hazards that must be accommodated in order to make measurements. Such hazards include those associated with high pressure, explosives, high voltage, high acoustic noise and toxic gas generated by the facility and the measurement system. Consequently, in many facilities the operator cannot be near the facility during operation so the equipment must be operated remotely or must operate autonomously. To reduce costs and increase test section size and operating pressure range many hypersonic facilities operate for very short duration, for example 100 msec or less. These are known as impulse facilities. For laser systems operating at 10 Hz only one measurement can be acquired in these facilities per tunnel run. Since some impulse facilities can operate only once per day it is difficult to obtain a statistically significant number of measurements with some measurement techniques. In such facilities higher-speed measurement systems that can obtain data at kHz or MHz rates are desirable. Large impulse facilities can move a few centimeters during operation, complicating measurement technique alignment. The flow through longer-run-duration facilities induces vibrations that can misalign optical measurement systems and changes in the model position may occur via thermal expansion of the support system. Furthermore, many large facilities have poor or no optical access; if there is optical access the window material may not be suitable for the desired measurement technique. Aerospace flow facilities are often located in dirty operating environments and for practical considerations the lasers often are placed far from the test section requiring long path lengths resulting in misalignment and reduced laser energy delivered to the test section. Finally, some hypersonic facilities produce very

luminous flow, making difficult the detection of weak light signals. In such flowfields, coherent optical measurement techniques are desirable.

The next section of this chapter reviews some of the equipment commonly used to perform the different measurement techniques. The following sections introduce and develop the theory behind four important measurement techniques used to study aerospace flows: PLIF, Rayleigh and Raman scattering and CARS. Theoretical developments are limited to introductory material with references provided for more detailed analysis. Following this, selected measurement examples are described. These examples do not provide an exhaustive review, but are meant to illustrate typical applications.

2. Equipment Used for Molecular-Based Optical Measurement

There are similarities in the hardware used in most optical spectroscopic measurement systems. Some of the more common lasers and detection systems will be summarized here. References for commercially available equipment described are not cited to avoid preferential treatment to certain vendors. It is difficult to capture all possible types of lasers and optical detection systems in a few paragraphs. This section is intended to provide an introduction and overview to the uninitiated and is not a comprehensive discussion. The various specifications described are approximate and are presented only to provide rough orders of magnitude.

Laser systems can be classified as continuous wave or pulsed, though hybrid systems also exist. Continuous wave (*CW*) lasers operate continuously and are specified by their operating power in Watts. CW lasers can be made to operate with very narrow spectral resolution suitable for high-resolution spectroscopy where the spectral width of the laser is negligible compared to the spectrum being measured. Inexpensive, low powered diode lasers having power on the order of 1 mW are used for absorption measurements. Higher powered CW lasers on the order of 10 W are used for Rayleigh scattering measurements. These higher powered CW lasers are generally not broadly tunable, so for resonant techniques like laser-induced fluorescence only coincidental spectral overlaps between available laser frequencies and atomic or molecular transitions can be exploited. To perform spectroscopic measurements at arbitrary wavelengths, high-powered CW lasers can be converted to tunable light using dye lasers and/or other energy conversion systems such as doubling or mixing crystals, sometimes in combination with other CW lasers. Currently, high-resolution (i.e. laser linewidth much narrower than the typical absorption linewidths) CW lasers are available commercially from the ultraviolet (UV) to the infrared (IR). The main limitations of CW lasers are their relatively low power output which may require long integration times to acquire data with sufficient signal-to-noise ratio in some applications. Whereas absorption spectroscopy, which detects the full laser beam, can be performed at hundreds of kHz, scattering approaches like the Rayleigh, Raman and LIF that use CW lasers typically acquire data several orders of magnitude slower because of low signal levels. For comparison, a typical hypersonic flow with a gas velocity of 2000 m/s, a 1 mm resolution would require 500 ns time resolution, corresponding to 2 MHz data acquisition rate.

Diode lasers provide CW light in most wavelength ranges of spectroscopic interest from the ultraviolet to the far infrared. Wavelengths can be varied over a limited range by modulating the temperature or injection current of the diode, at up to MHz scan rates,[12] providing extremely high time resolution for wavelength-scanning measurements. Because the lasers and detectors are small, have no moving parts, and the lasers are often coupled to optical fibers, these devices can be used to produce relatively robust measurement systems that are particularly well suited to the often harsh environments associated with nonequilibrium hypersonic flows. These characteristics have made diode laser absorption spectroscopy a particularly desirable technology for hypersonic flight testing programs.[13]

Pulsed lasers typically producing much higher power (on the order of 10^8 Watts) for short durations, typically over a few nanoseconds, have been commercially available for about three decades. Such powers are usually required to perform nonlinear spectroscopic measurement techniques like CARS. These lasers are usually specified in terms of the energy per pulse. For example, frequency doubled Nd:YAG laser systems can produce 1 J per pulse at 532 nm. Again, this type of laser is not broadly tunable but it can be used to pump a dye laser or optical parametric amplifier and together with other conversion devices (doubling or mixing crystals) can produce high-energy tunable output from the UV to the IR. Ten ns duration pulsed lasers allow measurements to be made with "flow freezing" producing time resolution. Raman, Rayleigh, PLIF and CARS systems based on Nd:YAG lasers typically integrate signals over 10 to 500 ns time durations. Unfortunately, commercially available high energy pulsed laser systems typically operate at repetition rates of 10 to 100 Hz, which according to the calculations above, are too slow to resolve unsteady flow fluctuations. Therefore, individual measurements can be considered instantaneous, but successive measurements are not correlated in time. The linewidth of pulsed lasers is typically broader than high resolution narrowband lasers because of a number of factors. A consequence of the Heisenberg uncertainty principle is that the shorter the duration of a laser pulse, the spectrally broader the laser pulse will be. Consequently, the spectrally narrowest 10 ns pulses typically have line widths equal to 0.004 cm^{-1}. These pulses are routinely obtained by injection seeding pulsed Nd:YAG lasers so that only a single longitudinal mode is amplified. These injection-seeded pulses are much broader than commercially available CW Nd:YAG lasers. Without seeding, the same Nd:YAG laser would have an even larger linewidth of about 1 cm^{-1}. Nd:YAG-pumped narrowband dye lasers typically have line widths within the range of 0.03 to 0.5 cm^{-1}, though modifications such as injection seeding or intercavity etalons can be used to reduce the linewidth of a pulsed dye laser. Conversely, spectrally selective elements can be removed to create a broadband (red) dye laser with a linewidth of 20 nm (~ 500 cm^{-1}) or more.[14]

There are several new laser technologies that have been developed in the past decade with high output power and fast repetition rates. This allows for flow freezing, temporally resolved measurements to be obtained with good signal-to-noise levels. *Pulse burst laser* technology uses Nd:YAG lasers that have been optimized to be pulsed 25-100's of times in succession at frequencies up to 1 MHz. Pulse burst laser technology is not yet widely commercially available although it is being brought to market. Another relatively new technology that

produces high power and high repetition rates is known as *ultrafast* or *femtosecond* lasers. As the name implies, the duration of the laser pulses can be nearly a million times shorter than a typical nanosecond laser. While the energy per pulse (typically less than 10 mJ, for commercially available systems) is much lower than ns-based systems, the output power can be on the order of 10^{10} Watts, opening up new opportunities for coherent measurement approaches. Such high powers can be efficiently converted using optical parametric amplifiers and doubling or mixing crystals to extend the tuning range of femtosecond lasers to the UV and IR. Femtosecond lasers are commercially available at repetition rates up to 10 kHz - still two orders of magnitude too slow to time-resolve unsteady hypersonic flows. Even though the resulting measurements would not be time correlated, such high data rates are especially useful for acquiring statistics in short duration or expensive-to-operate test facilities. The higher data rate allowed by femtosecond lasers would be beneficial in most experiments. Picosecond-duration lasers are also available for spectroscopic measurement applications, though picosecond lasers have neither the high energy per pulse of nanosecond lasers nor the high peak power of femtosecond lasers. The linewidth of a femtosecond laser is closely related to the duration of the pulse. Typical off-the-shelf femtosecond lasers with pulse duration on the order of 100 fs have linewidths of ~10 nanometers. While this relatively large linewidth prevents conventional high-resolution spectral-domain spectroscopy, the time domain can instead be used to obtain detailed spectral information.

Most measurement techniques use some type of spectrally selective optic or optical system to collect or process light. The simplest spectrally selective optic consists of filters that are placed in front of detectors or cameras. Absorptive and reflective filters are commercially available (or can be custom manufactured at a reasonable cost) at many wavelengths, for example to block the laser's wavelength and collect the signal in another wavelength. In some applications, the narrower the spectral filter the better, since the signal is often very close to the laser's wavelength such as in Rayleigh and rotational Raman scattering. Spectral filters blocking a 10-20 nm full width half maximum (FWHM) wide band near the laser's wavelength with greater than 6 orders of magnitude of attenuation while transmitting >95% of the Raman shifted signal can be purchased. However, such filters do not provide sufficient resolution to observe Doppler broadening and Doppler shifts required for gas temperature and velocity measurement from Rayleigh scattering, for example. Gaseous filters, such as I_2 vapor contained in a heated cell, can provide spectrally narrow (0.0015 nm or 0.05 cm^{-1} FWHM) and high (6 or more orders of magnitude) absorption which is useful in many applications.[15] Etalons are spectrally dispersive optics or optical systems that are made of a pair of partially reflective mirrors. An etalon's resolution depends on its flatness and reflectivity; the resolution can be high enough (0.01 cm^{-1}) to resolve the Doppler broadening (0.05 - 0.5 cm^{-1}) in typical hypersonic flow experiments and have an advantage over gas filters in that they can operate at any wavelength. Spectrometers, containing a dispersive optic such as a prism or grating, are typically used to disperse a signal beam into a spectrum that can be acquired by a detector or camera. Small (100 mm focal length), easy-to-use fiber-optic coupled spectrometers are commercially available for applications in which spectral resolution on the order of 0.02 nm (5 cm^{-1}) is acceptable. Larger spectrometers (for example with 1 meter or longer focal length) provide higher resolution spectra – the

resolution generally increasing linearly with the focal length. Coupled with a CCD camera, such spectrometers can typically achieve resolutions of 0.15 cm^{-1}/pixel.[16] Resolution can sometimes be improved by using a camera with smaller pixels or by using a telescope at the exit of the spectrometer to enlarge the spectrum.[17]

For spectroscopic measurement techniques, light is detected with a variety of different single point, line, or imaging devices. Among single point detectors, photodiodes are typically used in applications where the intensity of the collected light is high, for example in absorption spectroscopy. Photodiodes are used because they are linear over a wide range of light intensities, have fast time response, require relatively simple electronics and are inexpensive to produce. Photomultiplier tubes (PMTs) are usually single-point detectors, but they allow variable gain useful for amplifying light at low signal levels, while also providing a fast (sub-ns) time response. While photodiodes and PMTs are both available as linear and even two-dimensional arrays, other camera technologies are usually used in spectroscopic applications where high resolution spatial or spectral information is required. Charge coupled device (CCD) cameras provide the linear response (less than 1% nonlinearity), high dynamic range (12-16 bits) and high sensitivity required by many spectroscopic imaging or spectral applications. For applications requiring short exposures, for example to freeze the flow or to reject unwanted luminosity while capturing a transient signal, CCD cameras can be fitted with an image intensifier allowing exposure times down to hundreds of picoseconds. CCD cameras having 1 million pixels or more typically frame at tens of Hz consistent with high-powered YAG laser systems. CCD camera technology has been extended to much higher speeds (up to MHz rates) albeit with lower spatial resolution (for example 160x160 pixels). Recently, Complementary metal–oxide–semiconductor (CMOS) camera technology has allowed megapixel cameras to frame at tens of thousands of Hz allowing new opportunities for optical measurement techniques.

3. Laser-Induced Fluorescence (LIF)

Laser-induced fluorescence (LIF) uses a laser to probe individual species within the flowfield, providing information pertaining to both the thermodynamic (pressure, temperature, mole fraction) and fluid dynamic state (velocity) of the gas. The laser can be focused to a point for LIF measurements, formed into a thin sheet using a cylindrical and focusing lens in combination for planar LIF measurements (PLIF), or used to illuminate a volume for three-dimensional or stereoscopic imaging. Reviews of the laser-induced fluorescence measurement technique are available from Eckbreth[9] and others.[18,19] The measurement technique works by inducing a transition, usually of an electron, from a lower energy state (E_1) to an excited energy state (E_2) via stimulated absorption of one or more photons in the atomic or molecular species of interest. In a two-level model assumption, the atom or molecule of interest in the E_2 state then returns to the E_1

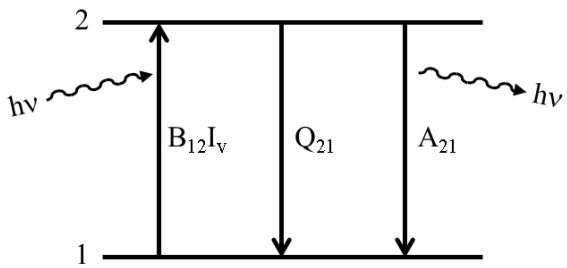

Figure 3.1: Two-level energy model of single-photon fluorescence.

state by transferring energy via spontaneous emission of a photon (fluorescence), or by transferring energy non-radiatively through a collision with another atom or molecule (collisional quenching).

For an atom, such as N or O, the energy required to induce an absorption transition of an electron to the E_2 state from the ground (E_1) state is equal to the energy difference between the atom with an electron occupying the excited electronic orbital and the atom's ground electronic orbital configuration, respectively. For molecules, such as N_2 and O_2, the energies of the E_2 and E_1 states include the energies associated with the vibrational and rotational motion of the molecule in addition to the energy associated with the molecule's electronic configuration. Figure 3.1 shows a generalized two-level energy model for fluorescence with the stimulated absorption transition induced by a single photon.

In Fig. 3.1, the rate at which the absorbing medium in the E_1 state transitions to the E_2 state is proportional to the product of the Einstein coefficient for stimulated absorption, B_{12}, and the laser's spectral irradiance (power per unit area per unit frequency), $I_\nu = IL_\nu$, where I is the irradiance (power per unit area) and L_ν is the laser spectral profile or laser line-shape (per unit of frequency).[9] The energy of the absorbed and emitted photons is the frequency, ν, multiplied by Planck's constant, h. The Einstein A_{21} and B_{12} coefficients describe the probabilities for emission and absorption,[20] respectively, while Q_{21} is the collisional quenching rate. For absorbing species, the line-shape function, Y_ν, describes the spectral width for a particular energy level.

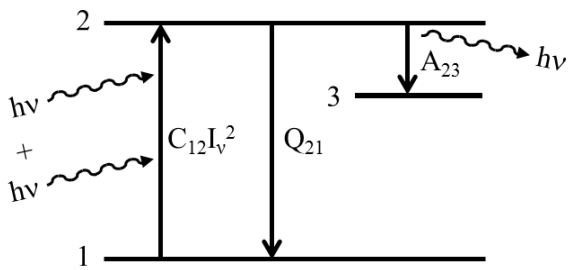

Figure 3.2: Two-level energy model of two-photon fluorescence.

As detailed in Reference 9, the line-shape function combines effects from Gaussian-shaped Doppler broadening and Lorentzian-shaped homogeneous broadening mechanisms. The integral of the product of the absorption line-shape function, Y_ν, and the laser's spectral profile, L_ν, is defined by the overlap integral, $G = \int Y_\nu L_\nu d\nu$, and describes what portion of a particular absorption transition is affected by the incident laser radiation. The rate constant for stimulated absorption, W_{12}, which describes the rate at which species in E_1 transition to E_2 via absorption of a single photon[9,19] is then given by:

$$W_{12} = B_{12}IG \tag{3.1}$$

As the laser passes through a flowfield, it is absorbed at a rate corresponding to Eq. 3.1, inducing a transition between the E_1 and E_2 states. Consequently, as the laser continues to propagate through the flowfield, the irradiance is continually diminished as a result of the absorption process as described by the Beer-Lambert law.[9]

In certain circumstances, the energy separation between the E_1 and E_2 states for the species being examined with LIF is such that the frequency of a photon necessary to induce an absorption transition is far into the ultra-violet portion of the electro-magnetic spectrum.

However, achieving frequencies far into the UV with conventional laser systems can be difficult.[20] Additionally, strong absorption of UV radiation by many materials and gases (including air) below approximately 200 nm limits the application of laser systems capable of producing such frequencies.[9] One solution is to use two-photon LIF techniques to probe species having absorption transitions in the deep UV. With a two-photon technique, the frequency (and therefore energy) of each photon is half that required by a single photon for the same transition. Figure 3.2 shows a generalized two-photon fluorescence energy model for two-photon LIF. For atomic species, such as N or O, spontaneous emission is often observed between E_2 and an intermediate energy state, E_3.

For the two-photon LIF process in Fig. 3.2, the two-photon absorption cross-section results in a rate constant different from that in Eq. 3.1 and has the form:[9,20,21-24]

$$W_{12} = C_{12} I^2 G \tag{3.2}$$

where C_{12} relates to the two-photon absorption cross-section. Note that the dependence of the rate constant scales with the square of the incident laser irradiance, I. This behavior arises from the probability of observing the simultaneous arrival of two photons, which is the square of the probability for the arrival of a single photon.[20]

In both Figures 1 and 2, Q_{21} is the so called *quenching* rate constant. It describes the rate at which energy is transferred through non-radiative collisions between excited atoms or molecules in the E_2 state and atomic or molecular collision partners of species i. This rate constant is computed similarly to that in Ref. 9 as:

$$Q_{21} = N_T \sum_i \chi_i \sigma_{s,i} v_{s,i} \tag{3.3}$$

where $N_T = P/k_B T$ is the total population of the excited state, χ_i is the mole fraction of quenching species i, $\sigma_{s,i}$ is the collision cross-section between the excited species, s, and quenching species, i, and $v_{s,i} = \sqrt{8 k_B T_{trans}/\pi \mu_{s,i}}$ is the mean relative velocity[25,26] between the excited species and quenching species, with $\mu_{s,i}$ being their reduced mass and T_{trans} their translational temperature. The spontaneous emission coefficient, A, in Figures 1 and 2 is also known as the Einstein A coefficient and describes the probability for spontaneous emission of a photon by an atom or molecule in the excited state.[20]

For the two-level model in Fig. 3.1, the rate of change of the populations N_1 and N_2, in the E_1 and E_2 states, respectively, can be obtained from relations similar to those presented in Ref. 9:

$$\frac{dN_1}{dt} = -\frac{dN_2}{dt} = -N_1 W_{12} + N_2 (Q_{21} + A_{21}) \tag{3.4}$$

$$N_1 + N_2 = N_S = \chi_s f_B N_T \tag{3.5}$$

Equation 3.5 is a conservation law saying that the combined populations of the E_1 and E_2 states are equal to the initial population of the excitation species' E_1 state, N_S, which is in turn

the product of the species mole fraction, χ_s, the total population, N_T, and the temperature-dependent Boltzmann fraction, f_B. Equation 3.4 assumes that the laser intensity is sufficiently weak such that stimulated emission (W_{21}) can be neglected.

The Boltzmann fraction, f_B, describes the ratio of the number of absorbers initially occupying E_1 relative to all possible energy states at a particular temperature, T, when a system is in thermodynamic equilibrium.[26] This term has a general form given by:[9,26,27]

$$f_B = \frac{g_j e^{-E_j/k_B T}}{\sum_j g_j e^{-E_j/k_B T}} \tag{3.6}$$

where g_j is the degeneracy of state j. Degeneracy refers to the number of quantized states that exist in a given energy level, E_j.[26] The summation in the denominator is termed the *partition function*, Q.

More involved differential rate equations can be formulated for the two-photon method like those presented in Ref. 24. It should be noted that the models presented in Figures 1 and 2 neglect transitions from E_1 to E_2 resulting from collisions, with a rate constant of Q_{12}. This is usually a good assumption for large energy separations associated with the visible or UV transitions typically employed for LIF. Transitions from the E_2 and E_3 states resulting from pre-dissociation (Q_{pre}) and ionization (Q_{ion}), which are described in Refs. 9 and 19, have also been neglected.

3.1 Linear, Steady State Solution

If a continuous laser source is used to populate the E_2 state and detection of fluorescence occurs well after this source is turned on, then N_2 can be assumed to have reached its steady-state value. From this assumption, the left-hand-side of Eq. 3.4 is set to zero, resulting in two algebraic equations (Eqs. 2.9 and 2.10) for two unknowns (N_1 and N_2). The same assumption can be made to determine the population, N_2, achieved by a pulsed laser source if the time required to reach steady state is short compared to the duration of the pulse. This population is computed as:

$$N_2 = \frac{\chi_s f_B N_T W_{12}}{W_{12}+Q_{21}+A_{21}} \tag{3.7}$$

The product of this excited state population and the spontaneous emission rate constant is N_2A_{21} and represents the number of transitions per unit time and per unit volume. Integrating this constant value with respect to time gives the total number of transitions per unit volume during the detection period. Substituting Eq. 3.1 for W_{12}, and assuming that W_{12} is small compared to A_{21} and Q_{21} (which is valid for low-intensity excitation), a relation for the total number of photons collected via fluorescence by the detection device is:[19]

$$S_{LIF} = \chi_s f_B N_T B_{12} I G \Phi t_{det} V \frac{\Omega}{4\pi} \eta \tag{3.8}$$

where $\Phi = A_{21}/(Q_{21} + A_{21})$ is the fluorescence yield, t_{det} is the period of detection, V is the volume probed by the laser source, Ω is the solid angle over which detection occurs, and η is

the detection efficiency. The fluorescence yield, Φ, describes the fraction of de-excitation transitions that occur via spontaneous emission (fluorescence) relative to all de-excitation transitions (i.e. spontaneous emission and collisional quenching, assuming pre-dissociation and ionization are negligible). Neglecting the constants in Eq. 3.8, a generalized form for the fluorescence signal similar to that presented in Refs. 19 and 28, including its thermodynamic (χ,P,T) dependencies and velocity dependence (arising from the Doppler effect), is:

$$S_{LIF} \propto \chi_s N_T f_B(T) B_{12} IG(\chi_s, P, T, U) \Phi(\chi_s, \chi_i, P, T) t_{det} \tag{3.9}$$

3.2 Non-Steady State Solution

For a pulsed laser source, if N_2 is changing during the period of detection, then the entirety of Eq. 3.4 must be solved to obtain the time-dependent population, $N_2(t)$. Similarly, if the duration of the laser pulse is of the same order of magnitude as the time required to reach steady state, then the population at the end of the laser pulse, $N_2(t_{laser})$, can be obtained by solving Eq. 3.4. By assuming the laser intensity behaves as a Heaviside step function in time, the population $N_2(t)$, existing during laser excitation can be calculated by substituting the relation for N_1 from Eq. 3.5 into Eq. 3.4 and integrating with respect to time:[19]

$$N_2(t) = \chi_s f_B N_T \frac{W_{12}}{r} \cdot (1 - e^{-rt}),\ 0 < t \leq t_{laser} \tag{3.10}$$

where $r = W_{12} + Q_{21} + A_{21}$. The inverse of this value, r^{-1}, is the characteristic time needed to achieve steady state. This solution assumes an initial condition which typically specifies the initial excited state population to be zero ($N_2(0) = 0$).

When the laser source is turned off, the only pathways to return to the ground state from the excited state are assumed to be through either spontaneous emission or collisional quenching. Therefore, for the period following laser excitation, the first term on the right-hand-side of Eq. 3.4 is zero. This modified version of Eq. 3.4 is then used to determine the excited-state population for the period after laser excitation by integrating with respect to time:[19]

$$N_2(t) = \chi_s f_B N_T \frac{W_{12}}{r} \cdot (1 - e^{-rt_{laser}}) \cdot e^{-(t - t_{laser})/\tau_{LIF}},\ t > t_{laser} \tag{3.11}$$

This solution assumes that the laser intensity is turned off instantaneously, with an initial condition given by Eq. 3.10, evaluated at $t = t_{laser}$. This solution shows that the population in the excited state decreases exponentially in time after the laser pulse.

The term $\tau_{LIF} = (Q_{21} + A_{21})^{-1}$ in Eq. 3.11 is referred to as the fluorescence lifetime and describes the rate at which the population in a particular excited state transitions to a lower state. As with the derivation of Eq. 3.8, the total number of photons collected via fluorescence over the detection period is determined by multiplying Eqs. 2.16 and 2.17 by the spontaneous emission rate Einstein coefficient A_{21}, accounting for the collection volume and detection system, and integrating with respect to time:[19]

$$S_{LIF} = \chi_s f_B N_T \Phi B_{12} IG t_{laser} \left\{ \left[1 - \frac{1 - e^{-rt_{laser}}}{rt_{laser}} \right] + \left[\frac{(1 - e^{-rt_{laser}})}{t_{laser}/\tau_{LIF}} \right] \right\} V \frac{\Omega}{4\pi} \eta \tag{3.12}$$

Like Eq. 3.8, this solution assumes that W_{12} is small compared to A_{21} and Q_{21}. However, if the laser irradiance, I, is sufficiently large such that W_{12} and W_{21} are of the same order of magnitude as Q_{21} and A_{21}, then both must be included in the solution. This gives $r = W_{12} + W_{21} + Q_{21} + A_{21}$ during laser excitation. By defining the irradiance at which the fluorescence signal saturates as[9,19] $I_{sat} = (Q_{21} + A_{21})/(B_{12} + B_{21})$ and rearranging r such that $r = \tau_{LIF}^{-1}[I/I_{sat} + 1]$, a more detailed formulation for the fluorescence signal, including effects from laser saturation, is given as:[19]

$$S_{LIF} = \chi_s f_B N_T \Phi B_{12} \frac{I}{1+I/I_{sat}} G t_{laser} \left\{1 + \frac{1-e^{-rt_{laser}}}{rt_{laser}} \left(\frac{I}{I_{sat}}\right)\right\} V \frac{\Omega}{4\pi} \eta \qquad (3.13)$$

When $I \ll I_{sat}$, Eq. 3.13 simplifies to a form similar to that of Eq. 3.10.

3.3 Multi-Level Fluorescence Modeling

In the preceding discussion, a simplified two-level model of fluorescence was put forth, which provides for an understanding of the most basic physical mechanisms and energy transfer processes involved. This basic description allows for the development of a general analytic relation between the fluorescence signal and these mechanisms and processes. However, such a simple description does not account for rotational or vibrational energy transfer occurring between the absorbing species and the surrounding gas mixture. Since each electronic energy level depicted in Fig. 3.1 can have vibrational and rotational fine structure for molecular species, such energy transfer processes result in a redistribution of the populations to various vibrational and rotational states. To account for these processes, analytical models including multiple energy states and a system of population rate equations are used. Discussion of such modeling aspects can be found in Refs. 9, 18 and 19.

3.4 Translational Temperature

Translational temperature resulting from the random thermal motion of the absorbing species can be determined by measuring the Doppler-broadened width of the absorption line-shape function[9] If the temperature, pressure, and mole fractions at a particular location are assumed to be constant, then the Boltzmann fraction and fluorescence yield in Eq. 3.9 at that location are also assumed to be constant. If these assumptions are valid, and if the laser line-shape function is known, then the fluorescence signal will be proportional to the overlap integral at a particular frequency. By scanning the laser's spectral frequency across a particular transition, the absorption line-shape function can be obtained.

Once the absorption line-shape is obtained, the contribution of homogeneous broadening mechanisms to the line-shape must be determined to allow for calculation of the Doppler-broadened line width. Homogeneous broadening can include components from Van der Waals broadening and Stark broadening effects,[29] in addition to collisional pressure-broadening effects. In many cases, the Van der Waals and Stark effects can be ignored, resulting in homogeneous broadening from pressure alone. If the pressure is known, then the component of the line-shape due to homogeneous broadening can be determined. Alternately, if the pressure is sufficiently low, then collisional pressure broadening can be ignored. A

fitting algorithm can then be used to determine the contribution of Doppler broadening to the line-shape. This allows for a more accurate temperature calculation as only one parameter, $\Delta\nu_D$, must be iterated upon to fit the line-shape. The translational temperature, T_{trans}, of the absorbing species can then be obtained by modifying Eq. 3.2:

$$T_{trans} = \frac{m}{8\ln(2)k_B}\left(\frac{c\Delta\nu_D}{\nu_0}\right)^2 \tag{3.14}$$

Both single-photon[29- 31] and two-photon [32 - 36] methods have been used to measure translational temperature. The requirement of scanning a laser's frequency to resolve the Doppler-broadened line-shape can limit the time resolution of the temperature measurement such that only average translation temperatures can be obtained.

Figure 3.3 shows LIF data (dotted line, upper plot) from Ref. 29 obtained by performing a frequency scan with a semiconductor laser source over an argon metastable transition centered at 810.4 nm. Each frequency scan over the absorption transition took 500 seconds to complete. In the experiment, argon plasma was generated using an inductively-coupled plasma torch. The translation temperature, *T*, and electron number density, n_e, were obtained by fitting the Voigt line-shape function, which accounted for both Doppler-broadening and several collisional broadening mechanisms, to the experimental LIF data (solid line, upper plot). The lower plot in Fig. 3.3 shows the residual: the difference between the experimental LIF data and the fitted line-shape. An analysis of one of the scans in Ref. 29 gave T_{trans} = 6800±690 K, resulting in a ~10% measurement uncertainty.

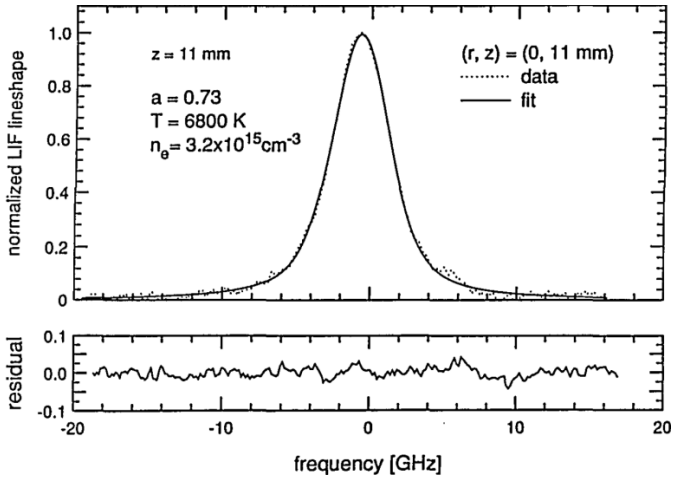

Figure 3.3: Experimental LIF data measured (dotted line, upper plot) in an Argon plasma and corresponding fit of Voigt line-shape (solid line, upper plot) to the experimental data (upper plot) and difference between experimental data and fit (lower plot). Image reprinted from Ref. 29 with permission of the authors and the publisher.

3.5 Rotational Temperature

For molecules, the rotational temperature, T_{rot}, can be obtained by exciting two absorption transitions and relating the signal intensities observed from each transition to the rotational temperature through modification of Eq. 3.9. This method was demonstrated in Ref. 37 using a two-photon excitation method to measure rotational temperature at a point in a cold (~300 K) turbulent flow. For each rotational transition, the population fraction, f_B, is dependent on the rotational energy, F_J, rotational quantum number, *J*, and rotational temperature, T_{rot}, of the absorbing species. This assumes that excitation occurs in the same vibrational state, *v*, such that the vibrational energy, G_v, is constant for each probed rotational transition. If χ_s, G, Φ, and t_{det} are assumed to be independent of the rotational state of the absorbing species,

then the ratio, *R*, of fluorescence signals can be simplified to the following relation, similar to that in Refs. 19, 38-41:

$$\frac{S_{LIF,i}}{S_{LIF,j}} = R = C\frac{B_{12,i}E_i}{B_{12,j}E_j}\frac{(2J_i+1)\exp[-F_{J,i}/k_BT_{rot}]}{(2J_j+1)\exp[-F_{J,j}/k_BT_{rot}]} \tag{3.15}$$

where the subscripts *i* and *j* refer to the particular excited absorption transition, *E* is the laser energy such that $E = at_{laser}I$, *a* is the beam cross-sectional area, t_{laser} is the temporal pulse width of the laser, and *C* is a constant which includes all terms that are independent of the rotational state of the absorbing species. Solving for T_{rot} in Eq. 3.15 yields:

$$T_{rot} = \frac{-\Delta E_{rot}}{k_B \ln\left[CR\frac{B_{12,j}E_j(2J_j+1)}{B_{12,i}E_i(2J_i+1)}\right]} \tag{3.16}$$

Here, $\Delta E_{rot} = (F_{J,i} - F_{J,j})$, and is the difference in energy between the probed rotational levels. To minimize the uncertainty associated with the measured rotational temperature, δT_{rot}, a propagation-of-error analysis can be performed on Eq. 3.15 by computing the derivative of the signal ratio, *R*, with respect to T_{rot}:[39,42]

$$\frac{\delta T_{rot}}{T_{rot}} = \frac{k_BT_{rot}}{\Delta E_{rot}}\frac{\delta R}{R} \tag{3.17}$$

This analysis suggests that by increasing ΔE_{rot}, and thereby probing two widely separated rotational energy levels, the uncertainty in T_{rot} can be proportionally decreased for a given error in *R*.[39]

Figure 3.4 shows a mean rotational temperature map of nitric oxide measured in the wake of a 6.35-mm-thick flat plate in a Mach 3 turbulent flow, taken from Ref. 42. The map was obtained by averaging a series of images taken for excitation from rotational levels *J* = 8.5 and *J* = 10.5, computing the ratio of the two averaged images, and using a relation similar to that in Eq. 3.16 to compute T_{rot}. In this experiment, it was shown that the turbulent nature of the flowfield required excitation of two relatively closely spaced rotational levels (*J* = 8.5 and 10.5). This requirement arose from the nonlinear relation between *R* and T_{rot} in Eq. 3.16, which can be heavily influenced by flowfield turbulence.

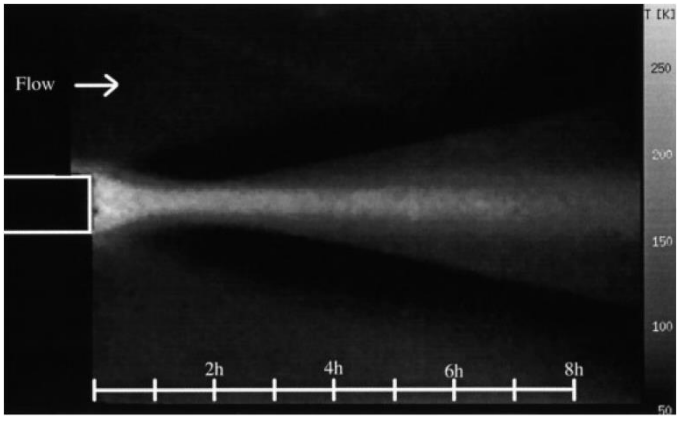

Figure 3.4: Rotational temperature map obtained in the supersonic wake of a flat plate using two-line rotational thermometry. Image reprinted from Ref. 42 with permission from the authors and Springer Science and Business Media.

Figure 3.4 shows a time-averaged temperature measurement obtained using a single laser, which probed the two transitions in separate wind tunnel runs. To obtain instantaneous temperature measurements in a plane using this method, a two-laser, two-camera system can be used, as in Refs. 38-40. In Ref. 39, instantaneous two-line temperature

imaging of OH in a shock tube at a nominal pressure of 40.53 kPa and temperature range of 1500-2950 K resulted in temperature measurements with errors of ~20%-25%.

Multi-rotational-line temperature methods also exist and can potentially provide relatively higher sensitivity and dynamic range T_{rot} measurements, particularly at lower temperatures where rotational energy levels are closely spaced.[43] Such methods are appropriate when large variations in T_{rot} are expected, requiring probing of several rotational levels. The rotational temperature is computed by exciting multiple rotational lines and measuring the signal. This measured fluorescence signal, together with the measured laser energy are then substituted into the following relation:[41]

$$\ln\left[\frac{S_{LIF,i}}{B_{12,i}E_i(2J_i+1)}\right] \tag{3.18}$$

A plot of this logarithmic term versus $F_{J,i}$, known as a Boltzmann plot, yields a linear trend with a slope of $-k_B T_{rot}$. Refs. 43-46 used this method to characterize rotational temperatures in arc jet flows. An alternative multi-line approach used in Ref. 47 for measurements in a flame involved fitting a simulated rotational spectrum to experimental data to obtain T_{rot}.

3.6 Vibrational Temperature

The vibrational temperature, T_{vib}, can be measured using an approach similar to that used for rotational temperature. For T_{vib} measurements, a two-line approach can be used. Such an approach is presented in Ref. 48, in which the same rotational levels, $J_i = J_j$, are probed in two different vibrational levels, $v_i \neq v_j$, resulting in nearly constant rotational energies, F_J, but different vibrational energies, G_v. Assuming χ_s, G, Φ, and t_{det} to be independent of the rotational and vibrational levels, the ratio of fluorescence signals, R, can be used to measure vibrational temperature, T_{vib}, in a way analogous to that in Eqs. 2.21 and 2.22.

As with rotational temperature measurements, a multi-vibrational-line temperature measurement method can also be used to infer T_{vib} by modifying the logarithmic term from Eq. 3.18:[41]

$$\ln\left[\frac{S_{LIF,i}}{B_{12,i}E_i(2J_i+1)\exp\left[-F_{J,i}/k_B T_{rot}\right]}\right] \tag{3.19}$$

If the rotational level, J_i, is fixed and the rotational energy, $F_{J,i}$, is kept approximately constant, then the vibrational temperature can be computed independently of rotational temperature.[41] This is done by generating a Boltzmann plot of vibrational energy, $G_{v,i}$, versus this logarithmic term, resulting in a linear relation with a slope equivalent to $-1/(k_B T_{vib})$.

Figure 3.5(a), taken from Ref. 41, shows a Boltzmann plot generated using a relation like that in Eq. 3.19 to infer vibrational temperature. The image data in the experiment was used to measure T_{vib} at a point downstream of a free-piston shock tunnel nozzle on the centerline of the flow. In this experiment, three absorption transitions were selected that had nearly constant rotational energies, F_J, but differing vibrational energies, G_v. In Fig. 5(b), also taken from Ref. 41, the vibrational temperature of NO was observed to be constant with distance

downstream of the nozzle, even though the nozzle was conical and the rotational temperature was shown to be decreasing with distance downstream, as the flow expanded. A simple computational model (shown in Fig. 5(b)) was not able to accurately predict the measured vibrational temperature.[41] As shown in Fig. 5(b), T_{vib} = 785±30 K, giving an uncertainty of ~4%.

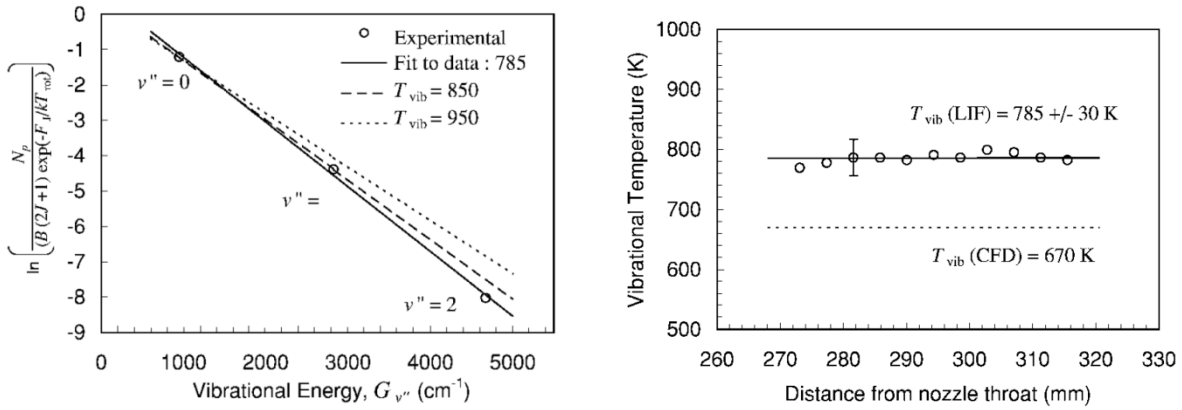

(a) (b)

Figure 3.5: Vibrational temperature measurement obtained by probing multiple vibrational levels and generating (a) a Boltzmann plot and (b) vibrational temperatures plotted as a function of distance downstream. Images taken from Ref. 41 with permission of the authors.

3.7 Species Concentration

Returning to the simplified Eq. 3.8, it is possible to quantify the number density, $\chi_s N_T$, using LIF. However, several factors complicate the interpretation of a LIF signal and its relation to concentration. For instance, Q_{21} in Eq. 3.3 depends on the concentration and temperature of the absorbing species and all other constituent species in the probed mixture. If the temperature of the mixture were unknown, then a separate measurement of temperature would be required to determine both Q_{21} and the temperature-dependent Boltzmann fraction. The measurement system also requires an appropriate absolute intensity calibration to a known reference, which can be further complicated by the collection optics and filters used in such a measurement. The response of the detection system as a function of S_{LIF} intensity and spectral frequency must also be well understood. The following discussion highlights some of the methods that have been used to provide concentration measurements that address some of these issues.

3.7.1 Non-quantitative flow visualization

A relatively simple approach to obtaining a qualitative visualization of species concentration is to use laser-induced fluorescence to visualize the spatial distribution of the absorbing species. To first-order, the fluorescence signal in Eq. 3.9 is proportional to the relative species concentration, $\chi_s N_T$, assuming all other terms are constant. In hypersonic non-equilibrium test facilities, the formation of reactive species at the high enthalpies required to simulate true flight conditions can influence the gas dynamics under study. For example, arc-heated facilities are often used to simulate true flight enthalpy conditions by depositing significant energy into a test gas and then expanding that gas to hypersonic Mach numbers. This process can result in a non-uniform species distribution resulting from the unsteady nature of the electrical arc.

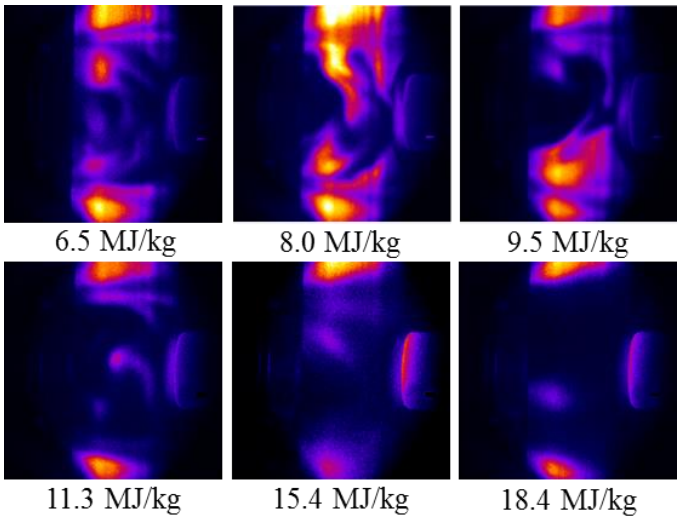

Figure 3.6: Instantaneous nitric oxide planar LIF flow visualization images in false color acquired in the Hypersonic Materials Environmental Test System (HyMETS) arc-heated facility at NASA Langley Research Center. Flow is from left to right. Images taken from Ref. 49 with permission of authors.

Figure 3.6 from Ref. 49 shows instantaneous nitric oxide (NO) planar LIF images in false color acquired in the Hypersonic Materials Environmental Test System (HyMETS) arc-heated facility at the NASA Langley Research Center for a flow simulating earth's atmosphere at several enthalpy conditions. The flow in this figure is from left to right. The object on the right-hand edge of the field of view is a 25 mm diameter silicon carbide tipped probe aligned with the axis of symmetry of the facility nozzle. For the lowest enthalpy condition shown (6.5 MJ/kg), the spatial distribution of NO within the core of the nozzle flow is irregular, suggesting that the energy deposition by the arc upstream of the nozzle is non-uniform. As the flow enthalpy increases to 18.4 MJ/kg, the distribution of NO remains irregular and the total production of NO appears to decrease.

Other examples of such LIF-based flow visualization experiments are provided in Ref. 50. The interpretation of such flow visualization images and their relation to quantitative species concentration measurement is complicated. The remaining terms in Eq. 3.9, such as the quenching rate constant, often vary significantly in high-speed non-equilibrium flows and can be difficult to determine. The sections that follow detail approaches for quantitative measurements of concentration which address such complicating factors.

3.7.2 Saturated LIF

To avoid the complications associated with an unknown quenching rate constant, a relatively high laser irradiance where $I \gg I_{sat}$ can be used to probe the absorbing species.[9] In this instance, the stimulated absorption and emission rates dominate both collisional quenching and spontaneous emission rates; that is, $(W_{12} + W_{21}) \gg (Q_{21} + A_{21})$. The result of this leads to a modified form of Eq. 3.8 where stimulated emission is included and the fluorescence signal is of a form similar to that in Ref. 9:

$$S_{LIF} = \chi_s f_B N_T A_{21} \frac{B_{12}}{B_{12}+B_{21}} t_{det} V \frac{\Omega}{4\pi} \eta \tag{3.20}$$

If A_{21}, B_{12}, and B_{21} are known, then this method can be used to measure concentration if the remaining terms, such as f_B, can be determined. In practice, it is difficult to achieve $I \gg I_{sat}$ because high powered pulsed laser beams are typically Gaussian, both spatially and temporally, so much of the acquired signal can originate from the lower intensity edges of the Gaussian beam, which excite the fluorescence linearly.[9] Further discussion of this method is found in Refs. 9 and 18.

3.7.3 Pre-dissociation LIF

Pre-dissociative fluorescence involves inducing a transition to a level in the excited state, which can then couple to a dissociative state, resulting in dissociation of the molecule into smaller molecules or atoms. Pre-dissociative fluorescence concentration measurements are similar to saturated fluorescence measurements in that the dependence on Q_{21} in Eq. 3.8 can be removed, in this case by exciting the absorbing species to a pre-dissociative state where the pre-dissociation rate, Q_{pre}, is faster than both Q_{21} and A_{21}.[9] A discussion of this mechanism can be found in Refs. 51 and 52 and a general discussion of the method can be found in Refs. 9 and 18. An application of the pre-dissociative technique was presented in Ref. 53 to measure time-averaged OH concentrations in a supersonic hydrogen-air turbulent combusting flow. Concentrations as high as 5.4×10^{16} cm^{-3} with uncertainties of 21% or less were reported.[53]

3.7.4 Short-Pulse LIF

There are two methods of using short laser pulses to quantitatively determine concentration. The first probes the species of interest with a laser pulse having a duration much shorter than the time between collisions with other species. With this method, the concentration can be determined by relating the measured exponential fluorescence decay behavior to the initial signal magnitude during the short-pulse excitation period. While this decay is a function of both A_{21} and Q_{21}, extrapolation of the exponential behavior to initial excitation provides an inferred peak intensity magnitude, which is assumed to be independent of collisional quenching effects.[18] This independence is assumed since a sufficient number of collisions, required to transfer energy non-radiatively from the excited state, would not yet have occurred. A discussion of this method can be found in Ref. 18. Reference 54 uses a form of this short-pulse method for OH concentration measurements in a turbulent flame.

A second method for measuring concentration involves using a laser pulse that is shorter than or comparable to the fluorescence lifetime, but not shorter than the collisional timescales described in Ref. 9. In this approach, the fluorescence lifetime is measured directly, usually using a photomultiplier tube. This short-pulse LIF method can also be used to determine spontaneous emission[55] and collisional quenching[56,57] rate constants when the thermodynamic conditions of the probed mixture are known. Even for unknown conditions, measurement of the fluorescence lifetime allows for the quenching rate to be determined and accounted for. Refs. 58 and 59 use a two-photon LIF technique in which fluorescence lifetime measurements are used to correct for collisional quenching effects in a similar manner. Figure 3.7(a), taken from Ref. 58, shows spectral scans of atomic nitrogen in the NASA Ames Aerodynamic Heating Facility arc jet flow (red data) and laboratory flow reactor (green data). Fluorescence measurements from the flow reactor and a krypton reference cell were used for intensity calibration in order to provide absolute atomic nitrogen number densities. The fluorescence lifetimes observed in the arc jet and flow reactor were used to correct for collisional quenching effects. Figure 3.7(b), also taken from Ref. 58, shows radial atomic nitrogen number density measurements for two air/argon arc jet runs taken 35.6 cm downstream of the nozzle exit. The reported uncertainty in number density was ~12%.[58]

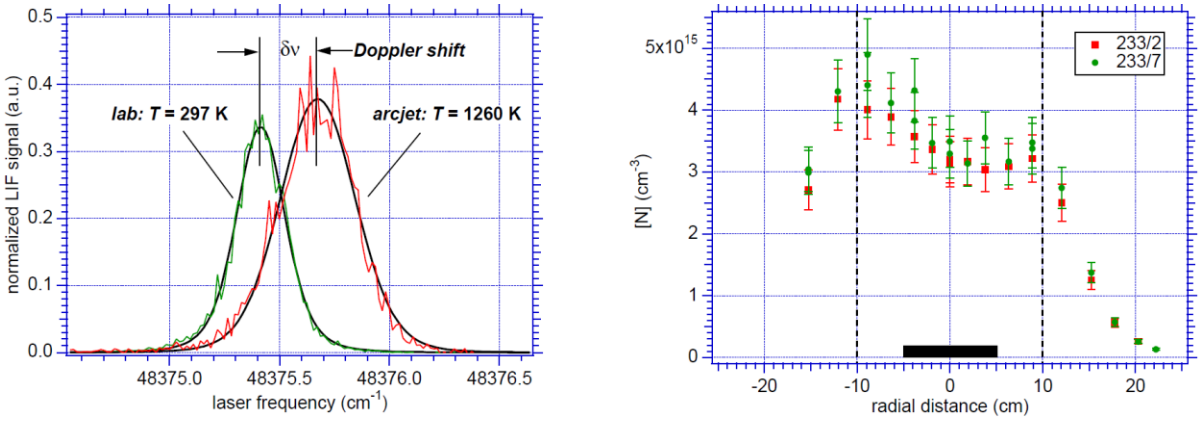

(a) (b)

Figure 3.7: (a) Spectral scans of atomic nitrogen in the NASA Ames Aerodynamic Heating Facility arc jet flow and in a laboratory flow reactor and (b) measured number densities spanning the radial direction of the arc jet 35.6 cm downstream of the nozzle exit. Image taken from Ref. 58 with permission of the authors.

A similar approach is being developed for mole fraction measurements in hypersonic turbulent boundary layers using naphthalene PLIF.[60,61] One benefit of using naphthalene is that it sublimates at slightly elevated temperatures (with respect to room temperature), allowing for the study of scalar transport effects in transitional boundary layers, turbulent boundary layers, and ablating surfaces.

3.7.5 Bi-Directional Beam LIF

If two overlapping, counter-propagating beams are tuned to the same transition, the ratio of fluorescence signals results in the cancellation of all terms in Eq. 3.9 at a point in the flow, with the exception of the spatially dependent laser irradiance. Thus, the spatially varying ratio

of fluorescence signals can be equated to the spatially varying ratio of irradiances of the respective beams. The Beer-Lambert law can then be used to relate irradiance, and therefore fluorescence signals, to number density via the relation:[62]

$$k_s(\nu) = N_s \varphi_s(\nu) \tag{3.21}$$

where $\varphi_s(\nu)$ is the transition cross-section of the absorbing species, describing the absorbing species' interaction with the incident irradiance on a per atom or molecule basis.[20] Combining Eq. 3.21 with the Beer-Lambert law allows for a relation between the natural logarithm of the signal ratio and the absorbing species number density to be made:[63]

$$N_s(x) = \frac{1}{2\varphi_{s,0}} \frac{d}{dx} \ln\left[\frac{S_{LIF,1}(x)}{S_{LIF,2}(x)}\right] \tag{3.22}$$

where $S_{LIF,1}(x)$ and $S_{LIF,2}(x)$ are the spatially varying fluorescence signal intensities of the forward- and backward-propagating beams, respectively. In Eq. 3.22, $\varphi_{s,0}$ is the peak transition cross-section, with $\varphi_{s,0} = \varphi_s(\nu_0)$.[20]

This concentration measurement technique was first demonstrated in Ref. 63. The technique only requires that a value for $\varphi_{s,0}$ be known in order to make an absolute concentration measurement of N_s .[63] For total absolute concentration, however, f_B must either be assumed or measured, as from Eq. 3.5, $N_s = \chi_s f_B N_T$. Figure 3.8, taken from Ref. 63, graphically depicts the process of obtaining a concentration of OH in a methane-air flame. In the top plot, the fluorescence intensities are plotted versus position across the flame. The middle plot shows the natural logarithm of the ratio of these two signals with position and the bottom plot shows the calculated absolute OH concentration using Eq. 3.22. Measurements of OH concentration were also made in a plane in Ref. 63 by imaging fluorescence from two counter-

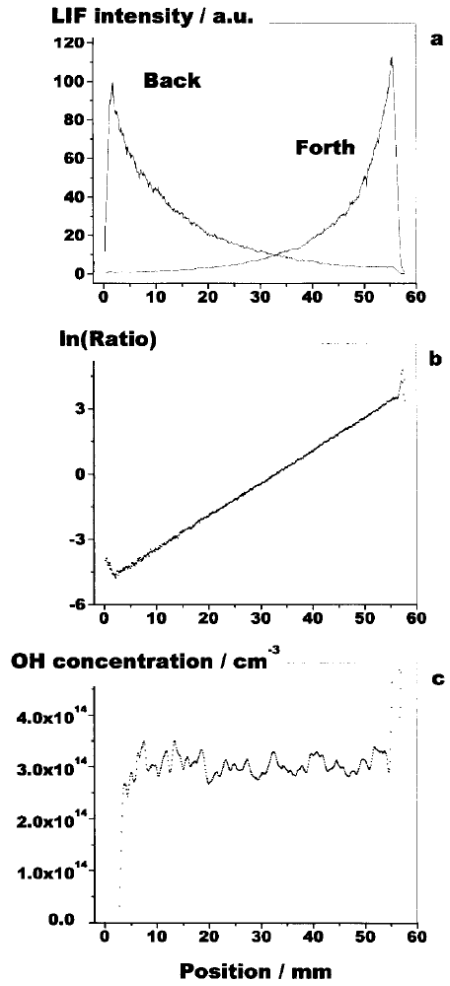

Figure 3.8: Graphical depiction of methodology used to measure concentration using bi-directional beam LIF. Top plot shows spatially varying fluorescence signals, middle plot shows natural logarithm of ratio of these signals, and bottom plot shows OH concentration calculated using Eq. 3.22. Image reprinted from Ref. 63 with permission of the authors and Springer Science and Business Media.

propagating laser sheets. Equation 3.22 was applied using each row of pixels to compute signal ratios. Single-shot imaging of a hydrogen/air/oxygen flame allowed for calculation of means and standard deviations of OH concentration. Using 10 images for each laser sheet direction (20 total images), Figure 3.8 of Ref. 63 showed a mean peak OH concentration of ~8.8×10^{14} cm^{-1} with a standard deviation of ~$\pm 1.7 \times 10^{14}$ cm^{-1}, which is ~19.7% of the mean.

3.7.6 Combined LIF/Rayleigh/Raman

In reacting flows, flows undergoing transition-to-turbulence, and turbulent flows, the time-varying nature of flow properties makes it difficult to ascertain concentration. By making simultaneous time-resolved measurements of temperature and major species concentrations, the thermodynamic-dependent parameters in Eq. 3.9 (Boltzmann fraction, overlap integral, and fluorescence yield) can be determined, and a direct relation between concentration and fluorescence signal established. A combined fluorescence, Rayleigh scattering, and Raman scattering measurement technique was used for this purpose in Ref. 64 . In that experiment, the Raman scattering was used to measure instantaneous concentrations for major species (O_2, N_2, H_2O, and H_2) in a turbulent hydrogen jet flame. This allowed for the mole fractions of the collision partners, χ_i, in Eq. 3.3 to be calculated. The combined Rayleigh/Raman scattering measurements were then used to measure temperature. The temperature-dependent collisional cross-sections and relative velocity in Eq. 3.3 could then be calculated, and the collisional quenching rate, Q_{21}, determined. The temperature-dependent absorption line-shape and Boltzmann fraction could also be determined from the temperature measurement. The additional measurement of laser energy then provided for a direct relation between NO fluorescence signal and concentration to be established. In Ref. 65, this technique was used to make concentration measurements of CO in turbulent premixed and stratified CH_4/air flames. A stated CO concentration accuracy and precision (single standard deviation) of 10% and 4.5%, respectively, were given.[65]

3.8 Pressure

Measurements of pressure can also be obtained using a LIF-based approach, although such measurements are not as common as LIF-based temperature and species concentration measurements (described in the preceding sections) for determination of the thermodynamic state of a gas. This is in part due to the implicit relationship between fluorescence signal and pressure in Eq. 3.9, as opposed to the explicit relationships with temperature and concentration.

One method by which pressure can be measured is by tuning to the center frequency of an absorption transition and relating the measured fluorescence signal to pressure. For such measurements, the selected absorption transition must be carefully chosen such that the temperature dependence (i.e. f_B) can be removed over the range of temperatures expected for the experiment. When this is done, the fluorescence signal is inversely proportional to the static pressure if certain additional simplifying assumptions are made. This approach has been used in low-quenching ($Q_{21} \ll A_{21}$) flows[42] or quenching-dominated ($Q_{21} \gg A_{21}$) flows where the pressure broadening is much larger than the Doppler broadening.[66,67]

Often for quenching-dominated LIF-based pressure measurements, however, the dependence of fluorescence signal on pressure when tuned to the center of an absorption transition is nearly removed, as N_T (and hence pressure) can be factored out of both the numerator and denominator in Eq. 3.9. An alternative approach is to infer pressure from the absorption lineshape function. This can be accomplished if a separate measure of temperature can be made so that the absorption lineshape dependence on temperature can be isolated from its dependence on pressure. Common methods include those which relate the width of the absorption lineshape to pressure,[68] those which resolve the entire absorption lineshape function,[69] and those which relate the ratio of fluorescence signal from the wing of the lineshape to the signal from the center of the lineshape.[70-72]

3.9 Doppler-Based Velocimetry

The Doppler effect can be used to determine flow velocities for atomic and molecular species. The translational motion of the absorbing species in the direction of the excitation laser's propagation, described by a velocity component U, results in a shift of the absorption line-shape function away from its transition center frequency, ν_0, according to:

$$\Delta\nu = \frac{U}{c}\nu_0 \tag{3.23}$$

This velocity-dependent frequency shift of the absorption line-shape function is implicit in the overlap integral, G, and thus, its effect on fluorescence signal can be seen through the dependence of G on the velocity component, U, in Eq. 3.9. When a component of translational motion of the absorbing species opposes the laser's direction of propagation, corresponding to the negative $(-)$ solution of Eq. 3.23, the incident laser radiation appears to be at a higher frequency from the perspective of the gas. Hence, as the laser's frequency is scanned over the absorption transition, Y_ν, the measured intensity of fluorescence corresponding to this profile is shifted toward a lower frequency, or red-shifted. The converse is true when motion is in the same direction as the laser's propagation, corresponding to the positive $(+)$ solution of Eq. 3.23, where the absorption profile is shifted toward a higher frequency, or blue-shifted.

In one implementation, velocity component measurements can be made by scanning the laser over an absorption transition in both the measurement volume and a reference cell. In this case, the Doppler shift between the absorption profiles is used to compute an average velocity according to Eq. 3.23. Examples of such measurements include those in an arcjet,[30,31,35,73] supersonic underexpanded jets,[68,69,74-76] shock tunnel,[77,78] and non-reacting supersonic flow with a rearward-facing step.[79-81] Such measurements require that the flowfield be relatively steady since shot-to-shot fluctuations in fluorescence intensity from thermodynamic and fluid dynamic variations can affect the measured line-shape. The velocity measurements can also be complicated by a frequency shift in the line-shape function resulting from collisional effects (pressure). In compressible flows, the pressure field can vary significantly, and hence the collisional shift in the line-shape function can likewise vary. Absorption of laser energy can also result in an apparent frequency shift in the line-shape function. Recall that the line-shape function must be inferred from the overlap integral, G,

which represents the convolution of the absorption line-shape and laser spectral line-shape. If absorption is significant, then irradiance will vary spatially, resulting in a spatially varying overlap integral. An analysis of how absorption affects the line-shape frequency shift is presented in Ref. 78. If flow symmetry is assumed, then the frequency shift due to pressure can be estimated.[77] Flow symmetry can also be used to correct for the frequency shift resulting from absorption.[31] Alternatively, if two counter-propagating laser beams are used, these frequency shift effects can be completely removed. The use of counter-propagating beams results in two excitation peaks, separated in frequency by twice the velocity-induced Doppler shift. The need for a reference cell measurement to ascertain velocity can also be removed, as a counter-propagating beam approach is self-referencing.[75,82,83]

Figure 3.9 in Ref. 78 shows a two-component velocity measurement about a heat shield model taken in a hypersonic free-piston shock tunnel. In this experiment, laser sheets were directed in both the radial (vertical) and axial (horizontal) directions so that measurements of the Doppler-shifted absorption profiles for the respective directions could be obtained and compared with measurements from a static reference cell to infer velocities. An estimation of velocity errors incurred from the frequency shifts due to absorption and collisional effects was also performed. In Ref. 78, three separate absorption transitions were probed to measure two different velocity components, with one transition being used for both components. This resulted in a measured axial freestream velocity of 2394±68 m/s and a measured radial velocity of 53±50 m/s, giving respective uncertainties of ~2.8% and ~94.3%.[78]

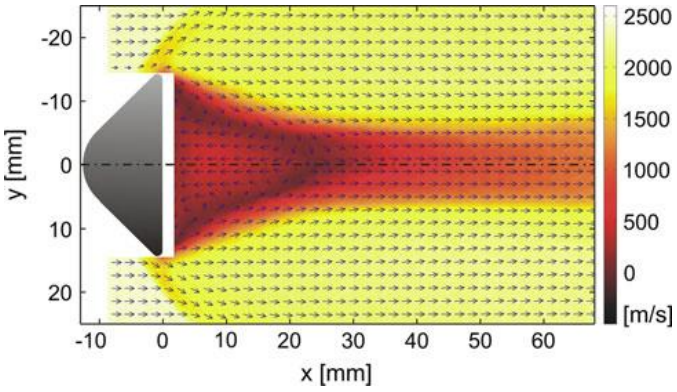

Figure 3.9: Two-component velocity measurement using fluorescence-based Doppler velocimetry technique. Vectors denote flow direction and color map represents magnitude. Image reprinted from Ref. 78 with permission of the authors and Springer Science and Business Media.

Another form of the fluorescence-based Doppler velocity measurement is a fixed frequency method, which can allow for an instantaneous velocity component measurement. With the fixed frequency technique, a narrow linewidth laser is tuned off the absorption profile peak to a point where the slope of the profile is maximum, as described in Refs. 70 and 84. Assuming that the absorption profile is approximately linear in the region of maximum slope, the measured signal intensity can be related to the Doppler shift of the profile. This fixed frequency Doppler velocimetry technique has been applied to a free jet,[85] supersonic underexpanded jet,[86] and reacting supersonic flow.[87] The stated random and systematic errors in Ref. 86, when added in quadrature, gave a total uncertainty of ~12%. In Ref. 87, the stated lowest time-averaged and single-shot uncertainties achieved were ~3% and ~15%, respectively, for a 1600 m/s velocity range.

3.10 Flow-Tagging Velocimetry

Another technique by which velocity can be measured using fluorescence is flow-tagging velocimetry. Fluorescence-based flow-tagging velocimetry is a time-of-flight technique that involves laser excitation—or tagging—of the gas along a line, series of lines, or grid pattern. With this form of velocimetry, the species of interest in the gas absorbs the incident radiation from a laser source, which induces either of the following: 1) fluorescence, 2) a reaction that forms a product that then emits a photon via fluorescence, or 3) a reaction that forms a product that can then be probed with another laser source to induce fluorescence. Images of the fluorescence pattern are acquired at two time delays, with velocity computed by measuring the displacement of the tagged molecules between images. Typically, a line or series of lines can be used to measure a single-component of velocity while a crossed grid pattern can be used to measure two-components. Two general fluorescence-based methods of flow-tagging velocimetry are discussed here; one that requires a single laser source and another that requires multiple laser sources. The main advantage of flow-tagging velocimetry, as compared to most Doppler-based methods (which are time averaged), is that it can make instantaneous (single-shot) measurements with fast time resolutions (as short as a few hundred nanoseconds). A disadvantage, however, is that flow-tagging velocimetry cannot provide full velocity field information. A broader discussion of molecular-tagging velocimetry, which relies on molecular tracers for flow-tagging, is provided in Ref. 88.

3.10.1 Single-laser methods

The first method involves either direct or indirect excitation of fluorescence with a single laser source. The first application of this method to a gaseous flow involved excitation of phosphorescence of biacetyl molecules, as described in Ref. 89. If this method is used, the fluorescence lifetime of the tagged molecules must be long enough so that advection provides for measurable displacements with tagged regions having signal intensities that are still above the detection limit of the imaging system at the time the second image is acquired. Typical experiments involve capturing a reference image acquired during the tagging process, or a relatively short time thereafter. If a single-framing camera is used, such as in Ref. 90, a single reference image or set of reference images is acquired. The timing of the single-frame camera is then delayed and a subsequent image or set of images is then acquired. If a two-camera system or dual-framing camera is used, such as in Ref. 91, the delayed image is acquired in sequence after the reference image. The velocity is computed by measuring the displacement of the tagged molecules

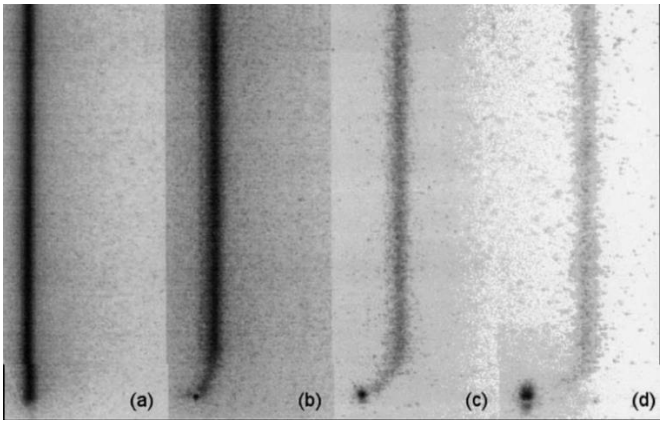

Figure 3.10: Single-line excitation of nitric oxide fluorescence used to study hypersonic boundary layer flow over a flat plate. Images, from left to right, correspond to camera delay settings of 0 ns, 250 ns, 500 ns, and 750 ns. Image reprinted from Ref. 90 with permission of the authors.

that occurs in the time between when the reference and delayed images were acquired. The form of this technique relying on direct excitation of fluorescence for flow tagging has been applied to the study of supersonic jets,[92-98] hypersonic boundary layers,[90,91,99,100] and arcjet flowfields.[31]

Figure 3.10, taken from Ref. 90, shows images from tagging a single line of nitric oxide using direct excitation of fluorescence within a flat plate hypersonic laminar boundary layer. In this Figure, the left-most image corresponds to the reference image, while the remaining images, from left to right, correspond to delayed images taken at 250 ns, 500 ns, and 750 ns after tagging, respectively. Measurements of freestream velocity, spatially averaged from a point just above the velocity boundary layer (3 mm) to 15 mm above the flat plate, resulted in a mean of 3,035±100 m/s at 90% confidence, giving an uncertainty of 3.3% of the mean.[90] Single-shot uncertainty estimates for a 3,000 m/s freestream flow and for camera delay settings of 250 ns, 500 ns, and 750 ns were 4.6%, 3.5%, and 3.5%, respectively.[90]

An indirect excitation scheme, as described in Refs. 101-103, relies on photodissociation of molecular nitrogen for flow tagging. The technique uses a femtosecond laser pulse to dissociate molecular nitrogen into two nitrogen atoms, which then recombine after a collision, forming molecular nitrogen in an intermediate state. A subsequent collision brings the molecular nitrogen to an excited electronic B state, which then emits a photon via fluorescence upon transitioning to the excited electronic A state. Ref. 103 provides a description of this process. One benefit of this indirect technique, known as Femtosecond Laser Electronic Excitation Tagging (FLEET), is that the recombination rate of dissociated atomic nitrogen allows for a much longer fluorescence lifetime. This would allow displacements to be measured over greater time scales, providing for accurate measurements of velocity in low-speed flow regions, such as in a hypersonic wake flow. Additionally, the technique relies on molecular nitrogen for tagging, which is present in most hypersonic facilities.

3.10.2 Multi-laser methods

A second method of fluorescence-based flow-tagging velocimetry involves writing a line, series of lines, or grid pattern into the flowfield by one of several laser-based mechanisms. This pattern can then be interrogated, or read, by subsequent laser pulses to induce fluorescence, allowing for the determination of velocity through measurement of the displacement of the pattern. Such techniques usually involve two or three different lasers and are therefore more time consuming to set up and more difficult to execute.

One mechanism by which a pattern can be written into the flowfield is via ionization of the absorbing species, known as Laser Enhanced Ionization (LEI) flow tagging. The tagging process is accomplished by promoting the species (such as sodium in Refs. 104-106) to a higher energy state via laser excitation near the ionization limit. Collisions then result in the ionization of the species, with the tagging pattern corresponding to the ionized regions. Subsequent laser pulses are used to induce fluorescence of the absorbing species in regions that have not been photo-ionized. Supersonic measurements of velocity in a shock tube were

performed using LEI flow-tagging in Refs. 104 and 105, and hypersonic velocity measurements in an expansion tube were performed in Ref. 106.

A second mechanism that can be used to write a pattern into the flowfield is by vibrational excitation of molecular oxygen via Raman pumping. This is followed by reading the pattern of the vibrationally-excited oxygen by inducing fluorescence. The technique, known as Raman Excitation and Laser-Induced Electronic Fluorescence (RELIEF),[107] is advantageous as it relies on the flow-tagging of oxygen which is a common working gas of most hypersonic facilities. This technique has been used to characterize turbulence in a free jet[108] and underexpanded jet.[109] The RELIEF technique, however, is limited to temperatures below 750 K. Above this temperature, a significant fraction of oxygen molecules are vibrationally excited, making it difficult to distinguish the tagged molecules from the background.[110]

Yet another mechanism involves using one laser to photo-dissociate a molecular species. This results in the formation of a product species for which a second laser can be used to read the location of the written pattern by exciting laser-induced fluorescence in the product species. The formation of the product species typically occurs through one or more reactions. A list of partner species used in the writing and reading process include: H_2O-OH,[111-117] N_2O-NO,[118] O_2-O_3,[119,120] N_2/O_2-NO,[121-124] and NO_2-NO.[94,125-132]

Figures 10(a) and 10(b), taken from Ref. 129, show images of vibrationally excited NO fluorescence in a grid pattern formed via photodissociation of NO_2 in a mixture containing 6.3% NO_2 in N_2. The images were taken in a supersonic underexpanded jet 400 ns (Fig. 3.11(a)) and 800 ns (Fig. 3.11b) after the pattern was written into the flow with a two-dimensional array of 355 nm beams. Two components of velocity were obtained by relating the displacement of the grid in the left image to a grid imaged in a stationary gas. The upper half of Fig. 3.11(c), taken from Ref. 129, shows measured streamwise velocities compared with computation, shown in the lower half of Fig. 3.11(c). The use of two pulsed dye lasers in this experiment permitted the excitation of both a low (J = 1.5) and high (J = 8.5) rotational

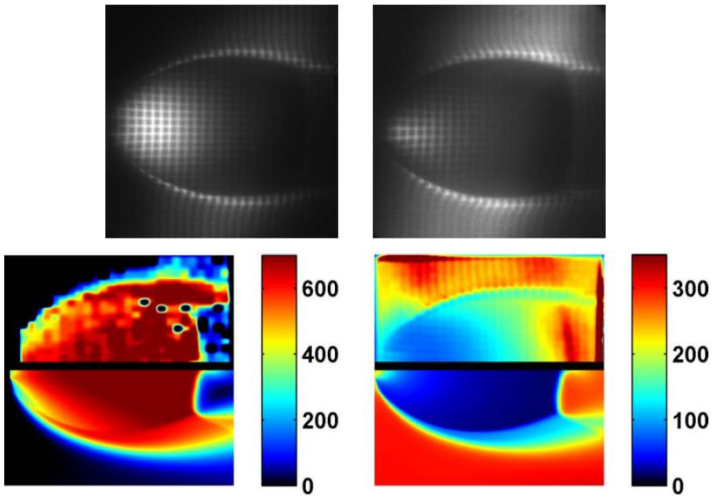

(a) (b) (c) (d)

Figure 3.11: Flow-tagging images of vibrationally excited NO fluorescence obtained (a) 400 ns and (b) 800 ns after photodissociation of NO_2. The two-dimensional grid pattern allows for calculation of two velocity components. Measured (c, top) and computed (c, bottom) streamwise velocity maps. Measured (d, top) and computed (d, bottom) rotational temperature map. Image reprinted from Ref. 129 with permission of the authors and the publisher.

level within the same vibrationally excited (v = 1) NO state. The fluorescence images corresponding to the low-J (Fig. 3.11(a)) and high-J (Fig. 3.11(b)) rotational levels also allowed for measurement of the rotational temperature by using a calculation similar to that presented in Eq. 3.16. The top half of Fig. 3.11(d), from Ref. 129, shows measured rotational temperature compared with computation, shown in the lower half of Fig. 3.11(d). Stated root-mean-square (RMS) uncertainties in the velocity measurement were ~5% with high signal-to-noise.[129] The stated RMS uncertainties in rotational temperature ranged from 9% to 35% prior to the Mach disk.[129]

NO_2-NO flow tagging velocimetry has also been used to study boundary layer transition on a flat plate in a Mach 10 wind tunnel.[131,132] Pure NO_2 was seeded into the boundary layer through a spanwise slot located downstream of the sharp leading edge. The angle of attack of the flat plate was 20 degrees, reducing the edge Mach number to about 4.2. Parallel focused beams of 355 nm light oriented normal to the surface of the flat plate (and in a plane parallel with the streamwise direction of the flow) dissociated the NO_2, creating NO. After a 40 ns delay, the NO was probed by a 226 nm laser, at which time the camera acquired an image. One microsecond later, a second 226 nm laser probed the NO and the second image was acquired with the same camera. The two images were compared to compute velocity profiles. Figure 3.12 shows the resulting velocity profiles for two cases, one with no trip (i.e. tripping element, a protuberance designed to trip the flow from laminar to turbulent) and one with a 1-mm tall cylindrical trip, where the measurements were made downstream of, and on the centerline of, the trip. (The laminar boundary layer thickness was also approximately 1 mm thick.) The figure shows mean profiles (black, top two charts) as well as profiles of the fluctuating component of velocity, u' (red, bottom two charts). For the case of no trip, the velocity profiles compare well with a compressible Blasius solution (shown in light grey). When the trip is present, the measured mean profiles depart from the laminar solution, showing a profile that is more full than the laminar profile near the plate surface with a pronounced velocity deficit near the edge of the profile. The fluctuating streamwise velocity increases by a factor of three, up to 250 m/s, between the two cases, with the fluctuations highest in the wake of the trip. The single-shot measurement precision was 15-25 m/s, which was 1-2% of the maximum velocity in the boundary layer. The accuracy was estimated to be 5-15 m/s.[131]

3.11 Advantages and Limitations of Laser-induced Fluorescence

The time scales associated with inducing fluorescence via laser excitation are typically a few hundred nanoseconds, which is much shorter than hypersonic flow time scales, therefore providing sufficient temporal resolution for high-speed transition-to-turbulence measurements. The availability of pulsed lasers capable of picosecond and femtosecond excitation allow for fluorescence measurements with time scales much less than those associated with collision and reaction time scales. Recently developed kHz- and MHz-rate pulsed laser systems have allowed image sequences consisting of tens to thousands[133] of images to be acquired, providing time-resolved information pertaining to high-speed fluid dynamic behavior. Both fluorescence-based velocimetry[128] and visualization [134, 135] experiments in hypersonic flow fields have been performed with these types of laser systems.

The spatial resolution of a LIF technique is also sufficient for many applications, and higher than other techniques such as Raman or CARS, with laser sheet thicknesses typically in the range of 0.1 to 1 mm and magnifications of tens of pixels per mm, depending on the experimental setup. Fluorescence-based measurements are more sensitive than other techniques (for example Raman spectroscopy) with sensitivity on the order of parts-per-million or better.[9]

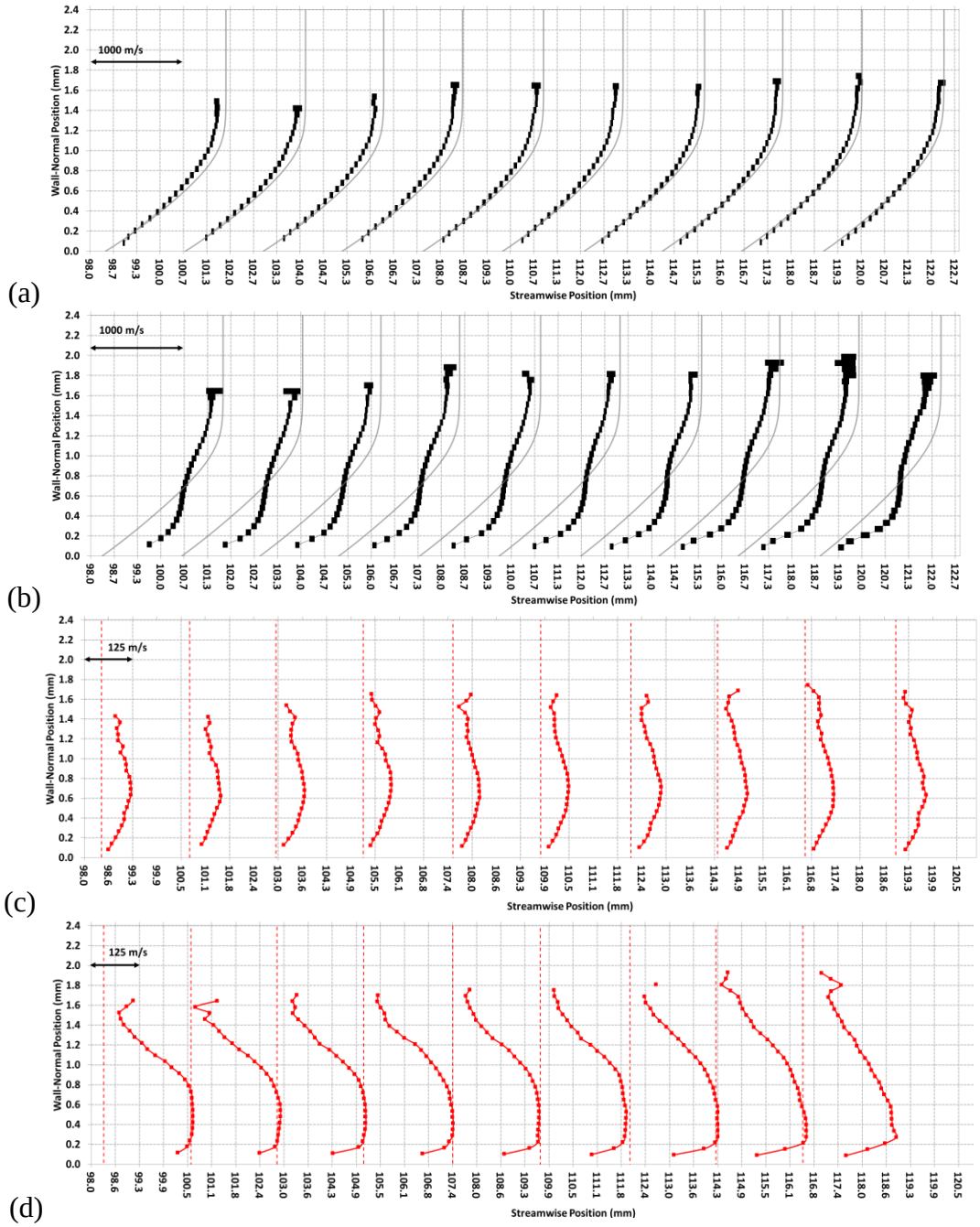

Figure 3.12: Streamwise velocity profiles on a flat plate in a Mach 10 facility for the case of no trip (a) and a k = 1 mm tall, 4 mm diameter cylinder trip (b) and the fluctuating streamwise velocity for no trip (c) and a k = 1 mm tall, 4 mm diameter cylinder trip (d). Images reprinted from Ref. 132 with permission of the authors.

Additionally, a wide range of species including intermediate combustion species can be probed using fluorescence techniques. Reference 18 provides an extensive listing of many species that have been detected using LIF and other methods. Another advantage of LIF is that it is readily extended to planar or volumetric measurement (see Refs. 136 and 137).

Several factors complicate acquisition and interpretation of LIF signals, complicating quantitative measurements. Quenching of the fluorescence, which prevents easy quantification of signal intensities, was discussed extensively above. Absorption of laser energy as the laser light passes through the flowfield can limit the effectiveness of fluorescence-based measurements, as the energy will decrease in an exponential manner over a given spatial path length according to the Beer-Lambert relations in Eqs. 2.5 and 2.6. This makes quantitative measurements difficult, as the laser energy at a particular location may not be easily determined. Absorption can be significant when the concentration of the absorbing ground state population is high, the transition cross-section is relatively large, the Einstein B coefficient for stimulated absorption is relatively large, and/or the path length through which the laser radiation passes is relatively long. To avoid strong absorption, a transition may be selected for which the population is small based on analysis of the Boltzmann fraction, as was done for PLIF visualization measurements in a hypersonic shock tunnel described in Ref. 138. Absorption can also limit measurement capabilities when fluorescence from the probed volume is re-absorbed by the species of interest. This effect, known as *radiative trapping*, occurs when fluorescence emission at frequencies readily absorbed by highly populated states must pass through gas containing these potential absorbers before reaching the imaging system. Measurements in a non-uniform or turbulent mixture are especially susceptible to errors associated with absorption and radiative trapping effects, as the absorption coefficient is a spatially- and temporally-varying property. A discussion of these issues, and some methods used to circumvent them, is provided in Ref. 9.

Another disadvantage of LIF is that it usually probes only a single species at a time, compared to Raman or CARS, which can interrogate many species simultaneously. However, the fact that PLIF can measure spatial distributions of species can compensate for the single-species capability in some applications.

Consideration must also be given to the optical access of the test facility. Since much of the work described in this discussion requires fluorescence excitation using laser frequencies in the UV portion of the electromagnetic spectrum, the window material used in hypersonic facilities must be capable of transmitting such frequencies with minimal absorption. Also, typically two or three windows are required for LIF or PLIF applications. The laser (beam or sheet) is typically brought in from one window and observed through another window at right angles to the first window. A third window can allow the laser to leave the test section, reducing scattered light, and allowing the quantification of absorption of the laser beam/sheet in some applications. These windows are typically relatively large compared to those required for CARS or diode laser absorption measurements. When short-pulse LIF experiments are performed, the inverse relationship between the pulse temporal width and spectral width (which for a Gaussian pulse is $\tau_{laser} = 0.44/\Delta\nu$)[20] can result in distortion of the temporal characteristics of the pulse. This is because the refractive properties of the

optical windows of the test facility affect the speed with which the frequency components of the short pulse pass through the window material. Reference 20 discusses issues related to short pulse excitation and interaction with optical components.

4. Rayleigh and Raman Scattering

4.1 Introduction

When a light beam passes through a gaseous medium, it can interact with the gas molecules or particles in the gas, thereby scattering light away from the path of the incident beam. *Elastic* scattering occurs if no energy is gained or lost to the medium. If energy is either absorbed or lost by the medium, the scattering is *inelastic*. Light scatter from particles that have a diameter, d, on the order of or larger than the light wavelength, λ, is termed Mie scattering. Scattering for which $d << \lambda$ is known as *spontaneous Rayleigh scattering* if elastic and *spontaneous Raman scattering* if inelastic. These processes are shown schematically in Figs. 4.1 and 4.2. Represented on the energy level diagram in Fig. 4.1, a photon excites a molecule from an originating state, 1, to a 'virtual' state, 2, from which the scattered photon is emitted. The virtual state, represented by a dashed line, is not an actual resonant state of the molecule. Instead, it indicates a non-resonant, short-lived state in which the electron distribution of the molecule is distorted. This virtual state immediately relaxes to the originating state (in the case of Rayleigh scattering) or another state (in the case of Raman scattering). Relaxation to a higher lying (e.g. vibrational) state than the originating state is termed *Stokes Raman* scattering. In this case, the molecule absorbs a quantum of energy through this process. In *anti-Stokes Raman* scattering the molecule imparts a quantum of energy to the scattered photon so that the scattered photon has higher energy than the incident photon. In this case, the originating state must not have been a ground state.

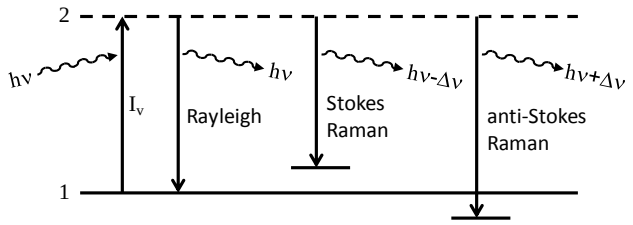

Figure 4.1. Energy level diagram indicating incident radiation, Rayleigh scattering and Raman scattering.

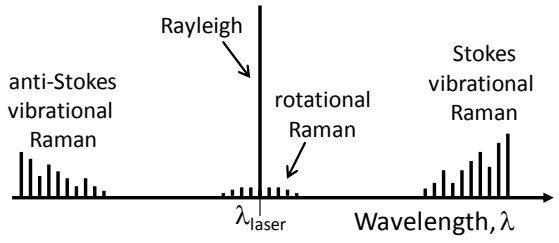

Figure 4.2. Notional Raman/Rayleigh spectra.

Figure 4.2 shows notional Raman/Rayleigh spectra, not drawn to scale. Rayleigh scattering is shown at the laser's wavelength. Discrete pure rotational Raman lines, associated with rotational quanta imparted to or subtracted from the incident laser frequency, are shown on opposite sides of the Rayleigh peak. Vibrational Raman bands are located further away, spectrally shifted towards the red (Stokes) and the blue (anti-Stokes). The vibrational Raman bands show rotational fine structure. Raman scattering is much weaker than Rayleigh scattering.

Raman scattering is typically three orders of magnitude smaller than Rayleigh scattering for most gases of interest to supersonic and hypersonic flows.[9]

4.2 Theory of spontaneous Rayleigh and Raman scattering

Comprehensive reviews of the theory and application of Rayleigh and Raman scattering have been given by others.[9,18,139,140] Herein we provide a brief introduction and overview. Later sections will show how this theory is applied to measure thermodynamic properties. Consider an electromagnetic wave incident upon a molecule, perturbing the molecule's electron cloud and making it oscillate at the same frequency as the incident wave. These oscillations cause a periodic charge separation within the molecule, known as an induced dipole moment. Oscillating dipole moments act like antennas, emitting radiation. As described in more detail by Baldwin,[141] if these oscillations are in-phase, the emission adds constructively, producing a coherent beam. If out-of-phase (for example, in the direction orthogonal to the beam), the emitted light interferes destructively and the radiation cancels. For a monochromatic plane wave passing through a gas, the constructive interference occurs only in the forward direction. The resulting emitted coherent light is perfectly in-phase with and indistinguishable from the incident wave. In a gas composed of a finite number of molecules, the destructive interference at other angles is not fully complete because of statistical variations in the number of particles located in different wavelength-sized volumes of the gas.[141,142] That is, there are not exactly the same number of particles in each wavelength sized volume, which would be required to cancel out the radiation perfectly. This statistical variation in the number density then leads to Rayleigh and Raman scattering. Rayleigh and Raman increase significantly in intensity at shorter wavelengths: both scale approximately as $1/\lambda^4$.[9]

The radiant intensity, I^{Ω}, which is the scattered power per unit solid angle, is proportional to the square of the induced dipole moment. The induced dipole moment, $\vec{p}$, is given by:[9]

$$\vec{p} = \varepsilon_0 \alpha \vec{E} \tag{4.1}$$

where ε_0 is the permittivity of free space, α is the molecular polarizability and $\vec{E}$ is the incident electric field given by $\vec{E} = \overrightarrow{E_0}\cos(\omega_0 t)$, where $\overrightarrow{E_0}$ is the amplitude of the electric field, ω_0 is the frequency of the laser light and t is time.

The polarizability of a molecule depends on its internal structure and varies with time during vibrational oscillations at the natural frequency of the molecule, ω_v, vibrating in the direction of its normal spatial coordinate, Q. The polarizability can be approximated with a Taylor series expansion:

$$\alpha = \alpha_0 + \left(\frac{\partial \alpha}{\partial Q}\right)_0 dQ \tag{4.2}$$

where the small physical displacement, dQ, of the atoms about their equilibrium positions (denoted by the subscript 0) during vibrations is:

$$dQ = Q_0 \cos(\omega_v t) \tag{4.3}$$

Combining Eqs. (4.1)-(4.3):

$$\vec{p} = \left[\alpha_0 + \left(\frac{\partial \alpha}{\partial Q}\right)_0 Q_0 \cos(\omega_v t)\right] \varepsilon_0 \overrightarrow{E_0} \cos(\omega_0 t) \tag{4.4}$$

Expanding and using a trigonometric identity:[9]

$$\vec{p} = \alpha_0 \varepsilon_0 \overrightarrow{E_0} \cos(\omega_0 t) + \tfrac{1}{2}\left(\frac{\partial \alpha}{\partial Q}\right)_0 \varepsilon_0 Q_0 \overrightarrow{E_0}[\cos(\omega_0 - \omega_v)t + \cos(\omega_0 + \omega_v)t] \tag{4.5}$$

The first term on the right side of Eq. (4.5) describes Rayleigh scattering at a frequency corresponding to the incident laser's wavelength. The second term indicates Raman scattering which is shifted from the Rayleigh scattering by $\pm\omega_v$ resulting in upshifted (anti-Stokes) and downshifted (Stokes) Raman scattering. While significant theory has been developed to describe the physics of Raman and Rayleigh scattering, the strengths of the scattering for different gases is generally measured and reported as a temperature-independent differential cross section:[9]

$$\left(\frac{\partial \sigma}{\partial \Omega}\right)_{zz} \equiv \frac{I_{zz}^{\Omega}}{NI} \tag{4.6}$$

which can be rearranged as:

$$I_{zz}^{\Omega} = \left(\frac{\partial \sigma}{\partial \Omega}\right)_{zz} NI \tag{4.7}$$

where the subscript *zz* refers to a polarization in the z (vertical) direction caused by an incident electric field oriented in the *z* direction, *N* is the number density of the gas and *I* is the laser irradiance.[9] The differential cross sections vary by process (Rayleigh vs. Raman), by molecule, and vary with the laser wavelength but are independent of pressure and temperature.

Rayleigh scattering from different molecules cannot be distinguished spectrally, so it is not usually used to detect individual species. Under circumstances where the composition is fixed or known, or limited to vary under controlled conditions,[143,144] Rayleigh scattering can be used to measure the gas density, ρ. As discussed further below, the Rayleigh scattering cross section varies from molecule to molecule, with some hydrocarbon species having cross sections more than an order of magnitude larger than N_2. The cross section for a mixture of gases is equal to the mole-fraction-weighted average of the individual cross sections. If the composition can be estimated or measured, for example by Raman scattering,[145] then the effective cross section for the gas mixture can be determined, allowing the density to be determined from the measured Rayleigh scattering. Under conditions where the pressure and composition are known or can be determined and where the perfect gas law applies, the gas temperature can be inferred from the measured density.[9] Such measurements can suffer from interference from Mie scattering from particles and laser scattered light.[9] To avoid Mie

interferences, the gases can be filtered to remove particles. Careful experimental design and blackening of surfaces can minimize scattered laser light.

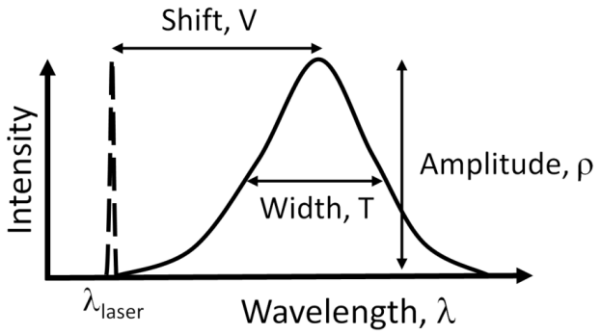

Figure 4.3. Notional sketch of spectrally dispersed Rayleigh scattered light (solid line) which has been Doppler shifted from the incident laser light (dashed).

Spectral analysis of Rayleigh scattering yields additional parameters that can be measured. Figure 4.3 shows a schematic of the dispersed Rayleigh scattered light (solid line), separated from the incident laser light (dashed line). The spectral shift of the Rayleigh from the laser is caused by the Doppler shift of the gas relative to the incident light beam and depends on the detection angle. The width of the Rayleigh spectrum depends, in part, on the gas temperature. The amplitude of the scattering, as described above, depends on the gas density (and composition). Thus, in principle, by spectrally dispersing the Rayleigh scattered light, the temperature, velocity, and density of a gas can be measured simultaneously. These effects are detailed below with examples given.

Revisiting Eq. (4.5), notice that for Raman scattering to occur, $\left(\frac{\partial \alpha}{\partial Q}\right)_0$ must be nonzero. This happens when a molecule exhibits a *change* in its polarizability with vibrational displacement. For example, as the atoms in the N_2 molecule vibrate, they become less polarizable as the atoms approach each other (charges exhibiting more force because they are closer to each other) and more polarizable when further apart (charges more weakly interacting). This results in a nonzero $\left(\frac{\partial \alpha}{\partial Q}\right)_0$. Such vibrations are *Raman active*. On the other hand, some vibrational modes do not change the molecule's polarizability, for example the asymmetric stretch of CO_2 has the following vibration pattern: O→ ← C O→. Such modes have $\left(\frac{\partial \alpha}{\partial Q}\right)_0 = 0$ and are termed *Raman inactive*. Further quantum mechanical selection rules and molecular structure considerations (atomic mass, bond length, moment of inertia, etc.) determine the shape and structure of the Raman spectra.[9] Since the frequency of Raman spectra depends strongly on the individual species' molecular structure (each vibrational resonance occurring at a different energy), Raman spectra from different molecules appear spectrally separated when they are dispersed, typically using a grating-based spectrometer equipped with a camera to acquire the spectra. Because Raman scattering is species-specific, it can be used to measure individual species concentrations, where in Eq. (4.6), *N* is the species being detected and the differential cross section is that of the individual species.

4.3 Advantages and Disadvantages of Rayleigh and Raman Scattering

Rayleigh and Raman scattering have many inherent advantages compared to other measurement techniques. Both use just a single laser and the laser need not be resonant with any particular molecular resonance as in absorption or laser induced fluorescence (LIF). This allows high-powered, fixed frequency lasers to be used for Rayleigh or Raman. Since they are linear laser techniques involving only a single excitation beam, Raman and Rayleigh are relatively easy to set up and understand, and the data are, in general, easier to analyze than nonlinear techniques like coherent anti-Stokes Raman spectroscopy (CARS). Neither Raman nor Rayleigh is sensitive to collisional quenching, a phenomenon which complicates the interpretation of LIF signals. Absolute intensity calibration of both techniques is relatively straight forward and easily performed. Raman and Rayleigh can be performed simultaneously using the same laser to measure species concentrations (Raman), temperature (Raman and/or Rayleigh), density (Raman and/or Rayleigh) and velocity (Rayleigh).

The major disadvantage of Raman and Rayleigh scattering is the low signal intensity. The low signal from Raman scattering generally prevents minor species (less than a few percent by mole fraction) from being detected using this technique. Because the signals are so low, large (low *f*-number) collection optics are usually used. Ideally, the detection optics need to be placed close to the measurement region. In ducted flows, large windows are required. Hypersonic and combusting flows can sometimes be luminous. Natural luminosity, like spontaneous Rayleigh and Raman scattering, emits light in all directions. In order to improve the signal-to-noise ratio, temporal, spatial, and spectral filtering can be used to collect the desired radiation and block unwanted natural luminosity. For example, gated detection of pulsed signals (or lock-in detection of continuous signals) can be used.

4.4 Translational Temperature, Velocity, and Density Measurements

The gas temperature and velocity can be determined from the Rayleigh spectrum by resolving the Doppler broadening and Doppler shift, respectively. The Rayleigh scattering linewidth is typically in the range of 1-6 GHz (0.03-0.17 cm^{-1}) for supersonic and hypersonic flow experiments in the range of a few hundred to a few thousand kelvins, depending on the temperature and angle of incidence of detection and collection of the light (see Ref. 139 for detailed information about the Rayleigh scattering lineshape and angular dependence). A high-resolution laser can be used so that the broadening caused by the laser's lineshape is negligible compared to this Doppler broadening. For example, injection seeded, pulsed Nd:YAG lasers typically have linewidths of about 0.1 GHz (0.004 cm^{-1}) while continuous sources can have linewidths that are orders of magnitude smaller. To spectrally resolve Rayleigh scattering, a high-spectral-resolution instrument is required. Two methods, described below and also in the introduction, are typically used: gas vapor cells and Fabry-Perot etalons.

A gaseous cell filled with iodine vapor can be used in combination with excitation in the visible wavelength range, where I_2 has many absorption lines, by placing a low-pressure gas cell containing crystalline iodine and I_2 vapor in front of a detector or camera. The diameter

of the cell should be larger than the diameter of the collection lens. The cell length, pressure and temperature of the I_2 cell are chosen to control the I_2 gas concentration and spectral line shape and therefore the absorption magnitude and profile. Attenuation of transmitted light by a factor of 10^5 can be achieved using high-resolution cw lasers, though it is more difficult to achieve attenuations greater than ~10^3 with off-the-shelf injection-seeded, pulsed Nd:YAG lasers.[146] The absorptions can be used to reject spurious scattered laser light, while passing the pressure- and Doppler-broadened and Doppler-shifted Rayleigh scattering, allowing background-scatter-free density measurements. These sharp absorption features can also be used for temperature and velocity measurements by using the steep edge of the absorption spectral profile to provide spectral resolution. Since the absorption spectrum of the gas filter is well known, if the laser frequency is scanned across the filter, then the Doppler-broadened and Doppler-shifted Rayleigh-scattered light will transmit through the filter, being acquired by the camera. Each pixel on the camera will then have obtained a convolution of the Rayleigh-scattered light with the absorption spectrum. These spectra can then be deconvolved to determine the gas temperature through the thermal broadening and gas velocity through the observed Doppler shift. Miles et al.[139] demonstrated this approach in a Mach 2 pressure-matched jet flow, shown in Fig. 4.4. Variations of this technique can provide both time-averaged and single-shot measurements. For single-shot measurements, the dynamic range of velocities that can be measured is limited, although by increasing the gas cell buffer gas pressure, the dynamic range has been increased by Elliot et al,. who made single-shot measurements with ~9% uncertainty over a velocity range from 200 to 600 m/s.[147,148]

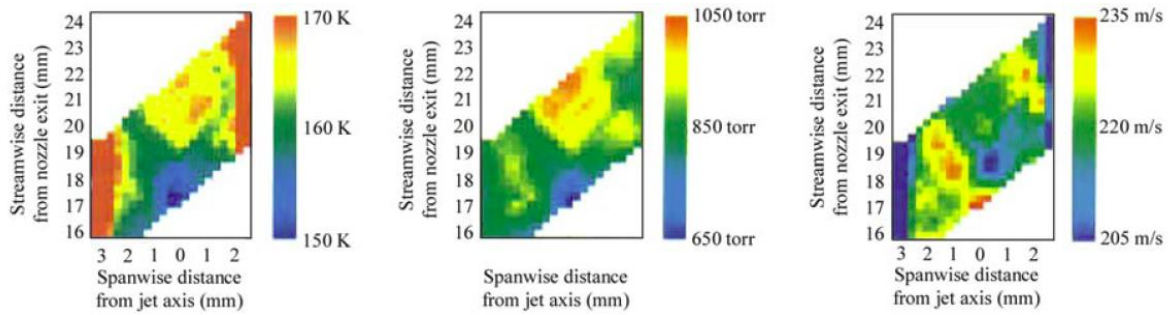

Figure 4.4. Temperature (left), pressure (center) and velocity (right) measured in a Mach 2 supersonic jet flow using Rayleigh scattering observed through a gas vapor cell using a frequency-scanned, injection-seeded Nd:YAG laser.[139] © IOP Publishing. Reproduced with permission of the authors and of IOP Publishing. All rights reserved.

By using a Fabry-Perot etalon, single-shot Rayleigh spectra can be obtained, allowing instantaneous (in ~100 ns) and simultaneous measurement of temperature, density and velocity. A Fabry-Perot etalon consists of two planar, reflective surfaces that cause interference, dispersing the transmitted light spatially, so that in the focal plane of the etalon, the spectrum of the light is separated spatially and can be resolved spectrally. Two different strategies have been developed to acquire these spectra. The first uses a CCD camera in the focal plane of the etalon to capture the dispersed spectrum.[149-152] The second method uses spatial masks or mirrors to direct the Rayleigh-scattered light to single-point detectors such as

photo-multiplier tubes (PMTs).[153,154] Typically, CCD cameras read out more slowly than single-point detectors such as PMTs, so using PMTs generally results in higher-speed detection. Measurement rates up to 32 kHz have been reported using this approach.[154] However, using a CCD camera offers several measurement advantages, described below.

Figure 4.5 shows one such example of CCD-based detection of Rayleigh-scattered light from Bivolaru et al.[151] A pulsed Nd:YAG laser is focused into a heated Mach 1.6 jet flow. The Rayleigh-scattered light is collected at right angles by a lens system that down-collimates the collected light and passes it through a solid etalon. The etalon-processed light is then focused on an electron-multiplying charged-coupled device camera (EMCCD) where the interference fringes are realized. This image is called an interferogram. An optical fiber (OF) directs some of the spectrally narrow laser light into the optical path so that a circular reference fringe will appear in the interferogram, as in Fig. 4.6(a). The pair of oval patterns located in the white rectangle show Doppler-shifted, Doppler-broadened, Rayleigh-scattered light collected by the lenses and dispersed by the etalon. A similar pattern is shown on the left side of the interferogram. These four oval patterns originate from four different spatial locations a few mm apart in the flow, thus resulting in four simultaneous, spatially-separated measurements. The gas velocity, $\boldsymbol{V}$, and the Doppler shift, Δf, are related by: $\Delta f = ((\boldsymbol{k_s}-\boldsymbol{k_o})\cdot \boldsymbol{V})/\lambda$, where λ is the wavelength of the incident light, $\boldsymbol{k_o}$ is the wave vector of the incident light and $\boldsymbol{k_s}$ is the wave vector of the collected light. (The wave vector points in the direction of light propagation and has a magnitude of $2\pi/\lambda$.) In the vector diagram shown in Fig. 4.5, $\boldsymbol{k_{o1}}$ is the wave vector of the incident light and $\boldsymbol{k_{s1}}$ is the wave vector of the collected light. The observed Doppler shift measures the velocity component V_1 in the direction defined by $\boldsymbol{k_{s1}} - \boldsymbol{k_{o1}}$, which bisects the angle β between the laser and collection wave vectors. Similarly, a mirror M_r reflects this incident beam back through the lens, L_2, and into the measurement volume with wave vector $\boldsymbol{k_{o2}}$ resulting in collected Rayleigh signal having a wave vector $\boldsymbol{k_{s2}}$. This signal is sensitive to the velocity component V_2. The reflected beam was slightly misaligned in the downward direction so that the two measurements would be spatially separated on the interferogram, shown in Fig. 4.6(a). Furthermore, the geometry of this experiment was constructed so that the V_1 would be orthogonal to the jet axis, measuring a radial velocity component while V_2 was parallel to the jet axis, measuring the axial velocity component. In Fig. 4.6(a), four spatially separated measurements of axial velocity are collected in the bottom half of the interferogram while four measurements of radial velocity are collected in the top half. Figure 4.6(b) shows the two boxed peaks after they have been processed to linearize the interferograms and to bin the data into single spectra.[150,151] These spectra were fitted with Gaussian curves to determine the Doppler shift and broadening associated with Rayleigh scattering, relative to the reference peaks. Subsequent work by this team and others has been able to simultaneously determine the gas velocity, temperature and density from similar spectra.[155,156]

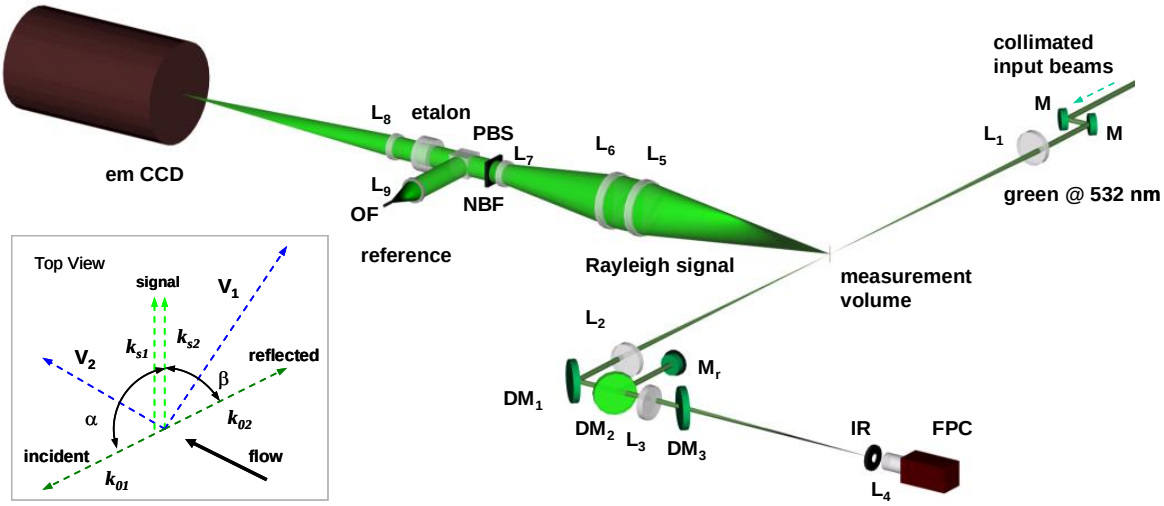

Figure 4.5. Two-component interferometric Rayleigh scattering system from Ref. 151. Mirrors are denoted by M, dichroic mirrors by DM and lenses by L. PBS is a polarizing beam splitter while NBF is a narrowband filter. IR is an iris and FPC is a focal plane camera used to monitor the beam alignment. In this experiment, the dichroic mirrors were required to filter out other laser beams associated with a dual-pump CARS measurement that was being performed simultaneously. Reprinted with permission of the authors.

In Ref. 151, Bivolaru et al. reported velocity measurements with a precision of ~40 m/s in a flow with ~1200 m/s, or about 3% of the maximum velocity. The dynamic range of the instrument was ~3000 m/s. (The dynamic range is mainly determined by the thickness of the etalon, which sets the free spectral range, or fringe-to-fringe spectral separation.) Thus, expressed as a percentage of the dynamic range of the instrument, the measurement precision is ~1%. To obtain more precise measurements at lower temperatures, the experiment can be designed to use higher spectral resolution.

The use of the camera-based approach has some advantages over the PMT-based approach. First, it can tolerate (and in fact, benefits from) scattering from stationary surfaces

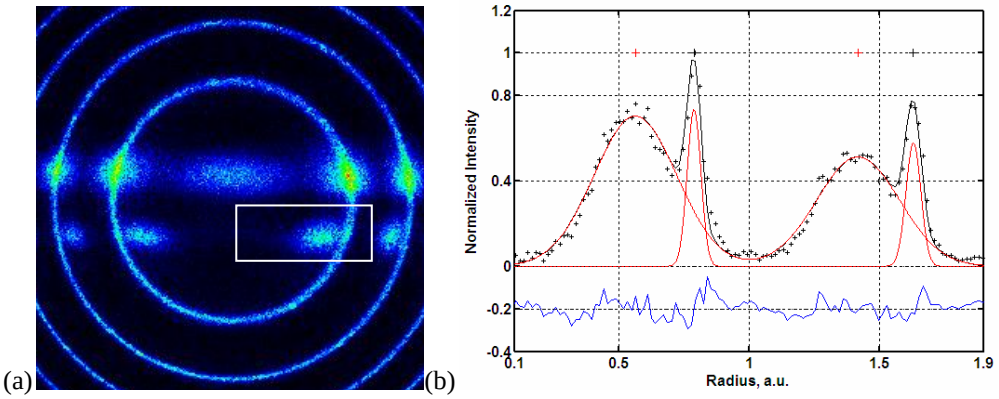

Figure 4.6. (a) Fabry-Perot interferogram of Rayleigh-scattered light obtained by laser beams from two different directions as well as laser-light, resulting in the circular pattern. (b) the linearized Rayleigh-scattered spectrum obtained from the boxed region in (a), showing best fits to the reference and Doppler-shifted light.[151] Reprinted with permission of the authors.

in the flow. Such scattering, as long as it is not too large, provides a reference frequency to determine the Doppler shift. Second, having a laser frequency reference in each interferogram makes the system insensitive to variations in the etalon transmission spectrum or the laser wavelength. In typical PMT-based experiments, the etalon must be temperature controlled, vibration isolated (if it is an air spaced etalon) and the laser frequency must be carefully controlled. Uncontrolled drift in either the etalon or laser would result directly in a systematic error in the PMT-based approach while it is automatically corrected in the CCD-based approach. A third advantage of the CCD-based approach is that it is somewhat more tolerant of scattering from clusters and particles in the flow, lessening the need for gases to be filtered. Scattered light from particles typically appears in CCD-based interferograms as spatially distinct, circular artifacts. These can sometimes be removed by image processing. However, if the scattering is too large either spatially or in intensity, it can corrupt the measurement; even in this case, other spatial locations in the flow may yield measurements from the same interferogram. As shown in Fig. 4.6, the CCD-based detection allows multiple spatial points to be measured simultaneously, allowing measurements at adjacent spatial locations to be correlated. Furthermore, with CCD-based detection, it is straightforward to measure multiple velocity components with the same instrument, also shown in Fig. 4.6. Finally, CCD-based detection has often been combined with pulsed-laser excitation, which has two benefits: it makes the measurement instantaneous, occurring in ~10 ns, and the signal intensity is much higher, allowing measurement in much lower density flows, such as atmospheric-pressure flames and low-pressure gas flows. Instantaneous measurements at 1/5 of atmospheric density or lower are possible with this approach.[151]

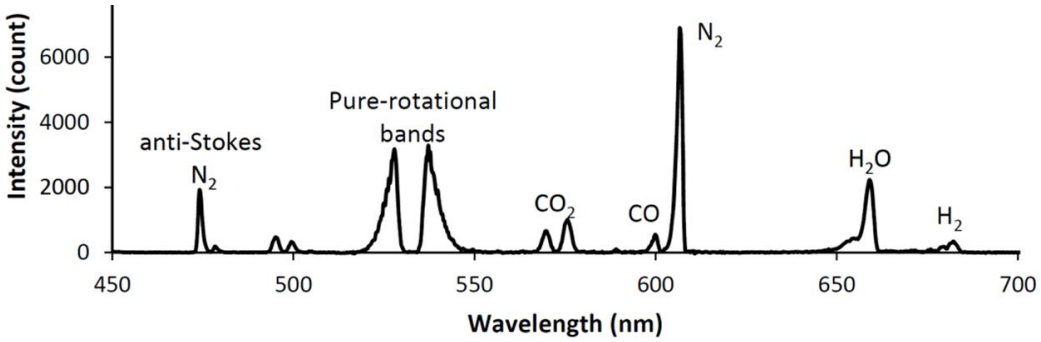

Figure 4.7. Five-hundred-pulse-average Raman spectrum in a high-pressure CH_4 air flame. The excitation laser wavelength was 532 nm. A 532 nm filter blocks Mie, Rayleigh and spurious laser scattering as well as some of the low-rotational-quantum-number rotational Raman lines. A subframe burst gating (SBG) technique was also used to subtract background emission from this spectrum.[157] Figure courtesy of and with permission of J. Kojima, NASA Glenn Research Center.

4.5 Rotational and Vibrational Temperature Measurements

Raman scattering is sensitive to individual molecular rotational and vibrational transitions. Since the population of these lines depends on (actually defines) the temperature, it is possible to measure rotational and vibrational temperatures from spontaneous Raman spectra. Figure 4.7 shows a typical Raman spectrum obtained in a hydrocarbon-air flame at high pressure.[158] A pulse-stretcher was used to extend the duration of the 500-mJ, 532-nm pulse by nearly a factor of 10, thereby lowering the peak laser power to avoid laser-induced breakdown while maintaining high pulse energy to yield a sufficiently high signal-to-noise ratio.[158] This spectrum shows many temperature and concentration dependent features. The relative heights and shapes of the different bands depend on temperature and gas concentration. Modeling, calibration and analysis of such Raman spectra can yield rotational and vibrational temperatures as well as concentrations. Several different strategies for temperature measurement based on spontaneous Raman scattering exist. Rotational temperatures can be measured from pure-rotational Raman scattering either using high-resolution or low-resolution detection, as indicated in Fig. 4.8.[159] The advantage of low-resolution detection is that the spectrum can be acquired simultaneously with the same instrument used to acquire multi-species spectra like that shown in Fig. 4.7. A disadvantage of this low-resolution technique is that many different species have similar pure rotational Raman shifts, so they overlap in the same spectral region close to the excitation laser. Such interferences from different species can lead to measurement errors. This technique works over a wide temperature range, including at room temperature. Alternately, rotational temperatures could be determined by resolving the rotational-vibrational Raman scattering, typically of N_2,[160] as is often done for CARS.[161] When flows are in rotational-vibrational equilibrium, it is more common to measure the temperature using vibrational bands, as described below, because they result in higher signal-to-noise ratios and consequently, more precise temperature measurements.

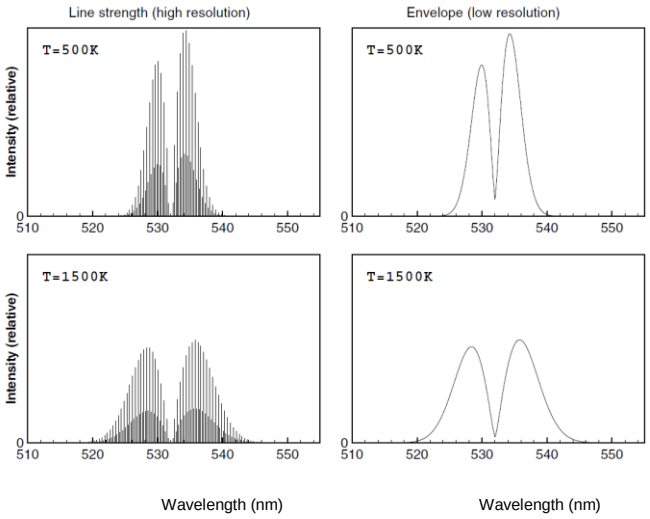

Figure 4.8. Theoretical calculation of the pure rotational Raman spectra of N_2 at two different temperatures and two different spectral resolutions, adapted from Ref. 159. © IOP Publishing. Reproduced with permission of the authors and of IOP Publishing. All rights reserved.

Vibrational temperatures can be measured from the relative heights of different vibrational Raman bands. A commonly used method compares the ratio of the Stokes to anti-Stokes (S-AS) vibrational Raman bands of N_2.[9,162-164] N_2 is often used because it is present in high concentration in many supersonic, hypersonic, and combusting flows, resulting in

adequate signal-to-noise ratio. Also, N_2 is used because it is relatively well understood and well resolved spectrally from other species. Recall from Fig. 4.1 that the anti-Stokes scattering originates from an excited vibrational state, whereas the Stokes scattering can originate from the ground vibrational state. Thus, the integrated intensity of the anti-Stokes N_2 spectrum at 473 nm in Fig. 4.7 can be compared to the Stokes scattering at 607 nm. This ratio, which is a monotonic function of temperature, can be used to determine the temperature. Since this method integrates the signal intensity in the two different bands, it improves the signal-to-noise ratio, allowing single-shot determination of temperature. Single shot precisions of ~20% of the measured temperature have been obtained at several points along a line using this method.[162] This technique becomes insensitive to temperature below about 700 K because the low population in the excited vibrational state causes low signal-to-noise ratio.[9]

A second method of measuring the vibrational temperature is to spectrally resolve the different vibrational bands of a molecule such as N_2, though the individual rotational lines need not be resolved. The relative heights of the vibrational levels can be plotted on a Boltzmann plot or can be fitted spectrally to determine the vibrational temperature.[165] For example, Sharma and coworkers[165] used a KrF excimer laser operating at 248 nm to generate spontaneous Raman scattering in the Electric Arc Shock Tube (EAST) facility at NASA Ames Research Center. The EAST facility, normally operated as a shock tube, was fitted with a two-dimensional converging-diverging nozzle so that a shock reflection generated a high pressure (100 atm), high temperature (5600 K) reservoir of N_2 gas that expanded through the nozzle. The sudden expansion through the nozzle results in vibrational-rotational nonequilibrium, which was monitored with Raman scattering. Measurements were performed at different distances downstream to study the evolution of the vibrational relaxation. Figure 4.9 shows a sample spectrum generated and spectrally fit to determine the rotational and vibrational temperatures. The vibrational temperatures were then plotted versus distance downstream in the flow so that different vibrational relaxation models could be tested.[165] Though not explicitly stated in the paper, the temperature measurement precision appears to be about 5%.

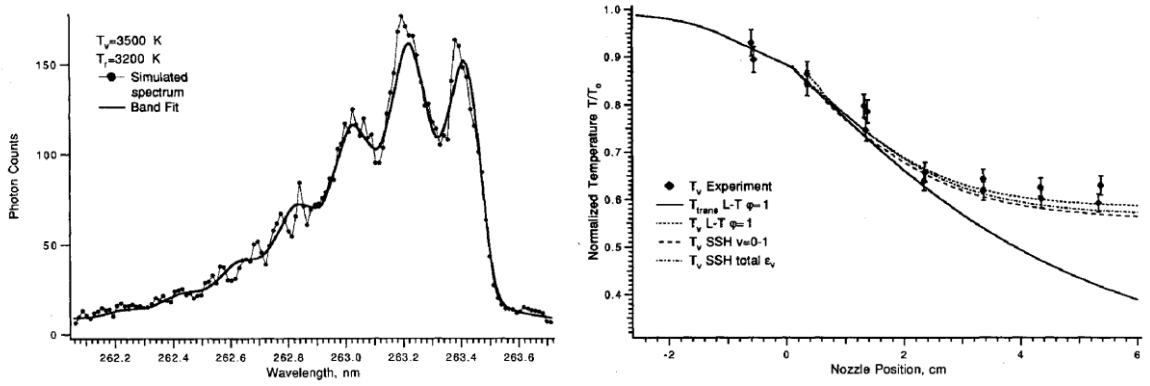

Figure 4.9. An experimental Raman spectrum of N_2, fitted for rotational and vibrational temperature (left), and resulting vibrational temperatures measured as a function of distance downstream of the nozzle (right), adapted from Ref. 165 with permission of the authors.

4.6 Species Concentration Measurement

Rayleigh scattering has been used in some specialized experiments for determining species concentration. For example, the Rayleigh scattering cross section for propane is 13.5 times larger than for air, allowing mixing to be quantified in propane/air jets.[166] However, *Raman* scattering is much more commonly used to measure species concentrations. Sandia National Laboratories have extensively used Raman scattering for major-species concentration measurements (along with Rayleigh and LIF measurements for temperature and minor-species concentration measurements, respectively).[65] This system uses a series of four frequency-doubled Nd:YAG lasers to produce temporally-stretched 1.8 Joule pulses which are focused to a 0.22 mm ($1/e^2$) diameter spot size. A separate laser excites LIF of CO. An imaging system directs the collected Raman/Rayleigh/LIF scattered light into the optical analysis system shown in the bottom-right panel of Fig. 4.10. The system contains two mechanical chopper wheels (one "slow" and one "fast") that are synchronized with the laser to transmit the signals while rejecting flow luminosity. It also has a transmission grating and multiple lenses, beam splitters and cooled (low noise) CCD cameras. This system images a 6-mm-long segment of the Rayleigh, Raman and LIF probe volume, allowing concentrations and temperature to be obtained along a line. The spatial resolution for the Raman measurements was ~10 pixels / mm along the 6-mm-long probe volume, though the actual spatial resolution was slightly worse due to optical distortions from the flame.[65]

A sample of the resulting concentration measurements is shown in Fig. 4.10. Raman has been used to measure N_2, O_2, CH_4, CO_2, H_2O and H_2 while CO was measured with two-photon LIF excited at 230.1 nm. Temperature was measured from the intensity of the Rayleigh-scattered light, using the ideal gas law to convert density to temperature as described above. The data are graphed versus temperature to show the correlation of species with temperature and to allow comparison with an unstrained flame calculation, shown in blue. The individual (red) data points correspond to different single pulses of the laser. Thus, these measurements are 'single shot' having been obtained with flow freezing (~100 ns) time resolution. Data such as these have been acquired at many locations in a variety of different flames, allowing the development of a large database of turbulent flames. The accuracy of the Raman concentration measurements varies from 2% to 10% of the measured concentration, while the precision (based on one standard deviation) varies from 0.7% to 7.5% depending on the species. The accuracy of the temperature measurement, based on Rayleigh scattering signal intensity, was reported to be 2% with a 1-σ precision of 0.75%.

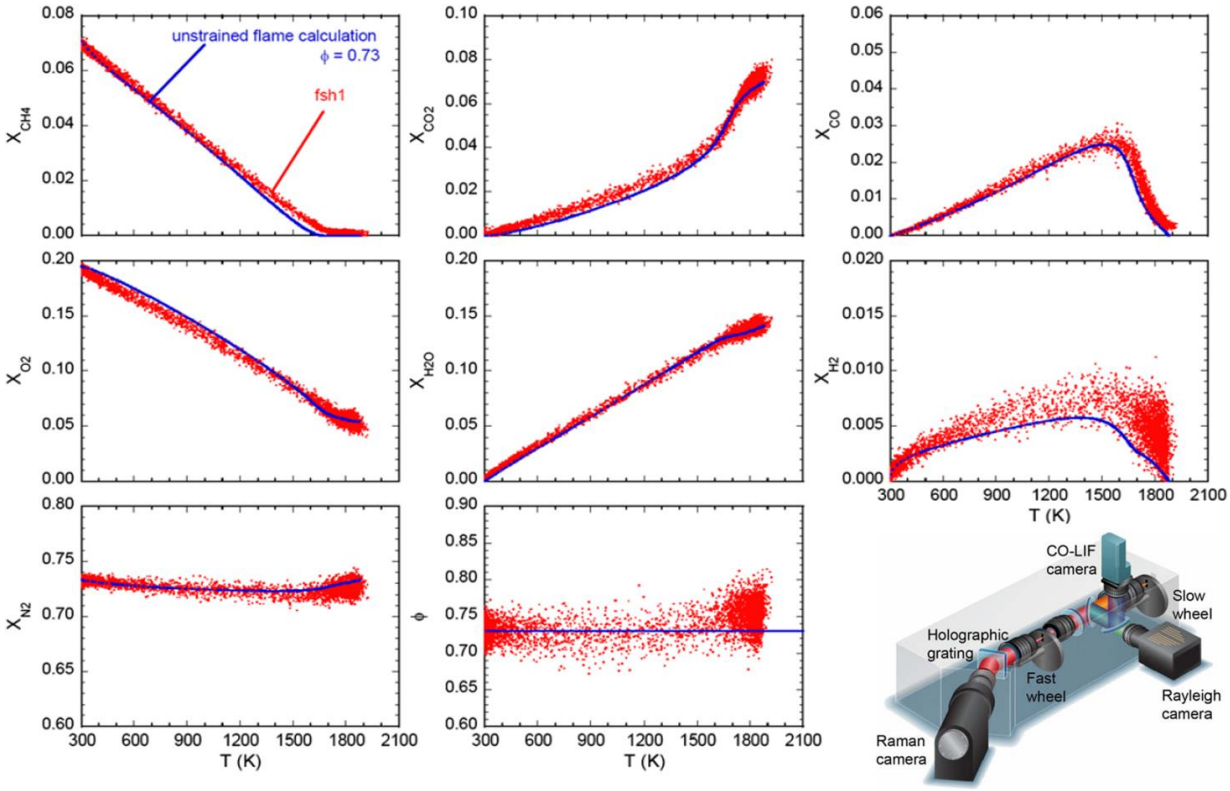

Figure 4.10. Scatter plots of mole fraction and equivalence ratio (ϕ) data at one location in an atmospheric pressure, methane-air flame compared with a calculation, and a schematic of the optical components associated with the collection and analysis of light from the Sandia Raman/Rayleigh/LIF imaging system (bottom right). Adapted from Ref. 65 with permission of the authors and the The Combustion Institute.

5. Coherent Anti-Stokes Raman Spectroscopy

5.1 Introduction

Comprehensive reviews of the theory and application of Coherent anti-Stokes Raman spectroscopy, often called coherent anti-Stokes Raman *scattering*, or CARS, in a gas have been given by others.[9,18] A brief introduction and overview are provided herein. CARS is a non-linear optical process in which three laser beams interact with the gas generating a fourth, laser-like signal beam. The energy level diagram of this process (each arrow represents a change in state due to photon absorption, an up arrow, or emission, a down arrow, and the length of the arrow is proportional to energy change or, equivalently, photon frequency) is shown in Fig. 5.1

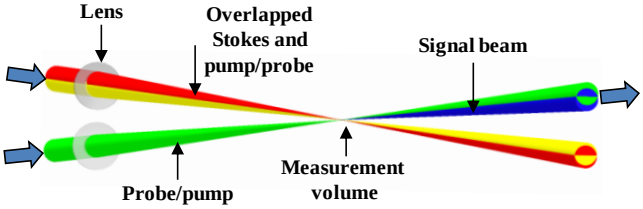

Figure 5.2. Planar BOXCARS beam geometry.

The pump beam and the lower frequency Stokes beam interact with the gas, a pump frequency photon is absorbed and a Stokes frequency photon is emitted coherently with the Stokes beam, and the gas is excited to a higher energy state via a state that in most CARS setups is a virtual state (although it could also be a real state). The difference between the frequencies of the upper and lower state, $\omega_{pump} - \omega_{Stokes}$, is called the Raman shift. A probe beam photon is coherently scattered from this excited state, shifted up in frequency by the Raman shift to form part of the signal beam, and the gas molecule returns to its original state. Total momentum as well as energy is conserved. Therefore, the momentum of the scattered photons equals that of the incident photons, leading to the following equation:

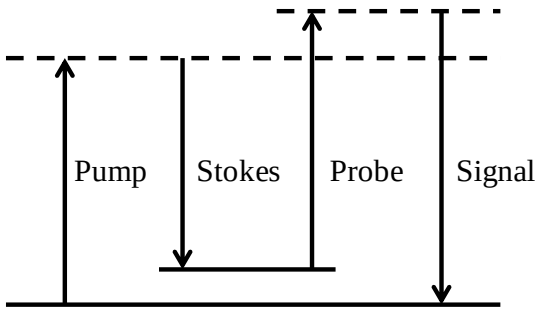

Figure 5.1. Energy level diagram showing the CARS process.

$$\overrightarrow{k_{pump}} + \overrightarrow{k_{probe}} = \overrightarrow{k_{Stokes}} + \overrightarrow{k_{signal}} \tag{5.1}$$

Since the *k*'s are the wave vectors (length proportional to photon frequency with the same direction as the beam), this equation allows the direction of the signal beam to be found from the directions of the pump, Stokes, and probe beams.

A physical interpretation of this process is that the interaction of the pump and Stokes beams establishes an optical fringe pattern in the gas. If the pump and Stokes frequencies are the same, as with a related technique called degenerate four-wave mixing (DFWM), this fringe pattern is stationary. In CARS, the frequencies are different and the fringe pattern moves across the interaction region, modulating the intensity at any particular point at the beat frequency, i.e., the Raman shift frequency. This moving fringe pattern excites a polarization response in the gas which acts as a moving grating from which a probe beam photon is scattered, in a manner similar to Bragg scattering, to form the signal beam photon. Since the grating is moving, the frequency of the signal photon is shifted relative to the probe photon by the Raman shift frequency. (An analogous effect occurs in an acousto-optical modulator where acoustical waves in a solid material, such as glass, form a moving grating of varying index of refraction, and incident laser light is coherently or Bragg scattered from this volumetric "grating" with its frequency shifted by the acoustical frequency.[167])

If the pump, probe, and Stokes lasers are all single frequencies, then the signal is also at a single frequency, as indicated in Fig. 5.1. If the pump and/or Stokes lasers are broadband lasers, while the probe is single frequency, then the signal is also broadband, and contains a spectrum that reflects the variation of CARS susceptibility of the molecules in the probe volume as a function of Raman shift. In many broadband CARS setups, the probe and pump frequencies are the same (derived from the same laser source). In the dual-pump CARS technique, [9,168] pump and probe frequencies are different and these two laser beams have interchangeable roles (each beam performs the role of pump in one CARS process and probe in a second CARS process). The signal is thus the coherent superposition of the signal from

the two processes, generated over two different ranges of Raman shift. When the desired Raman shift is small, as in rotational CARS (i.e., when the transitions probed are pure rotational transitions, which differ by relatively small quanta of energy and are thus relatively closely spaced spectrally), the pump and Stokes beams can be derived from the same broadband laser while the probe beam is single frequency (dual-broadband CARS).[9]

Since CARS is a non-linear process (see Section 1.2) it requires high irradiance levels. Consequently, CARS signal in a gas is typically generated by focusing pump, Stokes, and probe beams, and overlapping them at their common focus. If the beams are initially separate and crossed at the common focus, the arrangement is called BOXCARS; if they lie in a plane (Fig. 5.2), it is called planar BOXCARS. In this arrangement the measurement volume is the small region of overlap of all three beams.

5.2 CARS Theory[9,18,167]

CARS, like Raman and Rayleigh scattering, arises because of time-varying polarization induced in the gas in the presence of electromagnetic radiation. CARS, specifically, arises due to the third order susceptibility, χ_{CARS}, for which the induced polarization is described as follows:

$$P^{(3)}\left(\omega_{signal}\right) = \epsilon_0 \chi_{CARS} E(\omega_{pump}) E(\omega_{Stokes}) E(\omega_{probe}) \tag{5.2}$$

The *E*'s are the complex electrical field amplitudes. This equation can be substituted into the wave equation relating the electrical field to the induced polarization and solved by integration along the direction of the signal beam. The CARS irradiance is thus:

$$I_{signal} \propto I_{pump} I_{Stokes} I_{probe} |\chi_{CARS}|^2 L^2 \tag{5.3}$$

L is the length of the measurement volume, i.e., the length of the region along which the pump, Stokes, and probe beams all overlap. Rigorous calculations of the CARS susceptibility require quantum mechanical treatments, but classical derivations are simpler to understand. The gas is modeled as a simple harmonic oscillator in which the variation of the normal coordinate, *Q* (intermolecular spacing in the case of vibrational states), with time is described by a second order linear ordinary differential equation, with a time-dependent forcing function proportional to the average over an optical cycle of the square of the electrical field. (Thus, the forcing term oscillates at the Raman shift frequency.) The constant of proportionality in the forcing term is proportional to $\left(\frac{\partial \alpha}{\partial Q}\right)_0$, and consequently to the Raman scattering cross section, where α is the optical polarizability of the molecule. The CARS susceptibility is found by solving for the time dependence of the normal coordinate, combining with Eqs. (5.1) and (5.2) for the polarization (from the chapter on Rayleigh and Raman scattering), and comparing with Eq. (5.2):

$$\chi_{CARS} \propto \frac{N\left(\frac{\partial \sigma}{\partial \Omega}\right)}{\Delta\omega\left(2-\frac{\Delta\omega}{\omega_v}\right)+i\left(1-\frac{\Delta\omega}{\omega_v}\right)\Gamma} \tag{5.4}$$

The susceptibility is proportional to the molecule number density, *N*, and the differential Raman cross section, $\left(\frac{\partial\sigma}{\partial\Omega}\right)$, and reaches a peak where the detuning, $\Delta\omega \equiv \omega_v - \left(\omega_{pump} - \omega_{Stokes}\right)$, approaches zero. The damping coefficient, Γ, determines the line width. A quantum-mechanical treatment yields the following equation:

$$\chi_{CARS} = \sum_j \frac{K_j \Gamma_j}{2\Delta\omega_j - i\Gamma_j} + \chi_{nr} \text{ where } K_j \propto N\Delta_j \left(\frac{\partial\sigma}{\partial\Omega}\right)_j \quad (5.5)$$

The index *j* refers to a particular transition and Δ_j is the fractional difference in the population of the two states of the gas between which a transition is taking place (the two real levels in the energy level diagram of Fig. 5.1); χ_{nr} is the non-resonant susceptibility, a nearly constant term for the CARS process in which all the states in Fig. 5.1, other than the ground state, are virtual states. The (real part of the) line shape in Eqn. (5) is a Lorentz function with full-width at half maximum equal to Γ_j. This line shape is the same as the (complex conjugate of the) line shape for the classical solution when the detuning is small relative to the vibrational frequency. The line width depends inversely upon the lifetimes of the two states involved in the transition, which depend upon the rate of collisions between molecules (collisional broadening). Light emitted by molecules in motion is observed at a slightly different frequency by a stationary observer by an amount proportional to the velocity component towards the observer. This effect, when averaged over many molecules travelling in different directions, results in Doppler broadening. Since the distribution of molecular velocity components about the bulk mean in a gas in equilibrium is Gaussian, the line shape becomes a Voigt profile: a convolution between Gaussian and Lorentzian functions. At pressures much above atmospheric, additional line narrowing effects occur.

Since the CARS signal is proportional to $|\chi_{CARS}|^2$, a CARS spectrum reflects the populations of the molecular energy states involved in the transitions. Since these populations, in equilibrium, are related via the Boltzmann equation to the temperature, CARS can measure temperature. Integrated CARS signal is also strongly dependent upon number density and, in principle, could be used to measure density. This is not typically done because of experimental difficulties in maintaining a consistent geometry of the laser beams at the beam intersection. Small uncontrolled motions of the beams due to refraction in inhomogeneous gas fields, movements of the optical system, variation in the quality of the laser beams, etc., cause changes in signal intensity, and calibrations fail. However, where two gas species are resonant in a spectrum, the ratio of the population of one species to another may be found from the shape of the spectrum. Where only one species present is resonant, but χ_{nr} is known, the fraction of that species may be found from the relative amplitude of the resonant signal to the non-resonant "background"; however, χ_{nr} depends on the number density of all species present. If all species but one are resonant in the spectrum then the composition can be fully determined by reference to the non-resonant background.[169] Use of CARS as a diagnostic tool requires comparison of experimental and theoretical spectra. [170] Calculation of theoretical spectra is quite complex and numerically time-consuming: after computation of theoretical susceptibility, spectra must be convolved with laser line shapes and instrument probe function.[171]

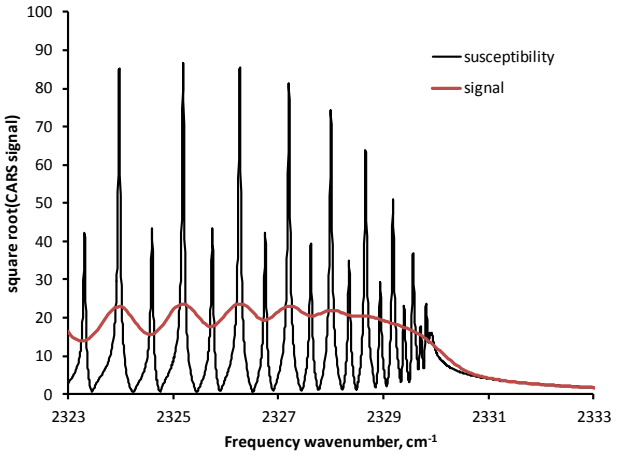

Figure 5.3. CARS N_2 Q-branch susceptibility and spectrum near band head at 1 atm., 1400 K.

Nitrogen is a very useful species for measurement of temperature since it is usually present in fuel-air combustion or hypersonic flows, and is readily probed by CARS. The band head of the N_2 Q branch is located at a Raman shift of 2330 cm^{-1} (units of inverse wavelength, proportional to frequency divided by the speed of light), and is readily accessible using available lasers. The Q branch occurs as a result of transitions between adjacent vibrational states ($\Delta v=+1$, where v is the vibrational quantum number) with no change in the rotational state ($\Delta J=0$, where J is the rotational quantum number). Figure 5.3 shows a portion of the N_2 Q-branch spectrum near the band head. Transitions are between v=0 and v=1and each peak corresponds to a different J value. Since rotation of the molecules affects the energy associated with a given vibrational state, the energy difference between v=0 and v=1 (at given rotational level) is a function of the rotational level. Two spectra are shown in this figure – the first is the CARS susceptibility and the second is a computed typical broadband CARS spectrum formed by convolution of typical laser line shapes and a typical instrument function with the susceptibility.[171] As may be seen, line shapes are typically not fully resolved in experiments.

Figure 5.4 shows the sensitivity of the signal spectrum to (a) temperature and (b) concentration. The calculations are for (a) air and (b) either air (79% N_2) or 10% N_2, 21% O_2, 69% H_2O, with a pressure of 1 atmosphere. The CARS signal strength varies strongly with temperature, partly through the effect of temperature on density (N) via the N^2 dependence of the CARS susceptibility. By using the Sandia CARSFT code,[170] the pressure and temperature dependence was determined to be proportional to $p^2T^{-3.5}$ at moderate to high pressures.[172] However, the shape of the spectrum also changes. At low temperature, only one vibrational band is present, associated with v=0 to v=1 transitions, and is relatively narrow (because fewer J levels are occupied). At the higher temperatures, "hot" bands are present also, associated with v=1 to v=2 and v=2 to v=3 transitions, and more J levels are populated. As the fraction of N_2 is reduced, the amplitude of the band structure becomes smaller relative to the non-resonant background, and sensitivity to N_2 is lost for concentrations less than a few percent. This lack of sensitivity below a few percent is typical and prevents measurement of minor species, although a number of CARS techniques, for example *resonance* CARS (e.g., Ref. [173]), have been developed to circumvent this limitation.

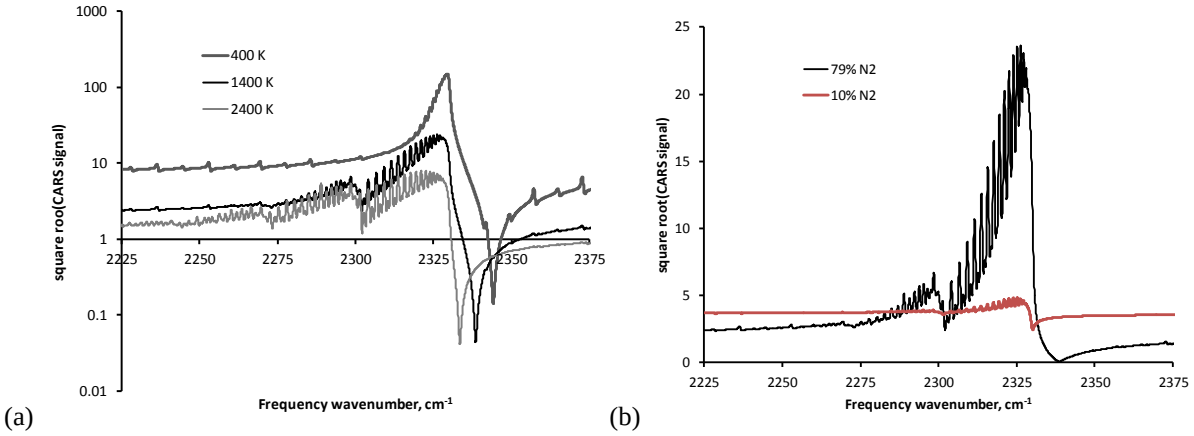

(a) (b)

Figure 5.4. Effects of (a) temperature and (b) concentration on the CARS N_2 Q-branch spectrum.

5.3 Ultrafast CARS

Ultra-fast techniques have been surveyed by Roy et al.[174] The CARS technique as described above is a steady-state process involving the mixing of four beams simultaneously present. For given laser energy available in the pump, probe, and Stokes laser beams, the energy in the signal beam is proportional to t^{-2}, where t is the time over which the measurement is made. Nanosecond (ns= 10^{-9} s) CARS is performed with Q-switch pulsed lasers where the pulse energy is distributed over 5 ns to 10 ns, at a pulse rate on the order of 10 Hz. There are many 10's or 100's of thousands of Raman frequency cycles during each laser pulse, so that CARS is effectively a steady-state process. However, with the advent of femtosecond (fs= 10^{-15} s) lasers (e.g., titanium-sapphire), very short pulse widths of order 10^{-14} seconds are possible at high pulse repetition rate (1 kHz or more), and the pulse width is less than the period of a Raman cycle. Due to the t^{-2} scaling, strong signal energy is available with modest pulse energy.

The theory of fs CARS is different from ns CARS since a steady state problem is replaced with an impulsively initiated, time-dependent one.[175] First, a polarization grating is established in the gas by the interaction of pump and Stokes beams. This grating evolves in time through rotational-vibrational relaxation and then, after some delay (typically up to several hundred picoseconds in measurement applications), a signal is generated by scattering the probe pulse off the grating. By making measurements at different probe delays the relaxation of the grating, which carries with it an imprint of the vibrational and rotational state of the probed molecules, may be observed. "Chirping" techniques have been developed where the probe beam is broadened both temporally and spectrally in such a way that the frequency of the probe varies with time. The temporal relaxation is thus mapped into frequency space, obtained in a single laser pulse, and may be analyzed with an optical spectrometer.[176]

Picosecond (ps = 10^{-12} s) CARS employs mode-locked solid state lasers with pulse lengths on the order of 10 ps and has characteristics of both ns and fs CARS. As with fs CARS, generation of the grating by the pump and Stokes beams, and scattering of the probe to form the signal, are typically separate steps. However, the probe pulse is still relatively

long compared with the Raman cycle period, and the signal contains an optical spectrum similar to that of ns CARS.[177] An advantage of ps CARS over ns CARS is that the ps pulses required to obtain adequate signal-to-noise ratio CARS spectra are better suited to pass through commercially available optical fibers without damaging the fibers.[178] Both fs and ps CARS have the potential advantages over ns CARS of much higher data (pulse) rates and the absence, when the probe is delayed relative to the pump-Stokes laser pulses, of non-resonant background effects. Another advantage of fs CARS is simpler theoretical modeling, since few or no collisions occur in the time of the measurement (negligible collisional effects).[174]

5.4 Advantages and Disadvantages of CARS for probing Supersonic, Hypersonic and Nonequilibrium Flow

In hypersonic propulsion systems (scramjets), flow velocities are supersonic in inlets and nozzles, and may be supersonic or a mixture of subsonic and supersonic in the combustors. In combustors, pressures are roughly one atmosphere while temperatures are similar to those of low speed combustion. Thermal non-equilibrium (not typically present in low speed combustion) as well as chemical non-equilibrium can be present due to the short flow through time (on the order of milliseconds). CARS has several advantages in this application. The signal comes as a laser beam, which means that it can be collected through a relatively small aperture and may be separated from non-coherent interferences by spatial filtering. This is particularly useful in an engine combustor where there may be emission from the gases and thermal radiation from the wall, and where, for structural reasons, it may not be possible to incorporate large windows. Typical CARS measurements are spatially and temporally resolved, with ~1.5 mm long and 50 μm diameter measurement volume, and a 10 ns time scale. CARS is able to non-intrusively measure local temperature and composition. Since the Q-branch spectrum reflects the rotational-vibrational state of the molecule, the populations of these states may be directly determined, which is useful when thermal equilibrium (and therefore a single "temperature") does not exist.

CARS has been used much less frequently in hypersonic freestreams, where temperatures and pressures can be very low. Due to the previously-mentioned $p^2T^{-3.5}$ scaling of the CARS signal, the signal to noise ratio may be low. At low temperatures only the vibrational ground state and far fewer rotational states of molecules are populated. Vibrational CARS (e.g., of the N_2 Q-branch) then depends upon measuring high resolution spectra of the rotational structure of the "cold" band near the band head, which depends upon the pressure-dependent collisional effects on line shape, as well as temperature. Measurements of both pressure and temperature, at pressures down to about 0.1 atm., have been made in an underexpanded supersonic jet using this approach.[179] If the v>0 bands are populated at low rotational temperature (vibrational non-equilibrium), this can be easily measured. Alternatively, pure rotational CARS ($\Delta v=0$, $\Delta J=\pm 2$) is sometimes used at low temperatures since the lines have greater separation than in the Q-branch, but no information on the vibrational state is obtained.[180]

In nonequilibrium flows CARS has a significant advantage that it can simultaneously monitor multiple individual state populations. Thus non-Boltzmann distributions can be

probed, as in the examples below. Using vibrational broadband CARS, separate rotation and vibrational temperatures can be determined from CARS spectra.

CARS has some disadvantages compared to other measurement techniques. It typically measures at only a single point, and so does not typically provide simultaneous information at multiple spatial locations. Instead, the probe volume is typically scanned around the flow allowing time-averaged spatial properties to be measured. The data rate is low in ns systems (order 10 Hz) so that in pulsed hypersonic facilities only one single measurement is obtained per facility run. Also, its ~1.5 mm long probe volume can be too large in certain applications where it is desired to resolve small length scales such as shock waves, shear layers or turbulent eddies. Many of these limitations are being overcome with fs CARS, where 1D[181] and 2D[182] imaging have been demonstrated recently with smaller probe volumes and data acquisition rates in the kHz regime have been achieved.[174] CARS requires optical access on two sides of the flow, which may limit application in some facilities. The experimental setup for CARS, involving two or three pulsed laser systems along with large spectrometer(s), is relatively complicated and time consuming to set up. Furthermore, the nonlinear nature of the theory of CARS complicates the interpretation and analysis of the resulting spectra. However, with the combination of accurate and precise temperature and multi-species measurement capabilities, CARS is commonly used in many supersonic, hypersonic, and nonequilibrium flow applications.

5.5 Mole Fraction and Nonequilibrium Temperature Measurement

Extensive dual-pump CARS measurements have been made in a dual-mode scramjet burning hydrogen.[183] The experiments were conducted in a facility which provided electrically heated clean air to the scramjet combustor via a Mach 2 nozzle. The CARS lasers, which were located outside the scramjet lab, consisted of an injection-seeded Nd:YAG, frequency doubled to 532 nm, an in-house broad band dye laser (Stokes laser) centered around 603 nm with FWHM of 10 nm, and a commercial narrow-band dye laser centered around 550.5 nm. Beams were relayed to the experiment via a translation system that could move the measurement volume and through special slotted windows in the scramjet. Beams were focused and crossed in the scramjet in a planar BOXCARS arrangement (Fig. 5.2) to form the measurement volume. The signal beam was transmitted out of the scramjet, recollimated, separated from one of the pump beams, relayed to a 1 m spectrometer, then imaged onto a cooled CCD array with 1340×100 pixels. The measured spectra had background subtracted and were normalized by a CARS spectrum in argon, which has no resonances, to remove the spectrum of the broad-band laser. The resulting spectra were fitted to theory, using the Sandia CARSFIT code[170] to generate the theoretical spectra and an in-house fitting code[171] to do the fitting, resulting in temperature standard deviations of ~3%.[184] The fitted parameters included vibrational temperature of N_2, a single rotational temperature for all resonant species, and mole fractions of N_2, O_2, and H_2.

Vibrational non-equilibrium was observed in the flow at the exit of the nozzle and in the freestream of the scramjet flow, which could be fitted to around 1200 K in vibrational temperature of N_2 and 1000 K in vibrational temperature of O_2, while the facility air

stagnation temperature was 1200 K and the nozzle exit static temperature was around 680 K.[185] The low rate of relaxation of N_2 vibrational energy relative to rotational (which rapidly comes into equilibrium with translational), and the higher but still relatively low rate for O_2 is consistent with known rates in the literature.[186] Measurements in which a varying amount of steam was added to the air flow are consistent with the known effect of water vapor to promote equilibrium.[187] Figure 5.5 shows the effect of water vapor in the dual-pump CARS spectrum; notice the large effect of steam on the hot band of the N_2 spectrum and a lesser effect on the hot band of the O_2. The intensity of these bands is proportional to the population difference between the v=1 and v=2 vibrational states (roughly proportional to the population of v=1 since the population of v=2 is small).

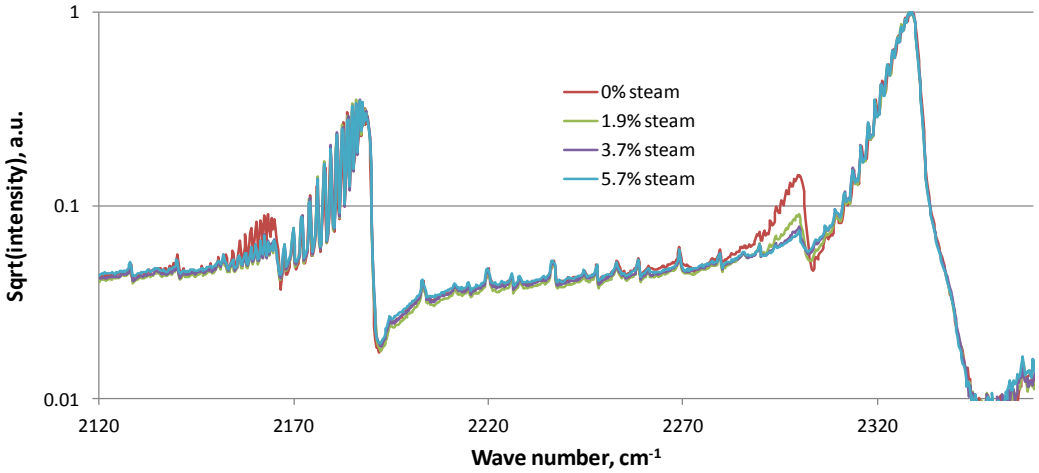

Figure 5.5. Experimental dual-pump CARS spectra in a Mach 2 flow with varying amounts of steam added to the air. The N_2 Q-branch is on the right and the O_2 on the left.

Figure 5.6 shows some typical (averaged) measured spectra and fits to theory in the scramjet. Spectrum (a) was in the freestream air of the flow and is shown with a fitted rotational temperature of 923 K and N_2 vibrational temperature of 1133 K. N_2 and O_2 Q-branch resonances may be seen. Spectrum (b) is in the combustion plume and shows H_2 rotational (S) lines as well as the aforementioned Q-branches, with fitted rotational and vibrational temperatures of 1588 K and 1766 K, respectively. Figure 5.7 shows contour maps of vibrational temperature in the combustor operated in the "scram" mode. The wireframe represents the corners of the flow path; a single hydrogen injector is seen at the downstream end of the small ramp visible on the top surface of the flow path. Flow enters at Mach 2 from the test facility nozzle and is from left to right. The development of the combustion may be seen; combustion is initiated on the top of the plume of hydrogen, near the fuel injector, and wraps around and engulfs the plume further downstream.

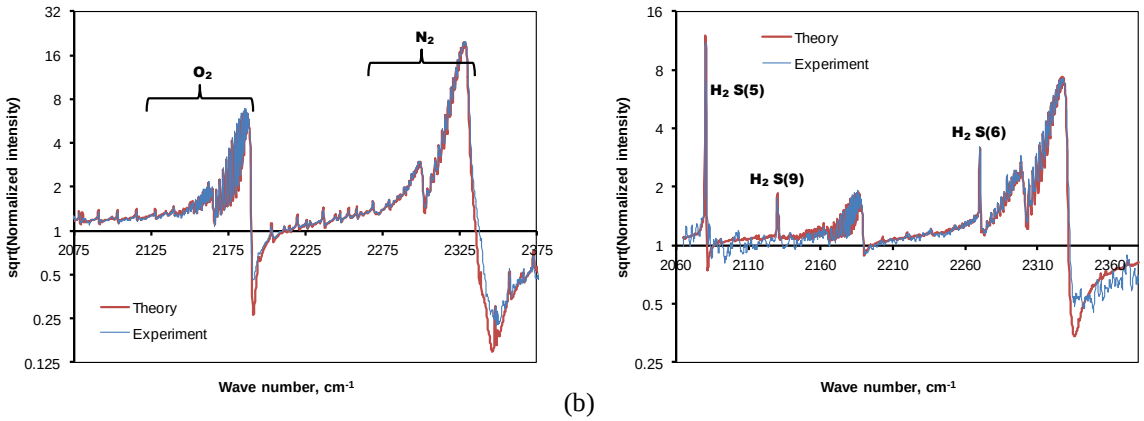

(a) (b)

Figure 5.6. Typical fits of theory to experimental dual-pump CARS spectra in a dual-mode scramjet: (a) freestream, (b) combustion plume.

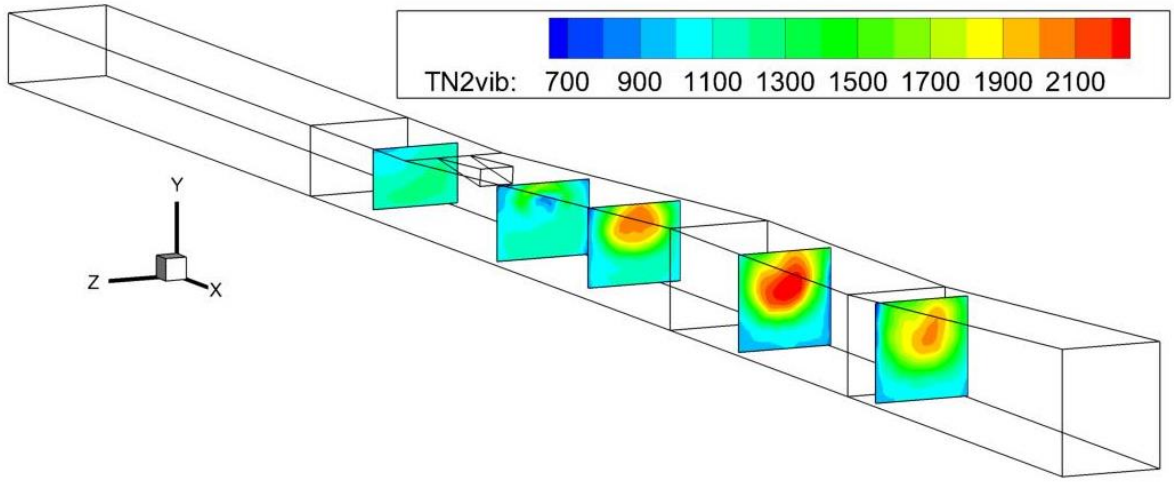

Figure 5.7. Contour plots of CARS-measured mean vibrational temperature in a dual-mode scramjet.

Simultaneous with the temperature measurements, species concentrations were also determined from CARS data. The concentration information was derived from the relative intensity of the different resonant features in the CARS spectra, comparing to the intensity of the nonresonant background, and considering that the mole fractions must sum to one.[169] Figure 5.8 shows CARS mole fraction measurements obtained at the same conditions as Fig. 5.7. The mole fraction is uniform air in the first plane at the left of each of the figures. Evidence of the cold H_2 fuel jet is seen in the temperature map (Fig. 5.6) and all three mole fraction maps in the second plane, which is located just downstream of the fuel injector (Fig. 5.7). As the fuel jet spreads spatially and is consumed by combustion, the presence of N_2 in the center of the downstream fuel plume shows evidence of fuel-air mixing. However, the O_2 mole fraction does not track exactly with the N_2 because it is reacting with the H_2. Not until the final plane at the right side of each figure, when all the H_2 is consumed, does the O_2 penetrate to the center of the duct, in the wake of the fuel plume.

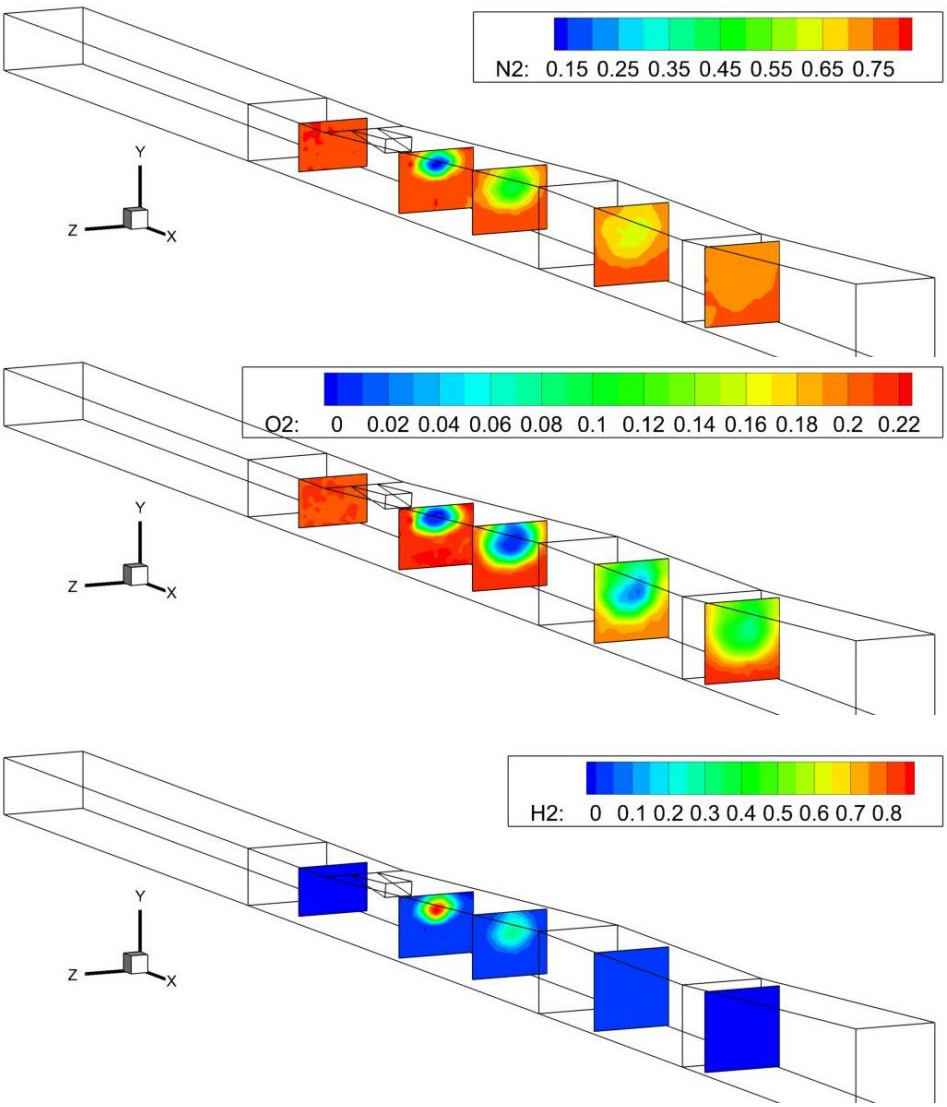

Figure 5.8. Contour plots of CARS-measured mean mole fractions of N_2 (top), O_2 (middle) and H_2 (bottom) in a dual-mode scramjet at the same conditions as Fig. 5.6.[183] Reprinted with permission of the authors.

5.6 Measurement of non-thermalized population distributions using CARS

Nonequilibrium flows sometimes result in non-Boltzmann distributions, for example among rotational or vibrational states. Montello et al.[188] used picosecond CARS to probe non-thermal vibrational distributions in N_2 generated in low pressure (100 Torr) N_2 and air pulsed discharges. They used a 150 ps duration, frequency-doubled Nd:YAG laser to generate the two green pump beams. The Nd:YAG laser also pumped a red broadband dye laser for the Stokes beam. These frequencies were chosen to probe the Q-branch Raman spectrum of N_2. The CARS signal was dispersed on a spectrometer, allowing instantaneous quantification of the N_2 vibrational distribution function (VDF). By varying the time between the CARS acquisition and the pulsing of the plasma discharge, the time evolution of the VDF could be studied.

Figure 5.9(a) shows vibrational N_2 CARS spectra obtained at different times after the beginning of the ~100 ns duration pulsed discharge. The narrowness of the bands indicates a relatively low rotational temperature, compared to the VDF. The populations of the excited vibrational levels are observed to increase with time (though the rotational distribution stays relatively constant). Vibrational levels from 0-9 were observed to have measurable population. When the vibrational populations are graphed with respect to vibrational quantum number (Fig. 5.9(b)) a thermalized population distribution would appear as a nearly straight line on this semi-log plot. Instead, departure from the Boltzmann distribution is observed, as evident from the non-linear trends in the data. A theoretical model captures much of the nonequilibrium physics occurring in this plasma.[188]

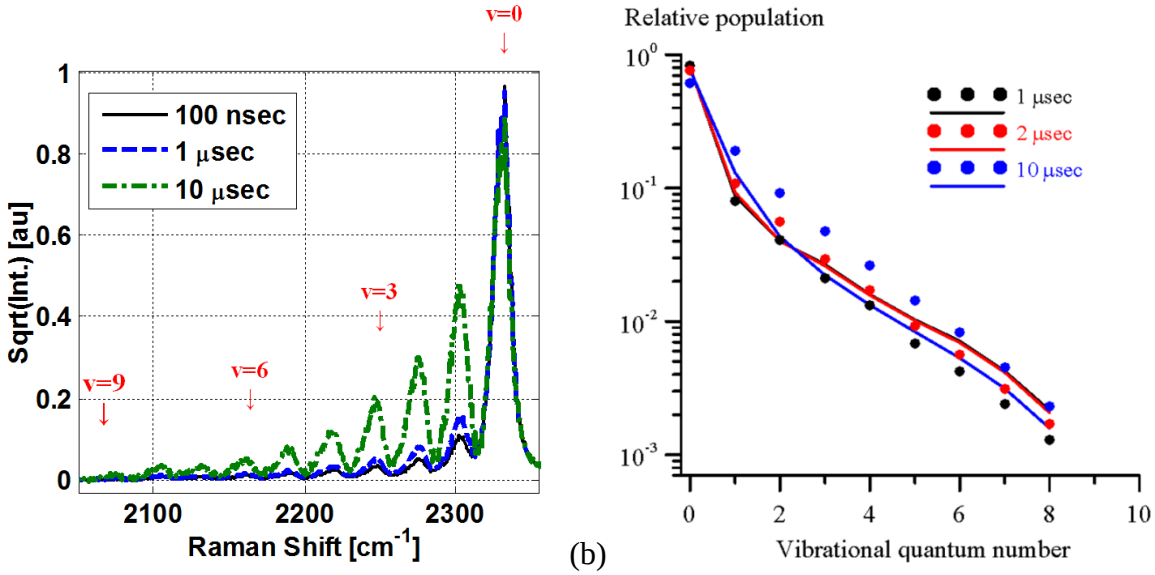

Figure 5.9. (a) N_2 Q-branch CARS spectrum obtained in a pulsed discharge operating with 100 Torr of N_2 shown for three different measurement times after the beginning of the ~100 ns discharge pulse. (b) Experimental and predicted vibrational energy level populations based on (a), showing non-thermal vibrational distributions which evolve with time.

5.7 CARS summary

In summary, CARS is a powerful technique for simultaneously and quantitatively measuring multiple flow parameters in gas flows with thermal and/or chemical non-equilibrium. If the gas is in thermal equilibrium, CARS can be used to measure temperature; if not, it can provide information on rotational and vibrational (for rotational-vibrational CARS) state populations, allowing separate determinations of rotational and vibrational temperature or rotational and vibrational distribution functions in non-thermalized flows. It also can be used to quantify the relative concentration of the species probed. It is spatially and temporally resolved, with a short measurement time (sub-ps to 10 ns) and a measurement volume that is typically on the order of 1 mm long. Nanosecond CARS is limited by available lasers to measurement rates of about 10 Hz, but femtosecond CARS data rates are often 1 kHz or more. Nanosecond CARS is a well-established technique, picosecond and femtosecond CARS in gases is quite recent, due to the advent of suitable lasers, and techniques are still under development. The primary limitations of state-of-the art CARS systems include their complexity (which has meant relatively few applications of it to large-

scale test facilities), the fact that measurements are pointwise and not planar or volumetric, and (for nanosecond CARS) the low data rate. Other issues include sensitivity to optical misalignment due to vibrations or refractive index variations along the beam path, and lack of spectral and collision-rate modeling for some species.

6. Conclusions

This manuscript has described numerous spectroscopic measurement techniques that are potentially applicable to the investigation of aerospace flows. One might ask, *"Which technique is best?"* or *"Which one should I use?"* The answer to the first question is that no one is best. The different techniques measure different properties in different ways and have relative merits. In addition, flow conditions and facility constraints may prevent application of specific measurement techniques. The answer to the second, more important question, depends on many factors. It depends on the measurement requirements as well as the past experience of the research team. It depends on the available equipment, the budget for new equipment and the time frame available to make the measurement. Some techniques, such as CARS, require a year or years of training to gain enough experience to apply the technique expertly. Dual-pump CARS requires home-built equipment (i.e. a broadband dye laser) as well as two commercially available lasers, a spectrometer, a low noise CCD camera, and other equipment. It is therefore relatively time consuming and expensive to set up. If a researcher or research team has experience with similar technology (for example Nd:YAG lasers, dye lasers, CCD cameras), then the work will progress faster. Less complicated (easier to set up and to understand) methods might yield usable results in a shorter time frame. These practical issues are certainly important, but a major consideration in planning an experiment is tailoring the chosen technique to the measurement requirements, the characteristics of the facility and the expertise of the scientist or engineer performing the experiment.

A measurement campaign should begin by answering the following questions, for example by interviewing the final "customer" of the data:

- What parameter(s) need to be measured?
- Must multiple parameters be obtained simultaneously to determine correlations?
- What spatial resolution is required?
- Is imaging required or are single-point or line measurements sufficient?
- What temporal resolution is required? (e.g. time required for a single measurement)
- Do measurements need to be time resolved? (e.g. a continuous sequence of data)
- What accuracy is needed?
- What precision is needed?
- What quantity of data is required?
- When is the data needed? Is instant (real-time) data required?
- Where in the flow are measurements required? (inflow, exit, near walls, etc.)
- What type of optical access is available?

- Can (toxic) seed gases be introduced? Will they influence the properties being measured?
- What is the ordered priority of the above requirements?

This list of requirements must be matched with available measurement technologies such as those reported in the sections above. There is rarely a perfect solution for this exercise. Instead, there is a compromise between the needs of the customer and the capabilities of the instrumentation team and the chosen technique. Goals should then be established before the research actually starts. This exercise is fruitful for the measurement scientist because it often results in a need for a new measurement technique that can be developed if existing techniques are not suitable

Acknowledgements

The authors wish to thank Jennifer Inman and Joel Everhart of NASA Langley Research Center and Christopher Combs from The University of Texas at Austin for assistance in reviewing this manuscript. The authors acknowledge support from the NASA Fundamental Aeronautics Program, Hypersonics and High Speed Projects. Dr. Cutler received support from the National Center for Hypersonic Combined Cycle Propulsion grant FA 9550-09-1-0611. The technical monitors on the grant are Chiping Li (AFOSR), and Aaron Auslender and Rick Gaffney (NASA).

References

[1] A. Smits and T. Lim, *Flow Visualization: Techniques and Examples*, Imperial College Press, London 2000

[2] G. S. Settles, *Schlieren and Shadowgraph Techniques*, Springer-Verlag, Berlin, 2001.

[3] F. White, *Viscous Fluid Flow*, McGraw Hill New York, 1991.

[4] D.C. Wilcox, *Turbulence Modeling for CFD*, DCW Industries, Inc., La Canada, CA,1993.

[5] B.W van Oudheusden, "PIV-based pressure measurement" Meas. Sci. Technol. Vol. 24, pp. 1-32, 2013

[6] C. Tropea, A. L. Yarin, and J. Foss, *Handbook of Experimental Fluid Mechanics*, Volume 1, ISBN-10: 3540251413 Springer, 1st Ed. 2007

[7] D. Sahoo, M. J. Ringuette, and A. J. Smits. "Experimental Investigation of a Hypersonic Turbulent Boundary Layer." AIAA 2009 780 (2009).

[8] G. Tedeschi, H. Gouin and M. Elena. "Motion of Tracer Particles in Supersonic Flows." Experiments in Fluids, Vol. 26, pp. 288-296, 1999.

[9] A. C. Eckbreth, *Laser Diagnostics for Combustion Temperature and Species 2nd Ed*., Combustion Science & Technology Book Series, Volume 3, Taylor & Francis, New York, 1996.

[10] D. G. Fletcher, "Nonintrusive diagnostic strategies for arcjet stream characterization." NASA Ames Research Center, Moffett Field CA .Paper presented at the RTO AVT Course on "Measurement Techniques for High Enthalpy and Plasma Flows", held in Rhode-Saint-Gen~se, Belgium, 25-29 October 1999, and published in RTO EN-8.

[11] Gauglitz, G., and Vo-Dinh, T., *Handbook of Spectroscopy*, Wiley-VCH Verlag GmbH & Co. KGaA, Weinheim, 2003.

[12] Lackner, Maximilian, Gerhard Totschnig, Franz Winter, M. Ortsiefer, M. C. Amann, R. Shau, and J. Rosskopf. "Demonstration of methane spectroscopy using a vertical-cavity surface-emitting laser at 1.68 μm with up to 5 MHz repetition rate." Measurement Science and Technology 14, no. 1 (2003): 101.

[13] Kurtz, J. J., Aizengendler, M., Krishna, Y., Walsh, P., O'Byrne, S. "A rugged, high-sensitivity, TDLAS-based oxygen sensor for a scramjet inlet," ISABE-2013-1605, Proceedings of the 21st International Symposium on Air-Breathing Engines, Busan, Korea, Sept. 9-13, 2013

[14] S. A. Tedder, J. L. Wheeler, A. D. Cutler, and P. M. Danehy, "Width-increased dual-pump enhanced coherent anti-Stokes Raman spectroscopy," Applied Optics Vol. 49, No. 8, pp. 1305–1313, March 2010.

[15] R. G. Seasholtz, and A.E. Buggele. "Improvement in suppression of pulsed Nd: YAG laser light with iodine absorption cells for filtered Rayleigh scattering measurements." NASA Technical Memorandum 113177, November 1997.

[16] N. Chai, S. V. Naik, N. M. Laurendeau, R. P. Lucht, S. Roy, and J. R. Gord. "Single-laser-shot detection of nitric oxide in reacting flows using electronic resonance enhanced coherent anti-Stokes Raman scattering." *Applied Physics Letters* 93, no. 9 (2008): 091115-091115.

[17] M. A. Woodmansee, V. Iyer, J. C. Dutton, and R. P. Lucht. "Nonintrusive pressure and temperature measurements in an underexpanded sonic jet flowfield." AIAA journal 42, no. 6 (2004): 1170-1180.

[18] K. Kohse-Höinghaus, and J. B. Jeffries, eds., *Applied Combustion Diagnostics*, Combustion: An International Series, Taylor & Francis, New York, 2002.

[19] P. C. Palma, *Laser-Induced Fluorescence Imaging in Free-Piston Shock Tunnels*, PhD Thesis, Australian National University, submitted May 1998, revised February 1999.

[20] B. A. E. Saleh, and M. C. Teich, *Fundamentals of Photonics 2nd Ed.*, John Wiley & Sons, Inc., Hoboken, New Jersey, 2007.

[21] W. K. Bischel, P. J. Kelly, and C. K. Rhodes, "*High-resolution Doppler-free two-photon spectroscopic studies of molecules. I. The v_3 bands of $^{12}CH_3F$*," Physical Review A, 13(5), 1976.

[22] T. J. McIlrath, R. Hudson, A. Aikin, and T. D. Wilkerson, "*Two-photon lidar technique for remote sensing of atomic oxygen*," Applied Optics, 18(3), 1979.

[23] W. K. Bischel, B. E. Perry, and D. R. Crosley, "*Detection of fluorescence from O and N atoms induced by two-photon absorption*," Applied Optics, 21(8), 1982.

[24] U. Meier, J. Bittner, K. Kohse-Höinghaus, and Th. Just, "*Discussion of two-photon laser-excited fluorescence as a method for quantitative detection of oxygen atoms in flames*," 22nd Symposium (International) on Combustion, The Combustion Institute, 1988.

[25] D. R. Crosley, "*Rotational and Translational Effects in Collisions of Electronically Excited Diatomic Hydrides*," Journal of Physical Chemistry, 1989, 93, 6273 – 6282.

[26] J. D. Anderson Jr., *Hypersonic and High-Temperature Gas Dynamics 2nd ed.*, AIAA Education Series, AIAA, Reston, VA, 2006.

[27] W. G. Vincenti, and C. H. Kruger Jr., *Introduction to Physical Gas Dynamics*, Reprint of 1967 ed., Wiley, New York, 1975.

[28] P. H. Paul, J. A. Gray, J. L. Durant, J. W. Thoman, "*Collisional Quenching Corrections for Laser-Induced Fluorescence Measurements of NO $A^2\Sigma^+$*," AIAA Journal, 32(8), August 1994.

[29] D. S. Baer, H. A. Chang, and R. K. Hanson, "*Fluorescence diagnostics for atmospheric-pressure plasmas using semiconductor lasers*," Journal of the Optical Society of America B, 9(11), pp. 1968-1978, November, 1992.

[30] J. G. Liebeskind, R. K. Hanson, and M. A. Cappelli, "*Laser-induced fluorescence diagnostic for temperature and velocity measurements in a hydrogen arcjet plume*," Applied Optics, 32(30), pp. 6117-6127, October 20, 1993.

[31] J. A. Inman, B. F. Bathel, C. T. Johansen, P. M. Danehy, S. B. Jones, J. G. Gragg, and S. C. Splinter, "*Nitric Oxide PLIF Measurements in the Hypersonic Materials Environmental Test System (HYMETS)*," 49th AIAA Aerospace Sciences Meeting, AIAA Paper 2011-1090, Orlando, FL, January 4-7, 2011.

[32] P. V. Storm, and M. A. Cappelli, "*LIF Characterization of Arcjet Nozzle Flows*," AIAA, ASME, SAE, and ASEE, Joint Propulsion Conference, AIAA Paper 1996-2987, Lake Buena Vista, FL, July 1 – 3, 1996.

[33] D. G. Fletcher, "*Arcjet flow properties determined from laser-induced fluorescence of atomic nitrogen*," 36th AIAA Aerospace Sciences Meeting, AIAA Paper 1998-0205.

[34] D. G. Fletcher, "*Arcjet flow properties determined from laser-induced fluorescence of atomic nitrogen*," Applied Optics, 38(9), March 20, 1999.
[35] J. H. Grinstead, B. J. Porter, and J. E. Carballo, "*Flow Property Measurement Using Laser-Induced Fluorescence in the NASA Ames Interaction Heating Facility*," 49th AIAA Aerospace Sciences Meeting, AIAA Paper 2011-1091, Orlando, FL., January 4 – 7, 2011.
[36] A. Lutz, J. Meyers, W. Owens, S. Smith, and D. G. Fletcher, "*Experimental Analysis of Carbon Nitridation and Oxidation Efficiency with Laser-Induced Fluorescence*," 51st AIAA Aerospace Sciences Meeting, AIAA Paper 2013-0924, Grapevine, TX., January 7 – 10, 2013.
[37] R. L. McKenzie, and K. P. Gross, "*Two-photon excitation of nitric oxide fluorescence as a temperature indicator in unsteady gasdynamic processes*," Applied Optics, 20(12), June 15, 1981.
[38] B. K. McMillin, J. L. Palmer, and R. K. Hanson, "*Temporally resolved, two-line fluorescence imaging of NO temperature in a transverse jet in a supersonic cross flow*," Applied Optics, 32(36), December, 20, 1993.
[39] J. M. Seitzman, R. K. Hanson, P. A. DeBarber, and C. F. Hess, "*Application of quantitative two-line OH planar laser-induced fluorescence for temporally resolved planar thermometry in reacting flows*," Applied Optics, 33(18), June 20, 1994.
[40] B. K. McMillin, J. M. Seitzman, and R. K. Hanson, "*Comparison of NO and OH Planar Fluorescence Temperature Measurements in Scramjet Model Flowfields*," AIAA Journal, 32(10), October 1994.
[41] P. C. Palma, P. M. Danehy, and A. F. P. Houwing, "*Fluorescence Imaging of Rotational and Vibrational Temperature in Shock-Tunnel Nozzle Flow*," AIAA Journal, 41(9), September 2003.
[42] E. R. Lachney, and N. T. Clemens, "*PLIF imaging of mean temperature and pressure in a supersonic bluff wake*," Experiments in Fluids, 24, pp. 354-363, 1998.
[43] U. Koch, A. Gülhan, and B. Esser, "*Determination of NO-rotational and vibrational temperature profiles in a high enthalpy flow field with nonequilibrium*," 1st Joint French-German Symposium on Simulation of Atmospheric Entries by Means of Ground Test Facilities, Stuttgart, Germany, 1999.
[44] A. Del Vecchio, G. Palumbo, U. Koch, and A. Gülhan, "*Temperature Measurements by Laser-induced Fluorescence Spectroscopy in Nonequilibrium High-Enthalpy Flow*," Journal of Spacecraft and Rockets, 14(2), April-June 2000.
[45] S. Löhle, M. Auweter-Kurtz, G. Herdrich, and T. Laux, "*LIF Measurements of NO in N_2/O_2 and N_2/CO_2 Plasma Flows*," 36th AIAA Thermophysics Conference, AIAA Paper 2003-3487, Orlando, FL., June 23-26, 2003.
[46] E. A. Brinkman, G. A. Raiche, M. S. Brown, and J. B. Jeffries, "*Optical diagnostics for temperature measurement in a DC arcjet reactor used for diamond deposition*," Applied Physics B, 64(6), pp. 689-697, 1997.
[47] W. G. Bessler, and C. Schulz, "*Quantitative multi-line NO-LIF temperature imaging*," Applied Physics B, 78, pp. 519-533, 2004.
[48] J. L. Palmer, and R. K. Hanson, "*Planar laser-induced fluorescence temperature measurements in free jet flows with vibrational nonequilibrium*," 31st AIAA Aerospace Sciences Meeting, AIAA Paper 1993-0046, Reno, NV., January 11-14, 1993.
[49] J.A. Inman, B.F. Bathel, C.T. Johansen, P.M. Danehy, S.B. Jones, J.G. Gragg, and S.C. Splinter, "*Nitric-Oxide Planar Laser-Induced Fluorescence Measurements in the Hypersonic Materials Environmental Test System*," Accepted by AIAA Journal, To Appear in 2013.
[50] A.J. Smits and T.T. Lin, eds., *Flow Visualization: Techniques and Examples 2nd Ed.*, Imperial College Press, London, 2012.
[51] H. Katô, and M. Baba, "*Dynamics of Excited Molecules: Predissociation*," Chemical Review, 95, pp. 2311-2349, 1995.
[52] G. Herzberg, "*Molecular Spectra and Molecular Structure: I. Spectra of Diatomic Molecules"*, New York, Van Nostrand Reinhold, 1950.
[53] G. Laufer, T. M. Quagliaroli, R. H. Krauss, R. B. Whitehurst III, J. C. McDaniel, and J. H. Grinstead, "*Planar OH Density and Apparent Temperature Measurements in a Supersonic Combusting Flow*," AIAA Journal, 34(3), March 1996.

[54] J. Zhang, G. B. King, N. M. Laurendeau, and M. W. Renfro, "*Two-point time-series measurements of hydroxyl concentration in a turbulent nonpremixed flame*," Applied Optics, 46(23), August 10, 2007.

[55] T. B. Settersten, B. D. Patterson, and W. H. Humphries, "*Radiative lifetimes of NO $A^2\Sigma^+(v'=0,1,2)$ and the electronic transition moment of the $A^2\Sigma^+$-$X^2\Pi$ system*," Journal of Chemical Physics, 131, 2009.

[56] T. B. Settersten, B. D. Patterson, and J. A. Gray, "*Temperature- and species-dependent quenching of NO $A^2\Sigma^+(v'=0)$ probed by two-photon laser-induced fluorescence using a picosecond laser*," Journal of Chemical Physics, 124, 2006.

[57] T. B. Settersten, B. D. Patterson, and C. D. Carter, "*Collisional quenching of NO $A^2\Sigma^+(v'=0)$ between 125 and 294 K*," Journal of Chemical Physics, 130, 2009.

[58] J. H. Grinstead, D. M. Driver, and G. A. Raiche, "*Radial profiles of arcjet flow properties measured with laser-induced fluorescence of atomic nitrogen*," 41st AIAA Aerospace Sciences Meeting, AIAA 2003-400, Reno, NV., January 6-9, 2003.

[59] D. G. Fletcher, and M. Playez, "*Characterization of supersonic and subsonic plasma flows*," 25th AIAA Aerodynamic Measurement Technology and Ground Testing Conference, AIAA 2006-3294, San Francisco, CA., June 5-8, 2006.

[60] B. J. Lochman, Z. R. Murphree, V. Narayanaswamy, and N. T. Clemens, "*PLIF imaging of naphthalene-ablation products in a Mach 5 turbulent boundary layer*," 27th AIAA Aerodynamic Measurement Technology and Ground Testing Conference, AIAA 2010-4346, Chicago, IL., June 28 – July 1, 2010.

[61] O. R. H. Buxton, B. J. Lochman, M. Sharma, and N. T. Clemens, "*Simultaneous PIV and PLIF Imaging of Low-Temperature Ablation in a Mach 5 Turbulent Boundary Layer*," 50th AIAA Aerospace Sciences Meeting, AIAA 2012-440, Nashville, TN., January 9-12, 2012.

[62] Thorne, A., Litzén, U., and Johansson, S., *Spectrophysics: Principles and Applications*, Berlin Heidelberg, 1999.

[63] M. Versluis, Georgiev, L. Martinsson, M. Aldén, and S. Kröll, "*2-D absolute OH concentration profiles in atmospheric flames using planar LIF in a bi-directional laser beam configuration*," Applied Physics B, 65, pp. 411-417, 1997.

[64] C. D. Carter, and R. S. Barlow, "*Simultaneous measurements of NO, OH, and the major species in turbulent flames*," Optics Letters, 19(4), pp. 299-301, February 15, 1994.

[65] R. S. Barlow, G.-H. Wang, P. Anselmo-Filho, M. S. Sweeney, and S. Hochgreb, "*Application of Raman/Rayleigh/LIF diagnostics in turbulent stratified flames*," Proceedings of the Combustion Institute, 32, pp. 945-953, 2009.

[66] J. C. McDaniel, "*Nonintrusive Pressure Measurement with Laser-Induced Iodine Fluorescence*," 18th AIAA Thermophysics Conference, AIAA 1983-1468, Montreal, Canada, June 1-3, 1983.

[67] F. Lemoine and B. Leporcq, "*An efficient optical pressure measurement in compressible flows: Laser-induced iodine fluorescence*," Experiments in Fluids, 19, pp. 150-158, 1995.

[68] A. Y. Chang, B. E. Battles, and R. K. Hanson, "*Simultaneous measurements of velocity, temperature, and pressure using rapid cw wavelength-modulation laser-induced fluorescence of OH*," Optics Letters, 15(12), June 15, 1990.

[69] S. V. Naik, W. D. Kulatilaka, K. K. Venkatesan, and R. P. Lucht, "*Pressure, Temperature, and Velocity Measurements in Underexpanded Jets Using Laser-Induced Fluorescence Imaging*," AIAA Journal, 47(4), April 2009.

[70] B. Hiller, and R. K. Hanson, "*Simultaneous planar measurements of velocity and pressure fields in gas flows using laser-induced fluorescence*," Applied Optics, 27(1), January 1, 1988.

[71] J. Hartfield Jr., S. D. Hollo, and J. C. McDaniel, "*A unified planar measurement technique for compressible flows using laser-induced iodine fluorescence*," 30th AIAA Aerospace Sciences Meeting, AIAA 1992-0141, Reno, NV, January 6-9, 1992.

[72] D. A. Rothamer and R. K. Hanson, "*Temperature and pressure imaging using infrared planar laser-induced fluorescence*," Applied Optics, 49(33), pp. 6436-6447, November 20, 2010.

[73] W. J. Marinelli, W. J. Kessler, M. G. Allen, S. J. Davis, S. Arepalli, and C. D. Scott, "*Copper atom based measurements of velocity and turbulence in arc jet flows*," 29th Aerospace Sciences Meeting, AIAA 1991-358, Reno, NV., January 7-10, 1991.

[74] J. C. McDaniel, B. Hiller, and R. K. Hanson, "*Simultaneous multiple-point velocity measurements using laser-induced iodine fluorescence*," Optics Letters, 8(1), pp. 51-53, January 1983.

[75] K. G. Klavuhn, G. Gauba, and J. C. McDaniel, "*OH Laser-Induced Fluorescence Velocimetry Technique for Steady, High-Speed, Reacting Flows*," Journal of Propulsion and Power, 10(6), 1994.

[76] W. D. Kulatilaka, S. V. Naik, and R. P. Lucht, "*Development of High-Spectral-Resolution Planar Laser-Induced Fluorescence Imaging Diagnostics for High-Speed Gas Flows*," AIAA Journal, 46(1), January 2008.

[77] P. M. Danehy, P. Mere, M. J. Gaston, S. O'Bryne, P. C. Palma, A. F. P. and Houwing, "*Fluorescence velocimetry of the hypersonic, separated flow over a cone*," AIAA Journal, 39(7), pp. 1320-1328, 2001.

[78] R. Hruschka, S. O'Byrne, and H. Kleine, "*Two-component Doppler-shift fluorescence velocimetry applied to a generic planetary entry probe model*," Experiments in Fluids, 48, pp. 1109-1120, 2010.

[79] D. G. Fletcher, and J. C. McDaniel, "*Laser-Induced Iodine Fluorescence Technique for Quantitative Measurement in a Nonreacting Supersonic Combustor*," AIAA Journal, 27(5), May 1989.

[80] R. J. Hartfield, S. D. Hollo, and J. C. McDaniel, "*Planar Measurement Technique for Compressible Flows Using Laser-Induced Iodine Fluorescence*," AIAA Journal, 31(3), March 1993.

[81] J. M. Donohue, and J. C. McDaniel, "*Computer-Controlled Multiparameter Flowfield Measurements Using Planar Laser-Induced Iodine Fluorescence*," AIAA Journal, 34(8), August 1996.

[82] M. Zimmerman, and R. B. Miles, "*Hypersonic-helium-flow-field measurements with the resonant Doppler velocimeter*," Applied Physics Letters, 37(10), November 15, 1980.

[83] B. F. Bathel, C. Johansen, J. A. Inman, S. B. Jones, and P. M. Danehy, "*Review of Fluorescence-Based Velocimetry Techniques to Study High-Speed Compressible Flows*,"AIAA 2013-0339, 51st AIAA Aerospace Sciences Meeting, Grapevine, TX, January 7-10, 2013.

[84] B. Hiller, and R. K. Hanson, "*Two-frequency laser-induced fluorescence technique for rapid velocity-field measurements in gas flows*," Optics Letters, 10(5), May, 1985.

[85] U. Westblom, and M. Aldėn, "*Spatially resolved flow velocity measurements using laser-induced fluorescence from a pulsed laser*," Optics Letters, 14(1), January 1, 1989.

[86] P. H. Paul, M. P. Lee, and R. K. Hanson, "*Molecular velocity imaging of supersonic flows using pulsed planar laser-induced fluorescence of NO*," Optics Letters, 14(9), May 1, 1989.

[87] M. Allen, S. Davis, W. Kessler, H. Legner, K. McManus, P. Mulhall, T. Parker, and D. Sonnenfroh, "*Velocity Field Imaging in Supersonic Reacting Flows near Atmospheric Pressure*," AIAA Journal, 32(8), August 1994.

[88] M. M. Koochesfahani, and D. G. Nocera, *"Molecular Tagging Velocimetry*," *Handbook of Experimental Fluid Dynamics*, Chap. 5.4, edited by J. Foss, C. Tropea, and A. Yarin, Springer-Verlag, Berlin, 2007.

[89] B. Hiller, R. A. Booman, C. Hassa, and R. K. Hanson, "*Velocity Visualization in Gas Flows Using Laser-Induced Phosphorescence of Biacetyle*," Review of Scientific Instruments, 55(12), pp. 1964-1967, December, 1984.

[90] P. M. Danehy, S. O'Byrne, A. F. P. Houwing, J. S. Fox, and D. R. Smith, "*Flow-Tagging Velocimetry for Hypersonic Flows Using Fluorescence of Nitric Oxide*," AIAA Journal, 41(2), February 2003.

[91] B. F. Bathel, P. M. Danehy, J. A. Inman, S. B. Jones, C. B. Ivey, C. P, and Goyne, "*Velocity Profile Measurements in Hypersonic Flows Using Sequentially Imaged Fluorescence-Based Molecular Tagging*," AIAA Journal, 49(9), September 2011.

[92] W. R. Lempert, N. Jiang, S. Sethuram, and M. Samimy, "*Molecular Tagging Velocimetry Measurements in Supersonic Microjets*," AIAA Journal, 40(6), June, 2002.

[93] W. R. Lempert, M. Boehm, N. Jiang, S. Gimelshein, and D. Levin, "*Comparison of molecular tagging velocimetry data and direct simulation Monte Carlo simulations in supersonic micro jet flows*," Experiments in Fluids, 34, pp. 403-411, 2003.

[94] A. G. Hsu, R. Srinivasan, R. D. W. Bowersox, and S. W. North, "*Two-component molecular tagging velocimetry utilizing NO fluorescence lifetime and NO_2 photodissociation techniques in an underexpanded jet flowfield*," Applied Optics, 48(22), August 1, 2009.

[95] J. A. Inman, P. M. Danehy, B. F. Bathel, D. W. Alderfer, and R. J. Nowak, "*Laser-Induced Fluorescence Velocity Measurements in Supersonic Underexpanded Impinging Jets*," 48th AIAA Aerospace Sciences Meeting, AIAA 2010-1438, Orlando, FL., January 4-7, 2010.

[96] C. T. Johansen, P. M. Danehy, S. W. Ashcraft, B. F. Bathel, J. A. Inman, and S. B. Jones, "*PLIF study of Mars Science Laboratory capsule reaction control system jets*," 41st AIAA Fluid Dynamics Conference, AIAA Paper 2011-3890, Honolulu, HI., June 27-30, 2011.

[97] C. T. Johansen, J. Novak, B. Bathel, S. W. Ashcraft, and P. M. Danehy, "*Comparison of MSL RCS jet computations with flow visualization and velocimetry*," 50th AIAA Aerospace Sciences Meeting, AIAA Paper 2012-0594, Nashville, TN., January 4-7, 2012.

[98] R. J. Balla, "Iodine Tagging Velocimetry in a Mach 10 Wake", AIAA Journal, Technical Note, (accepted).

[99] A. F. P. Houwing, D. R. Smith, J. S. Fox, P. M. Danehy, and N. R. Mudford, "*Laminar boundary layer separation at a fin-body junction in a hypersonic flow*," Shock Waves, 11, pp. 31-42, 2001.

[100] B. F. Bathel, P. M. Danehy, J. A. Inman, A. N. Watkins, S. B. Jones, W. E. Lipford, K. Z. Goodman, C. B. Ivey, and C. P. Goyne, "*Hypersonic Laminar Boundary Layer Velocimetry with Discrete Roughness on a Flat Plate*," AIAA Paper 2010-4998, 40th Fluid Dynamics Conference and Exhibit, Chicago, IL, June 28 - July 1, 2010.

[101] J. B. Michael, M. R. Edwards, A. Dogariu, and R. B. Miles, "*Femtosecond laser electronic excitation tagging for quantitative velocity imaging in air*," Applied Optics, 50(26), pp. 5158-5162, September 10, 2011.

[102] J. B. Michael, M. R. Edwards, A. Dogariu, and R. B. Miles, "*Velocimetry by femtosecond laser electronic excitation tagging (FLEET) of air and nitrogen*," 50th AIAA Aerospace Sciences Meeting, AIAA 2012-1053, Nashville, TN., January 9-12, 2012.

[103] M. R. Edwards, A. Dogariu, and R. B. Miles, "*Simultaneous Temperature and Velocity Measurement in Unseeded Air Flows with FLEET*," 51st AIAA Aerospace Sciences Meeting, AIAA 2013-0043, Grapevine, TX., January 7-10, 2013.

[104] P. Barker, A. Bishop, and H. Rubinsztein-Dunlop, "*Supersonic velocimetry in a shock tube using laser enhanced ionization and planar laser induced fluorescence*," Appl. Phys. B, 64 (3), pp. 369-376, 1997.

[105] P. F. Barker, A. M. Thomas, T. J. McIntyre, and H. Dunlop-Rubinsztein, "*Velocimetry and Thermometry of Supersonic Flow Around a Cylindrical Body*," AIAA Journal, 36 (6), pp. 1055-1060, June 1998.

[106] B. N. Littleton, A. I. Bishop, T. J. McIntyre, P. F. Barker, and H. Dunlop-Rubinsztein, "*Flow tagging velocimetry in a superorbital expansion tube*," Shock Waves, 10, pp. 225-228, 2000.

[107] R. Miles, C. Cohen, J. Connors, P. Howard, S. Huang, E. Markovitz, and G. Russell, "*Velocity measurements by vibrational tagging and fluorescent probing of oxygen*," Optics Letters, 12 (11), pp. 861-863, November, 1987.

[108] R. B. Miles, D. Zhou, B. Zhang, W. R. Lempert, and Z-S. She, "*Fundamental Turbulence Measurements by Relief Flow Tagging*," AIAA Journal, 31(3), March, 1993.

[109] R. B. Miles, J. Conners, E. Markovitz, P. Howard, and G. Roth, "*Instantaneous supersonic velocity profiles in an underexpanded sonic air jet by oxygen flow tagging*," Physics of Fluids A, 1(2), pp. 389-393, February, 1989.

[110] R. B. Miles, J. Grinstead, R. H. Kohl, and G. Diskin, "*The RELIEF flow tagging technique and its application in engine testing facilities and for helium-air mixing studies*," Measurement Science and Technology, 11(9), pp. 1272-1281, September, 2000.

[111] L. R. Boedeker, "*Velocity measurement by H_2O photolysis and laser-induced fluorescence of OH*," Optics Letters, 14 (10), pp. 473-475, May 15, 1989.

[112] J. A. Wehrmeyer, L. A. Ribarov, D. A. Oguss, F. Batliwala, R. W. Pitz, and P. A. DeBarber, "*Flow tagging velocimetry for low and high temperature flowfields*," *37th AIAA Aerospace Sciences Meeting*, Reno, NV, 1999.

[113] J. A. Wehrmeyer, L. A. Ribarov, D. A. Oguss, R. W. and Pitz, "*Flame flow tagging velocimetry with 193-nm H_2O photodissociation*," Applied Optics, 38 (33), pp. 6912-6917, November, 20, 1999.

[114] L. A. Ribarov, J. A. Wehrmeyer, S. Hu, and R. W. Pitz, "*Multiline hydroxyl tagging velocimetry measurements in reacting and nonreacting experimental flows*," Experiments in Fluids, 37, pp. 65-74, 2004.

[115] L. A. Ribarov, S. Hu, J. A. Wehrmeyer, R. W. and Pitz, "*Hydroxyl tagging velocimetry method optimization: signal intensity and spectroscopy*," Applied Optics, 44 (31), pp. 6616-6626, November, 1, 2005.

[116] R. W. Pitz, M. D. Lahr, Z. W. Douglas, J. A. Wehrmeyer, S. Hu, C. D. Carter, K-Y. Hsu, C. Lum, and M. M. Koochesfahani, "*Hydroxyl tagging velocimetry in a supersonic flow over a cavity*," Applied Optics, 44(31), pp. 6692-6700, November 1, 2005.

[117] M. D. Lahr, R. W. Pitz, Z. W. Douglas, and C. D. Carter, "*Hydroxyl-Tagging-Velocimetry Measurements of a Supersonic Flow over a Cavity*," Journal of Propulsion and Power, 26 (4), pp. 790-797, July – August 2010.

[118] A. M. ElBaz, and R. W. Pitz, "*N_2O molecular tagging velocimetry*," Applied Physics B, 106, pp. 961-969, 2012.

[119] R. W. Pitz, T. M. Brown, S. P. Nandula, P. A. Skaggs, P. A. DeBarber, M. S. Brown, and J. Segall, "*Unseeded velocity measurement by ozone tagging velocimetry*," Optics Letters, 21 (10), pp. 755-757, 1996.

[120] L. A. Ribarov, J. A. Wehrmeyer, F. Batliwala, R. W. Pitz, and P. A. DeBarber, "*Ozone Tagging Velocimetry Using Narrowband Excimer Lasers*," AIAA Journal, 37(6), June 1999.

[121] N. J. Dam, R. J. H. Klein-Douwel, N. M. Sijtsema, and J. J. ter Meulen, "*Nitric oxide flow tagging in unseeded air*," Optics Letters, 26 (1), pp. 36-38, January 1, 2001.

[122] N. M. Sijtsema, N. J. Dam, R. J. H. Klein-Douwel, and J. J. ter Meulen, "*Air Photolysis and Recombination Tracking: A New Molecular Tagging Velocimetry Scheme*," AIAA Journal, 40 (6), pp. 1061-1064, June 2002.

[123] W. P. N. Van der Lann, R. A. L. Tolboom, N. J. Dam, and J. J. ter Meulen, "*Molecular tagging velocimetry in the wake of an object in supersonic flow*," Experiments in Fluids, 34, pp. 531-534, 2003.

[124] J. Bominaar, M. Pashtrapanska, T. Elenbaas, N. Dam, H. ter Meulen, W. van de Water, "*Writing in turbulent air*," Physical Review E, 77, 2008.

[125] C. Orlemann, C. Schulz, and J. Wolfrum, "*NO-flow tagging by photodissociation of NO_2. A new approach for measuring small-scale flow structures*," Chem. Phys. Lett., 307, pp. 15-20, 1999.

[126] N. Shinji, M. Kasahara, M. Tsue, and M. Kono, "*Velocity Measurements of Reactive and Non-reactive Flows by NO-LIF Method Using NO_2 Photodissociation*," Heat Transfer – Asian Research, 34 (1), pp. 40-52, 2005.

[127] A. G. Hsu, R. Srinivasan, R. D. W. Bowersox, and S. W. North, "*Molecular Tagging Using Vibrationally Excited Nitric Oxide in an Underexpanded Jet Flowfield*," AIAA Journal, 47 (11), pp. 2597-2604, November, 2009.

[128] N. Jiang, M. Nishihara, and W. R. Lempert, "*500 kHz NO_2 Molecular Tagging Velocimetry in a Mach 5 Wind Tunnel*," 27th AIAA Aerodynamic Measurement Technology and Ground Testing Conference, AIAA 2010-4348, Chicago, IL., Jun 28-July 1, 2010.

[129] R. Sánchez-González, R. Srinivasan, R. D. W. Bowersox, and S. W. North, "*Simultaneous velocity and temperature measurements in gaseous flow fields using the VENOM technique*," Optics Letters, 36(2), pp. 196-198, January 15, 2011.

[130] R. Sánchez-González, R. Srinivasan, R. D. W. Bowersox, and S. W. North, "*Simultaneous velocity and temperature measurements in gaseous flowfields using the vibrationally excited nitric oxide monitoring technique: a comprehensive study*," Applied Optics, 51(9), pp. 1216-1228, March 20, 2012.

[131] B. F. Bathel, P. M. Danehy, C. T. Johansen, S. B. Jones, and C. P. Goyne, "*Hypersonic Boundary Layer Measurements with Variable Blowing Rates Using Molecular Tagging Velocimetry*," AIAA Paper 2012-2886, 28th AIAA Aerodynamic Measurement Technology, Ground Testing, and Flight Testing Conference, New Orleans, LA., June 25-28, 2012.

[132] B. F. Bathel, C. T. Johansen, S. B. Jones, P. M. Danehy, and C. P. Goyne, "*Trip-induced Transition Measurements in a Hypersonic Boundary Layer Using Molecular Tagging Velocimetry*," 51st AIAA Aerospace Sciences Meeting, AIAA 2013-0042, Grapevine, TX., January 7-10, 2013.

[133] I. Boxx, M. Stöhr, C. Carter, and W. Meier, "*Sustained multi-kHz flamefront and 3-component velocity-field measurements for the study of turbulent flames*, Applied Physics B, 95(1), pp. 23-29, April, 2009.

[134] N. Jiang, M. Webster, W. R. Lempert, J. D. Miller, T. R. Meyer, C. B. Ivey, and P. M. Danehy, "*MHz-rate nitric oxide planar laser-induced fluorescence imaging in a Mach 10 hypersonic wind tunnel*," Applied Optics, 50(4), February 1, 2011.

[135] N. Jiang, J. Bruzzese, R. Patton, J. Sutton, R. Yentsch, D. V. Gaitonde, W. R. Lempert, K. D. Miller, T. R. Meyer, R. Parker, T. Wadham, M. Holden, and P. M. Danehy, "*NO PLIF imaging in the CUBRC 48-inch shock tunnel*," Experiments in Fluids, 53, pp. 1637-1646, 2012.

[136] B. Yip, R. L. Schmitt, and M. B. Long, "*Instantaneous three-dimensional concentration measurements in turbulent jets and flames*," Optics Letters, 13(2), pp. 96-98, February, 1988.

[137] P. M. Danehy, B. F. Bathel, J. A. Inman, D. W. Alderfer, and S. B. Jones, "*Stereoscopic Imaging in Hypersonic Boundary Layers using Planar Laser-Induced Fluorescence*," 26th AIAA Aerodynamic Measurement Technology and Ground Testing Conference, AIAA 2008-4267, Seattle, WA., June 23-26, 2008.

[138] C. S. Combs, N. T. Clemens, P. M. Danehy, B. F. Bathel, R. Parker, T. Wadhams, M. Holden, and B. Kirk, "*NO PLIF Visualizations of the Orion Capsule in LENS-I*," 51st AIAA Aerospace Sciences Meeting, AIAA 2013-0033, Grapevine, TX., January 7-10, 2013.

[139] R. B. Miles, W. R. Lempert and J. N. Forkey, "Laser Rayleigh Scattering," Meas. Sci. Technol. p. R33-R51, v.12, 2001.

[140] Springer Handbook of Experimental Fluid Mechanics, Volume 1, edited by Cameron Tropea, Alexander L. Yarin, John F. Foss, ISBN-10: 3540251413 Springer, 1st Ed. 2007.

[141] G. C. Baldwin, "An Introduction Nonlinear Optics," Plenum Press, New York, 1969.

[142] A. Thorne, U. Litzėn, and S. Johansson, Spectrophysics: Principles and Applications, Berlin Heidelberg, 1999.

[143] P. Magre and R. W. Dibble, Finite chemical kinetic effects in a subsonic turbulent hydrogen flame, Combust. Flame 73, 195, 1988.

[144] V. Bergmann, W. Meier, D. Wolff, and W. Stricker, "Application of Spontaneous Raman and Rayleigh Scattering and 2D LIF for the characterization of a Turblent $CH_4/H_2/N_2$ Jet Diffusion Flame," appl. Phys. B, vol. 66, pp. 489-502, 1998.

[145] Q.V. Nguyen, R.W. Dibble, C.D. Carter, G.J. Fiechtner and R.S. Barlow, "Raman-LIF Measurement of Temperature, Major Species, OH and NO in a Methane-Air Bunsen Flame," Combust. Flame, vol. 105, pp. 499-510, 1996.

[146] R. G. Seasholtz and A. E. Buggele, "Improvement in Suppression of Pulsed Nd:YAG Laser Light With Iodine Absorption Cells for Filtered Rayleigh Scattering Measurements," NASA TM–113177.

[147] G. S. Elliott, M. Samimy, S. A. Arnette, "Details of a Molecular Filter-Based Velocimetry Technique," Paper AIAA-94-0490, 32nd Aerospace Sciences Meeting & Exhibit, Reno, NV, January 10-13, 1994.

[148] G. S. Elliott, M. Samimy, S. A. Arnette "A molecular filter based velocimetry technique for high speed flows," Experiments in Fluids, Volume 18, Issue 1-2, pp 107-118, December 1994.

[149] R.G. Seasholtz, A.E. Buggele, and M.F. Reeder, "Flow Measurements Based on Rayleigh Scattering and Fabry-Perot Interferometer," Optics and Lasers in Engineering, Vol. 27, No. 6, 1997, pp. 543-570.

[150] D. Bivolaru, M. V. Otugen, A. Tzes, and G. Papadopoulos, "Image Processing for Interferometric Mie and Rayleigh Scattering Velocity Measurements," AIAA J.Vol. 37, No. 6, June 1999.

[151] D. Bivolaru, P. M. Danehy, R. L. Gaffney, Jr. and A. D. Cutler, "Direct-View Multi-Point Two-Component Interferometric Rayleigh Scattering Velocimeter," 46th AIAA Aerospace Sciences Meeting and Exhibit, Reno, Nevada, AIAA Paper 2008-236, January 7-10, 2008.

[152] A. F. Mielke-Fagan, K. A. Elam, and M. M. Clem, "Multiple-Point Mass Flux Measurement System Using Rayleigh Scattering," AIAA-2009-528, 2009 47th AIAA Aerospace Sciences Meeting Including The New Horizons Forum and Aerospace Exposition, Orlando, Florida, January 5 - 8 2009.

[153] J. Panda, R. G. Seasholtz, and K. A. Elam, "Investigation of noise sources in high-speed jets via correlation measurements," Journal of Fluid Mechanics, Vol. 537, pp.349-385, 2005.

[154] A.F. Mielke, K.A. Elam, C.J. Sung, "Multiproperty Measurements at High Sampling Rates Using Rayleigh Scattering," AIAA Journal, Vol. 47, No. 4, pp. 850-862, 2009.

[155] D. Bivolaru, A. D. Cutler, and P. M. Danehy, "Spatially- and Temporally-resolved Multi-parameter Interferometric Rayleigh Scattering," Paper AIAA-2011-1293, 49th AIAA Aerospace Sciences Meeting including the New Horizons Forum and Aerospace Exposition, Orlando, Florida, January 4-7, 2011.

[156] A. F. Fagan, M. M. Clem, K. A. Elam, "Improvement in Rayleigh Scattering Measurement Accuracy," 50th AIAA Aerospace Sciences Meeting including the New Horizons Forum and Aerospace Exposition, AIAA 2012-1060 Nashville, TN., January 9-12, 2012.

[157] J. Kojima, D. Fischer, and Q.-V. Nguyen, "Subframe burst gating for Raman spectroscopy in combustion," Optics Letters, Vol. 35, No. 9, p. 1323-1325, May 1, 2010.

[158] J. Kojima and D. G. Fischer, "Multiscalar Analyses of High-Pressure Swirl-Stabilized Combustion via Single-Shot Dual-SBG Raman Spectroscopy," Combust. Sci. technol. (under review).

[159] J. Kojima and Q.-V. Nguyen, "Single-shot rotational Raman thermometry for turbulent flames using a low-resolution bandwidth technique," Meas. Sci. Technol. 19 (2008).

[160] S. M. Schoenung, R. E. Mitchell, Comparison of Raman and Thermocouple Temperature Measurements in Flames, Combust Flame 35 (1979) 207-211.

[161] A.D. Cutler, G. Magnotti, L. M. L. Cantu, E. C. A. Gallo, P.M. Danehy and R. Baurle, R. Rockwell, C. Goyne, and J. McDaniel "Measurement of Vibrational Non-equilibrium in a Supersonic Freestream using Dual-Pump CARS" AIAA-2012-3199, 28th Aerodynamic Measurement Technology, Ground Testing, and Flight Testing Conference, New Orleans, Louisiana, June 25-28, 2012.

[162] J. A. Wehrmeyer, S. Yeralan, and K. S. Tecu, "Linewise Raman-Stokes/anti-Stokes temperature measurements in flames using an unintensified charge-coupled device," Appl. Phys. B. 62, p. 21–27, 1996.

[163] F. Rabenstein, A. Leipertz, Two-Dimensional Temperature Determination in the Exhaust Region of a Laminar Flat-Flame Burner with Linear Raman Scattering, Appl Opt 36 (1997) 6989-6996.

[164] J. Kojima, and Q.-V. Nguyen, "Strategy for Multiscalar Raman Diagnostics in High-Pressure Hydrogen Flames," In: New Developments in Combustion Research (Edited by W. J. Carey), ISBN: 1-59454-826-9, NOVA Science Publishers, New York, (2006), pp. 227-256.

[165] S. P. Sharma, S. M. Ruffin, W. D. Gillespie and S. A. Meyer, "Vibrational Relaxation Measurements in an Expanding Flow Using Spontaneous Raman Scattering," J. of Thermophys. and Heat Trans. Vol. 7, No. 4, Oct.-Dec. 1993.

[166] T. M. Dyer, "Rayleigh scattering measurements of time-resolved concentration in a turbulent propane jet,"AIAA Journal, vol. 17, Aug. 1979, p. 912-914.

[167] R. W. Boyd, Nonlinear Optics, 3rd Ed., Academic Press, 2008.

[168] R. P. Lucht, "Three-laser coherent anti-Stokes Raman scattering measurements of two species," *Optics Letters*, Vol. 12, No. 2, Feb. 1987, pp. 78-80.

[169] S. O'Byrne, P. M. Danehy, S. A. Tedder, A. D. Cutler, "Dual-Pump Coherent Anti-Stokes Raman Scattering Measurements in a Supersonic Combustor," *AIAA Journal*, Vol. 45, No. 4, p. 922-933, April 2007.

[170] R. E. Palmer, The CARSFT Computer Code for Calculating Coherent Anti-Stokes Raman Spectra: User and Programmer Information, Sandia report SAND89-8206, Feb. 1989.

[171] A. D. Cutler, G. Magnotti, "CARS Spectral Fitting with Multiple Resonant Species Using Sparse Libraries," *J. Raman Spectroscopy*, Vol. 42, Issue 11, 2011, pp. 1949-1957.

[172] K. M. Bultitude, P.M. Danehy, E. Fraval, J.S. Fox, A.F.P. Houwing "Broadband coherent anti-Stokes Raman spectroscopy (BB-CARS) in flames and hypersonic flows," 2nd Australian Conference on Laser Diagnostics in Fluid Mechanics and Combustion, Monash University, Melbourne Australia, 1999.

[173] W. D. Kulatilaka, N. Chai, S. V. Naik, N. M. Laurendeau, R. P. Lucht, J. P. Kuehner, S. Roy, J. R. Gord, "Measurement of nitric oxide concentrations in flames by using electronic-resonance-enhanced coherent anti-Stokes Raman scattering," *Optics Letters*, Vol. 31, Issue 22, pp. 3357-3359, http://dx.doi.org/10.1364/OL.31.003357, 2006.

[174] S. Roy, J. R. Gord, A. K. Patnaik, "Recent advances in coherent anti-Stokes Raman scattering spectroscopy: Fundamental developments and applications in reacting flows," *Progress in Energy and Combustion Science*, Vol. 36, Issue 2, pp. 280-306, ISSN 0360-1285, 10.1016/j.pecs.2009.11.001, April 2010.

[175] R. P. Lucht, P. J. Kinnius, S. Roy, J. R. Gord, "Theory of femtosecond coherent anti-Stokes Raman scattering spectroscopy of gas-phase transitions," *J. Chem. Phys*. 127, 044316, http://dx.doi.org/10.1063/1.2751184, 2007.

[176] R. P. Lucht, S. Roy, T. R. Meyer, J. R. Gord, "Femtosecond coherent anti-Stokes Raman scattering measurement of gas temperatures from frequency-spread dephasing of the Raman coherence," *Appl. Phys. Lett*. 89, 251112, http://dx.doi.org/10.1063/1.2410237, 2006.

[177] T. R. Meyer, S. Roy, J. R. Gord, "Improving Signal-to-Interference Ratio in Rich Hydrocarbon–Air Flames Using Picosecond Coherent Anti-Stokes Raman Scattering," *Applied Spectroscopy*, Vol. 61, Issue 11, pp. 1135-1140, 2007.

[178] P. S. Hsu, A. K. Patnaik, J. R. Gord, T. R. Meyer, W. D. Kulatilaka, S. Roy, "Investigation of optical fibers for coherent anti-Stokes Raman scattering (CARS) spectroscopy in reacting flows," Experiments in Fluids, Volume 49, Issue 4, pp 969-984, October 2010.

[179] M. A. Woodmansee, J. C. Dutton, R. P. Lucht, "Experimental Measurements of Pressure, Temperature, and Density Measurements in an Underexpanded Sonic Jet Flowfield," Paper No. AIAA 99-3600, presented at the 30th AIAA Fluid Dynamics Conference, Norfolk, VA., June 28-July 1, 1999.

[180] J. Zheng, J. B. J. B. Snow, D. V. Murphy, A. Leipertz, R. K. Chang, R. L. Farrow, "Experimental comparison of broadband rotational coherent anti-Stokes Raman scattering (CARS) and broadband vibrational CARS in a flame," *Optics Letters*, Vol. 9, No. 8, pp. 341-343, August 1984.

[181] A. Bohlin, B. D. Patterson, and C. J. Kliewer. "Simplified two-beam rotational CARS signal generation demonstrated in 1D." The Journal of chemical physics 138 (2013): 081102.

[182] A. Bohlin, and C. J. Kliewer. "Two-dimensional gas-phase coherent anti-Stokes Raman spectroscopy (2D-CARS): Simultaneous planar imaging and multiplex spectroscopy in a single laser shot." The Journal of Chemical Physics 138 (2013): 221101.

[183] A. D. Cutler, G. Magnotti, L. M. L. Cantu, E. C. A. Gallo, P. M. Danehy, R. D. Rockwell, C. P. Goyne, J. C. McDaniel, "Dual-Pump CARS Measurements in the University of Virginia's Dual-Mode Scramjet: Configuration "C"," AIAA-2013-0335, 51st Aerospace Sciences Meeting, Grapevine, TX, 7-10 Jan, 2013.

[184] G. Magnotti, A.D. Cutler and P.M. Danehy, "Development of a Dual-Pump CARS System for Measurements in a Supersonic Combusting Free Jet", Paper AIAA-2012-1193, presented at the 50th AIAA Aerospace Sciences Meeting, Nashville TN., January 9-12, 2012.

[185] A.D. Cutler, G. Magnotti, L.M.L. Cantu, E.C.A. Gallo, P.M. Danehy, R. Baurle, R.D., Rockwell, C.P. Goyne, J.C. McDaniel, "Measurement of Vibrational Nonequilibrium in a Supersonic Freestream using Dual-Pump CARS," AIAA Paper 2012-3199, 28th AIAA Aerodynamic Measurement Technology, Ground Testing, and Flight Testing Conference, New Orleans, 25-28 June 2012.

[186] Vincenti, W.G., Kruger, C.H., *Introduction to Gas Dynamics*, Robert Krieger Pub. Co., New York, 1977.

[187] Center, R.E., Newton, J.F., "Vibrational Relaxation of N_2 by H_2O," *J. Chem Phys.*, Vol. 68, No. 8, April 1978.

[188] A. Montello, Z. Yin, D. Burnette, I.V. Adamovich, and W.R Lempert, "Picosecond CARS Measurements of Nitrogen Vibrational Loading and Rotational/Translational Temperature in Nonequilibrium Discharges," Accepted for publication in J. Phys. D: Appl. Phys., May, 2013 (to appear in Sept, 2013).